

# TOWARDS HIGHLY EFFICIENT BIAS-FREE SOLAR WATER SPLITTING

Proefschrift

ter verkrijging van de graad van doctor  
aan de Technische Universiteit Delft,  
op gezag van de Rector Magnificus prof. ir. K.C.A.M. Luyben,  
voorzitter van het College van Promoties,  
in het openbaar te verdedigen op 10 september 2013 om 12:30 uur

door Fatwa Firdaus ABDI  
Master of Science, National University of Singapore

geboren te Jakarta, Indonesië

Dit proefschrift is goedgekeurd door de promotoren:

Prof. dr. B. Dam  
Prof. dr. R. van de Krol

Samenstelling promotiecommissie:

Rector Magnificus,	voorzitter
Prof. dr. B. Dam,	Technische Universiteit Delft, promotor
Prof. dr. R. van de Krol,	Helmholtz-Zentrum Berlin für Materialien und Energie, promotor
Prof. dr. M. Zeman,	Technische Universiteit Delft
Prof. dr. G. Mul,	Universiteit Twente
Prof. dr. R.A.J. Janssen,	Technische Universiteit Eindhoven
Dr. J.T.M. Kennis,	Vrije Universiteit Amsterdam
Prof. dr. K. Sivula,	École Polytechnique Fédérale de Lausanne
Prof. dr. J.J.C. Geerlings,	Technische Universiteit Delft, reservelid

Cover artwork by Ruth Marbun  
e: [ruth.marbun@gmail.com](mailto:ruth.marbun@gmail.com); w: <http://iniruthmarbun.blogspot.com>

Printed by: GVO drukkers & vormgevers B.V.

The work described in this thesis was carried out in Materials for Energy Conversion and Storage (MECS) group, Department of Chemical Engineering, Faculty of Applied Sciences, TU Delft. Financial support was provided by the European Commission's Framework Project 7 (NanoPEC, Project 227179).

ISBN 978-90-6464-693-5

## CONTENTS

<b>1 Introduction .....</b>	<b>5</b>
1.1 <i>The energy crisis</i> .....	5
1.2 <i>Photoelectrochemical (PEC) water splitting: the best possible solution?</i> .....	7
1.3 <i>Principle of PEC water splitting</i> .....	10
1.3.1 <i>Semiconductor</i> .....	10
1.3.2 <i>Semiconductor-electrolyte interface</i> .....	14
1.3.3 <i>PEC water splitting mechanism</i> .....	15
1.4 <i>Materials for PEC water splitting</i> .....	18
1.5 <i>Bismuth vanadate (BiVO<sub>4</sub>) as a photoelectrode material</i> .....	20
1.5.1 <i>Crystal structure</i> .....	20
1.5.2 <i>Electronic structure</i> .....	24
1.6 <i>This thesis</i> .....	26
1.7 <i>References</i> .....	27
<b>2 Nature and Light Dependence of Bulk Recombination in Co-Pi-Catalyzed BiVO<sub>4</sub> Photoanodes.....</b>	<b>30</b>
2.1 <i>Introduction</i> .....	31
2.2 <i>Experimental details</i> .....	32
2.3 <i>Results and discussion</i> .....	34
2.4 <i>Conclusions</i> .....	42
2.5 <i>References</i> .....	42
<b>3 Efficient BiVO<sub>4</sub> Thin Film Photoanodes Modified with Cobalt Phosphate Catalyst and W-doping.....</b>	<b>47</b>
3.1 <i>Introduction</i> .....	48
3.2 <i>Experimental details</i> .....	49
3.3 <i>Results and discussion</i> .....	51
3.4 <i>Conclusions</i> .....	58
3.5 <i>References</i> .....	58
<b>4 The Origin of Slow Carrier Transport in BiVO<sub>4</sub> Thin Film Photoanodes: a time-resolved microwave conductivity study .....</b>	<b>63</b>
4.1 <i>Introduction</i> .....	64
4.2 <i>Experimental details</i> .....	65
4.3 <i>Results and discussion</i> .....	66
4.4 <i>Conclusions</i> .....	73
4.5 <i>References</i> .....	74

<b>5 Efficient Solar Water Splitting with a Silicon PV-biased Gradient-doped Oxide Homojunction Photoanode.....</b>	<b>77</b>
5.1 Introduction.....	78
5.2 Experimental details .....	79
5.3 Results and discussion.....	81
5.4 Conclusions .....	90
5.5 References .....	91
<b>6 Design Rules for Hybrid Photoelectrodes for Solar Water Splitting.....</b>	<b>94</b>
6.1 Introduction.....	95
6.2 Hybrid photoelectrode configurations .....	96
6.3 Optimum photocatalyst for hybrid photoelectrode.....	102
6.4 Optimum PV cell for hybrid photoelectrode.....	107
6.5 Device optimization .....	111
6.6 Conclusions .....	115
6.7 References .....	116
<b>Appendix A.....</b>	<b>120</b>
<b>Appendix B.....</b>	<b>124</b>
<b>Appendix C.....</b>	<b>127</b>
<b>Summary.....</b>	<b>138</b>
<b>Samenvatting.....</b>	<b>141</b>
<b>List of Publications.....</b>	<b>144</b>
<b>Acknowledgements.....</b>	<b>146</b>
<b>Curriculum Vitae.....</b>	<b>148</b>

# 1 Introduction

*“I’d put my money on the sun and solar energy, what a source of power! I hope we don’t have to wait until oil and coal run out, before we tackle that.”*

Thomas Edison, 1931.

## 1.1 The energy crisis

The industrial revolution has introduced an exponential increase of the world’s population, which is accompanied by an increasing demand for energy. Currently, there are more than 7 billion people in the world, consuming 15 TW of energy. By 2050, it is estimated that ~9 billion people will populate the earth and 30 TW of energy is needed. Providing such a big amount of energy is a challenge that the society has to face. At the moment, more than 80% of our energy needs are met by fossil fuels, i.e. oil, coal and natural gas. However, these are finite natural resources, and we are depleting them at a rapid rate. While there are reports estimating that our fossil fuel reserves are enough for centuries, the effect of diminishing reserves will be felt much sooner. This is because many of these reserves are unconventional, which means the extraction process is much more challenging and expensive. As a result, the supply-demand relationship is no longer elastic. In fact, the global production of oil has been capped at 75 million barrels per day since 2005, even though the world oil price has been fluctuating between US\$ 40 to 130 per barrel.<sup>1</sup> To further illustrate the urgency of the problem, the WWF recently launched a report stating that if everyone in the world used oil at the same rate as the average Saudi, Singaporean, or U.S. resident, the world’s proven oil reserves would be used up in less than 10 years.<sup>2</sup>

Even if the fossil fuel supplies were infinite, there is a far more compelling reason for an urgent switch from fossil fuels: climate change, which is already causing more than 150,000 deaths a year.<sup>2</sup> The use of fossil fuels is accompanied by the emission of greenhouse gases, particularly carbon dioxide (CO<sub>2</sub>), which is the main cause of the climate change. The atmospheric CO<sub>2</sub> level has recently passed 400 ppm in early May

2013,<sup>3</sup> as compared to 280 ppm at the beginning of the industrial revolution, and it is rising with the rate of  $\sim 2$  ppm/year. According to the International Panel on Climate Change (IPCC), this level has to be kept below 450 ppm to prevent the average global temperature rise to exceed  $2^\circ\text{C}$  compared to pre-industrial temperatures and avoid devastating consequences.<sup>4</sup> To have a chance of doing that, global greenhouse gas emissions need to start falling within the next five years, and the industrialized world level need to fall back to 20% of the 1990 levels.<sup>5</sup>

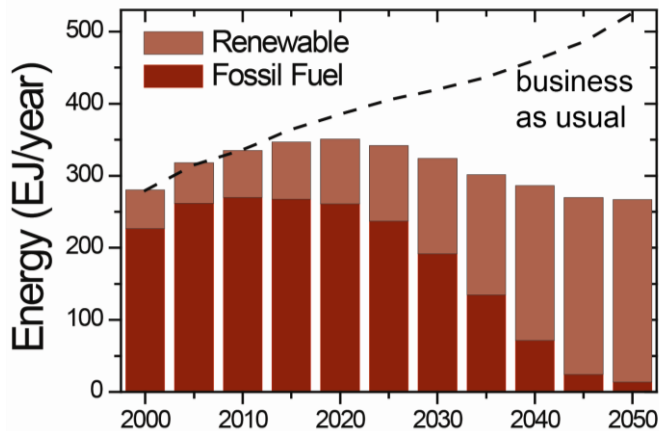


**Figure 1.1.** Ecofys scenario for fossil fuel to renewable energy transition. Adapted from ref [2].

The task ahead is a huge one, but it is fortunately not an unattainable utopia. Recently, Ecofys presented a scenario to address this challenge based on practically possible solutions.<sup>2</sup> This scenario is visualized in Figure 1.1. First, we need to implement an aggressive end-use energy savings and electrification strategy. It is then predicted that the energy demand in 2050 will be 15% lower than in 2005 and half of the business-as-usual situation. Secondly, a large-scale transition from fossil fuels towards sustainable and renewable sources of energy is needed. By 2050, it is expected that more than 90% of the energy needs are met by renewable sources, which would reduce the greenhouse gas emissions from the energy sector by about 80%.

The above scenario might be motivating, but it is certainly not the only possible scenario. While it is generally agreed that collective efforts from all parties (governments, industries, scientists, etc.) are required and they have to begin now, the optimal transition route from fossil fuels towards renewable energy sources is still highly debated. The viability of a certain route needs to be analyzed based on its economical merits as well as technological considerations.

## 1.2 Photoelectrochemical (PEC) water splitting: the best possible solution?

Figure 1.2 shows the estimated global power generation capacities of the various renewable energy sources. Depending on the availability and the geographical condition of a particular region, a mixture of these energy sources will form the most likely energy infrastructure of the future. Of all these sources, solar energy is the only one with the potential to meet all our energy needs. 120,000 TW of solar energy reaches the Earth's surface, out of which 36,000 TW is on land. This by far exceeds all other renewable sources combined. This means only 0.8% of the surface of the land on Earth needs to be covered with 10% efficient solar cells to generate 30 TW of power.

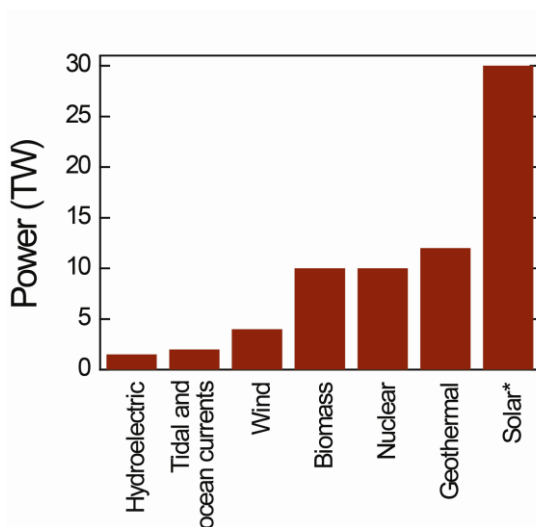


**Figure 1.2.** Global power generating capacities of various renewable energy sources. Adapted from various sources.<sup>6-8</sup> \*Note that the solar power capacity is calculated based on covering 0.8% of the surface of the land on Earth with 10% efficient solar cells.

Unfortunately, the intermittency of the sun is one major drawback of this energy source. The availability of solar energy is highly variable; it is subjected to a day/night cycle, the presence of clouds, geographical location, etc. To cope with that, electricity network operators might implement grid-based energy storage in the form of a 'smart grid'. However, at a certain point, the capacity of this grid system will be exceeded and alternative large-scale energy storage solutions need to be implemented. Table 1.1 shows the energy density of the different energy storage systems. Compared to mechanical-based storage systems and capacitors or batteries, fuels provide the most

effective way of storing energy, with a 2-3 orders of magnitude higher energy density. This is because the energy is stored in the smallest possible configuration: chemical bonds. Storing solar energy in the form of chemical fuels is therefore an attractive possibility.

**Table 1.1.** Gravimetric and volumetric (at 1 bar, unless specified) energy density of various energy storage techniques.<sup>7-9</sup>

Energy storage	Energy density	
	Gravimetric (MJ/kg)	Volumetric (MJ/L)
<b>Mechanical</b>		
Compressed air	0.512	0.16 (300 bar)
Pump water uphill	0.001	0.001
<b>Capacitors</b>		
Supercapacitor	0.01	—
Ultracapacitor	0.0206	—
<b>Batteries</b>		
Pb	0.14-0.17	—
NiCd	0.14-0.22	—
Li-ion	0.54-0.72	—
<b>Fuels</b>		
Coal	24	—
Wood	16	—
Gasoline	44	35
Diesel	46	37
Methanol	20	18
Natural gas	54	0.036
Hydrogen	143	0.011 5.6 (700 bar)

Examples of chemical fuels are shown in Table 1.1, such as methanol, methane, diesel, gasoline, and hydrogen. Most of these fuels require a source of carbon in their synthesis routes. In view of the environmental concerns outlined in the previous section, CO<sub>2</sub> is an obvious candidate. However, direct conversion of CO<sub>2</sub> to a fuel (e.g. methanol, methane) is a very challenging task. Its concentration in air is rather low (398 ppm), so one is probably bound to use point sources. Furthermore, the electrochemical conversion of CO<sub>2</sub> to methanol and methane requires complex six- or eight-electron transfer reactions, respectively. The production of hydrogen, on the other hand, does not require a carbon source. Water can be used as the source of hydrogen through a water splitting reaction. This reaction requires 237 kJ/mol of energy, which can very well be provided by the energy of a visible-light photon.



Additionally, the reduction and oxidation half-reactions only require two and four electrons, respectively. While this is by no means trivial, it is much easier than the direct conversion of CO<sub>2</sub> to fuels.

Hydrogen has a very high gravimetric energy density, more than three times the energy density of gasoline. However, the problem lies in the volumetric energy density. At 1 bar, its volumetric energy density is only 0.011 MJ/L, 3 orders of magnitude lower than gasoline. This can be increased by storing H<sub>2</sub> in high pressure containers—5.6 MJ/L is possible at 700 bar—but it comes with a ~10% energy penalty for hydrogen compression. Hydrogen can also be stored in the form of metal hydrides, such as MgH<sub>2</sub>. However, at the moment, the storage capacity of this system is still too low (< 2 wt% in any convenient pressure-temperature operating window). Alternatively, hydrogen can react with CO<sub>2</sub> to produce chemical fuels. In this process, CO<sub>2</sub> is indirectly converted into hydrocarbons, which is a much easier route than the direct electrochemical process. CO<sub>2</sub> and hydrogen can be converted into CO using a reverse water-gas shift reaction. The CO and H<sub>2</sub> form syngas, which can be converted to any liquid hydrocarbon fuels using well-known Fischer-Tropsch processes.<sup>10</sup> This type of fuel is also easily transported; more than 80% of our current energy use is in the form of liquid hydrocarbons. This means that there is already a huge infrastructure available, which will ease the transition from fossil fuels.

While there are many possible pathways for the conversion of water and sunlight into hydrogen,<sup>7, 11, 12</sup> in this thesis we choose the photoelectrochemical (PEC) water splitting route because of the easy separation of the gasses and a suitable pressure-temperature operating window. The technology for indirect PEC water splitting using coupled photovoltaic (PV) and electrolyzer systems is already commercially available, showing a solar-to-hydrogen (STH) efficiency of around 8%. However, direct PEC water splitting—this process will be discussed in the next section—offers three important advantages. First, due to the 50-100 times lower operating current density of the direct PEC water splitting, a much lower overpotential is needed. This relaxes the condition of the catalytic step in the process. Second, in order to achieve the potential needed for the electrolyzer (~1.9V), three (or more) PV cells are normally used in series. As a result, a larger area is needed to achieve the same current density, which is not the case for direct PEC water splitting. Finally, a direct PEC water splitting system requires fewer additional components (wires, frames, glass, etc.) than a combination of PV plus electrolysis since one can construct a monolithic device. This may lead to a significantly lower balance-of-system cost for producing hydrogen. Coupled PV-electrolyzer is estimated to produce hydrogen at the cost exceeding US\$ 8/kg, while a reasonable estimate of the direct PEC water splitting shows a cost in the range of US\$ 3-5/kg.<sup>13, 14</sup> This compares very well with the US\$ 2-4/kg target that is set by the US Department of Energy (DOE), and the EU's 5 €/kg H<sub>2</sub> target for future hydrogen production pathways.

Direct PEC water splitting—after this point “PEC water splitting” refers to the direct process—therefore offers the best possible solution to our growing concern, as outlined in section 1.1. The challenge lies in the efficiency improvement of this process, which is one of the central themes of this thesis. Additionally, the scale of the production also poses a challenging requirement. To illustrate this, a hydrogen production of  $\sim 127$  Mega-moles per second is needed to fulfill the 30 TW energy demand by 2050. This means 10%-efficient  $H_2$  production devices need to be made non-stop (24/7/365) at a rate of  $\sim 500$   $m^2/s$  until 2050. While this will not be thoroughly addressed in this thesis, this factor is taken into account here and should always be considered in the development of PEC water splitting process.

### **1.3 Principle of PEC water splitting**

The main component in PEC water splitting is the semiconductor, which converts incident photons to electron-hole pairs. Therefore, in this section, the basic properties of a semiconductor will be discussed, followed by a description of the semiconductor-electrolyte interface. Finally, a complete PEC cell and the relevant processes that occur will be described.

#### **1.3.1 Semiconductor**

Quantum mechanics states that electrons can only occupy discrete energy levels. Further restrictions apply due to the Pauli exclusion principle: no two electrons can have the same set of quantum numbers. Therefore, electrons in the same orbital must have opposite spins. When two atoms are brought together, the molecular orbitals combine to form bonding and anti-bonding energy levels. If more and more atoms are brought together, the spread in energies gives rise to closely spaced sets of allowed states known as energy bands. Two energy bands will be formed, corresponding to the bonding and anti-bonding energy levels, which are called the valence band and the conduction band, respectively. The valence band is filled with electrons, while the conduction band is mostly empty. In the valence band, electrons are effectively immobile, while they are mobile in the conduction band. The difference between the valence and conduction band is called the forbidden gap or bandgap, since no energy states are allowed to exist in this region.

Materials are often classified by their electrical properties, which are determined by their respective bandgap size. Figure 1.3 shows the energy diagrams of three different classes of materials: metal, semiconductor and insulator. For metals, the valence bands overlaps with the conduction bands, i.e. no bandgap exists at all in metal. As a result,

there is always an abundance of carriers in metals, which make them good conductor. On the other hand, insulators have very wide bandgaps. As an example, SiO<sub>2</sub> is an insulator and it has a bandgap size of ~8 eV. This gap is too large for room-temperature thermal excitation of electrons from the valence band to the conduction band. Therefore, very few—if any—carriers exist inside insulators, which make them poor conductors.

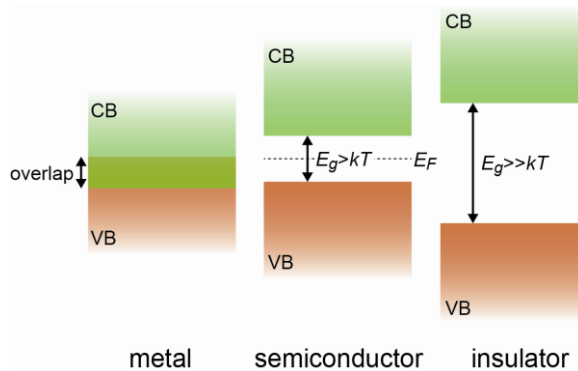


**Figure1.3.** Energy diagram of a metal, a semiconductor and an insulator. CB = conduction band, VB = valence band,  $E_g$  = bandgap energy,  $E_F$  = Fermi energy,  $k$  = Boltzmann constant,  $T$  = temperature.

Semiconductors stand in between metals and insulators. Their conduction bands and valence bands are separated by moderately sized bandgaps (in the order of 1-3 eV). While this is still not small enough for room-temperature thermal excitation of electrons to occur, the bandgap size of the semiconductor is in the energy range provided by sunlight. This is a very special property of semiconductors which make them very suitable for solar cells and PEC water splitting applications. Upon illumination, electrons can therefore be excited from the valence band to the conduction band. This excitation will create two mobile carriers: a photo-generated electron in the conduction band and a photo-generated hole (missing electron) in the valence band. Both carriers have significant roles in PEC water splitting reaction, which will be discussed in section 1.3.3.

Figure 1.3 shows a dashed line in the bandgap region of a semiconductor. This is the Fermi energy level, which is defined as the energy level at which the probability of it being occupied by an electron is exactly half. This energy can also be viewed as the electrochemical potential of the electrons in the semiconductor. Ideally, at absolute zero temperature (0 K), the valence band of a semiconductor is completely filled with electrons, whereas the conduction band is completely empty. Therefore, the Fermi energy level is located at exactly halfway between the valence and conduction band.

However, above 0 K, the chance for an electron to be thermally excited to the conduction band is larger than zero. The distribution of electrons over the energy levels can then be described by the Fermi-Dirac distribution and the density of states in the conduction and valence band.

The Fermi-Dirac distribution ( $f(E)$ ) determines the probability of an energy level  $E$  being occupied by an electron at a certain temperature  $T$ , which is given by the following equation:

$$f(E) = \frac{1}{\exp\left(\frac{E - E_F}{kT}\right) + 1} \quad (1.1)$$

The density of states ( $g(E)$ ) defines the number of available energy states at a certain energy level  $E$ , given for the conduction and valence band by the following equations:

$$g_c(E) = \frac{m_e^* \sqrt{2m_e^*(E - E_c)}}{\pi^2 \hbar^3} \quad (1.2)$$

$$g_v(E) = \frac{m_h^* \sqrt{2m_h^*(E_v - E)}}{\pi^2 \hbar^3} \quad (1.3)$$

$m_e^*$  and  $m_h^*$  are the effective masses of electrons and holes, respectively;  $\hbar = h/2\pi$ ,  $h$  is the Planck's constant, and  $E_c$  and  $E_v$  are the energy levels of the conduction and valence band edge, respectively. The combination of the Fermi-Dirac distribution and the density of states therefore define the number of electrons at a certain energy level  $E$  ( $g(E)f(E)$ ). Specifically, the number of electrons ( $n$ ) and holes ( $p$ ) in the conduction and valence band, respectively, is given by the following equations.

$$n = \int_{E_c}^{E_{top}} g_c(E) f(E) dE \quad (1.4)$$

$$p = \int_{E_{bottom}}^{E_v} g_v(E) (1 - f(E)) dE \quad (1.5)$$

For a non-degenerate semiconductor, where the difference between the Fermi energy level and the conduction or valence band is more than  $3kT$ , these two equations can be further simplified to the followings:

$$n = N_C \exp\left(\frac{E_F - E_C}{kT}\right) \text{ with } N_C = 2\left(\frac{2\pi m_e^* kT}{h^2}\right)^{3/2} \quad (1.6)$$

$$p = N_V \exp\left(\frac{E_V - E_F}{kT}\right) \text{ with } N_V = 2\left(\frac{2\pi m_h^* kT}{h^2}\right)^{3/2} \quad (1.7)$$

$N_C$  and  $N_V$  are the effective densities of states in the conduction and valence bands, respectively.

For practical applications, extremely pure semiconductors (also called *intrinsic* semiconductors) are often not desired, mainly due to the relatively poor conductivity. To rectify this, semiconductors are often doped with impurities. This type of semiconductors is also referred to as *extrinsic* semiconductors. Depending on their valency, there are two different types of dopants: donor and acceptor. In donor-doped semiconductors, an impurity with higher valency than the host atom is introduced, e.g. phosphorus or arsenic in silicon. The extra valence electron in the donor-type dopants can be excited to the conduction band and thereby improve the conductivity of the semiconductor. In contrast, acceptor-doped semiconductors have impurity with lower valency than the host atom, e.g. boron in silicon or  $\text{Cr}^{3+}$  on a  $\text{Ti}^{4+}$  site in  $\text{TiO}_2$ . As a result, electrons can be excited from the valence band of the semiconductor to the acceptor-type dopants, creating holes in the valence band of the semiconductor.

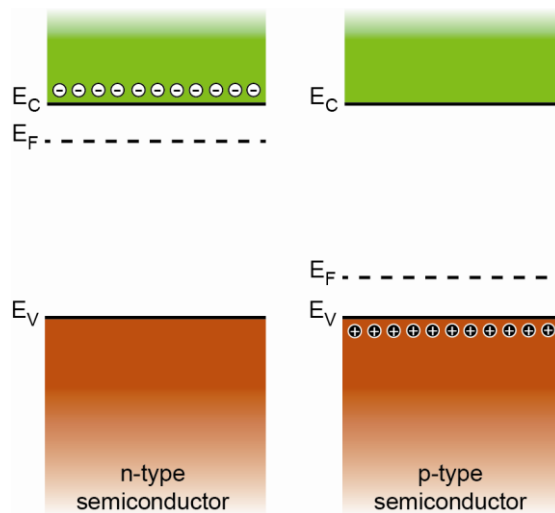


**Figure 1.4.** Energy diagram of extrinsic semiconductors: n-type (left) and a p-type (right).

A donor-doped semiconductor (n-type semiconductor) has electrons as the majority carriers, while holes are the majority carriers for an acceptor-doped semiconductor (p-type semiconductor). Figure 1.4 shows the energy band diagram of an n-type and a p-type semiconductor. Due to the large presence of electrons in the conduction band, the Fermi level in an n-type semiconductor is much closer to the conduction band. Similarly, the Fermi level in a p-type semiconductor is located close to the valence band, because of the high existence of holes.

### **1.3.2 Semiconductor-electrolyte interface**

In PEC water splitting, the semiconductor will be immersed in aqueous electrolyte. When the semiconductor is brought into contact with water, a charge transfer reaction is happening between the semiconductor and the electrolyte until the electrochemical equilibrium condition is achieved. For example, Figure 1.5a shows the energy levels of an isolated n-type semiconductor and the redox potentials of the dominant redox species in the electrolyte. In the whole volume of an isolated semiconductor, the amount of ionized donor (+) equals the number of electrons. However, when the n-type semiconductor is contacted with the electrolyte, electrons will be transferred from the semiconductor to the electrolyte, until it reaches equilibrium. This is when the Fermi level of the semiconductor is at the same level as the redox level of the electrolyte (Fig. 1.5b). As a result, an upward bending of the bands is created, and there is a region near the surface of the semiconductor where the concentration of electrons is depleted. This region is called the depletion layer or the space charge layer.

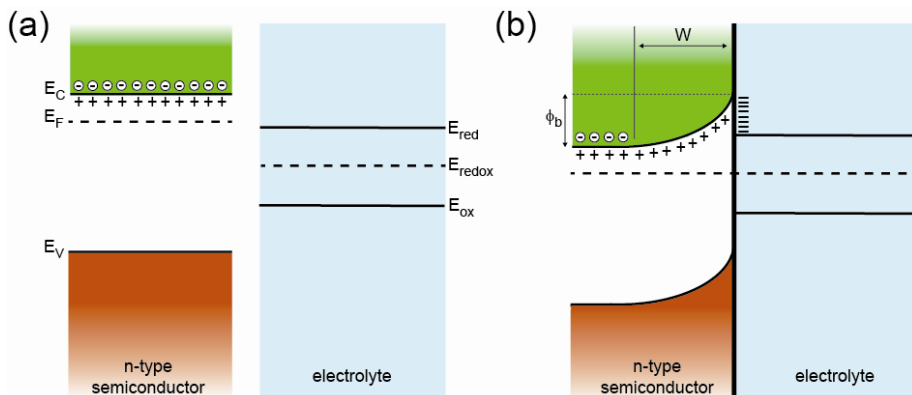


**Figure 1.5.** The formation of space charge layer in n-type semiconductor when it is immersed in the electrolyte. **(a)** represents the isolated band diagram of the semiconductor and the electrolyte, while **(b)** represents the equilibrated band diagram.

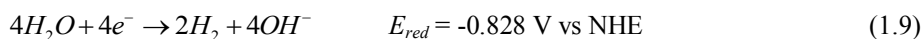
A space charge layer is important in the context of PEC water splitting, since in this layer a potential drop ( $\phi_b$ ) is present. This resulted in an electric field, which is beneficial for the separation of photo-generated electrons and holes. The width of the space charge ( $W$ ) is determined by the following equation:

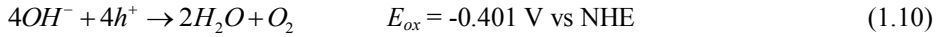
$$W = \sqrt{\frac{2\epsilon_0\epsilon_r}{eN_D} \left( \phi_b - \frac{kT}{e} \right)} \quad (1.8)$$

$N_D$  is the concentration of ionized donors,  $\epsilon_0$  is the dielectric permittivity of vacuum and  $\epsilon_r$  is the relative dielectric permittivity of the semiconductor. For more detailed information on semiconductor properties, the effect of the pH of the electrolyte and the applied potential, etc, the reader is referred to several excellent textbooks on the topic (e.g. Bard and Faulkner,<sup>15</sup> van de Krol and Grätzel<sup>7</sup>).

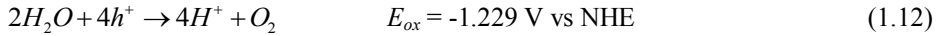
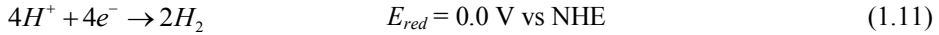
### 1.3.3 PEC water splitting mechanism

Figure 1.6a shows a schematic illustration of a PEC cell based on an n-type semiconductor and a metal counter electrode, both immersed in aqueous electrolyte. In an alkaline electrolyte, the reduction and oxidation reactions of water can be written as follows:





For an acidic electrolyte, the equations can be modified to the following:



The overall water splitting reaction can therefore be written as the following:

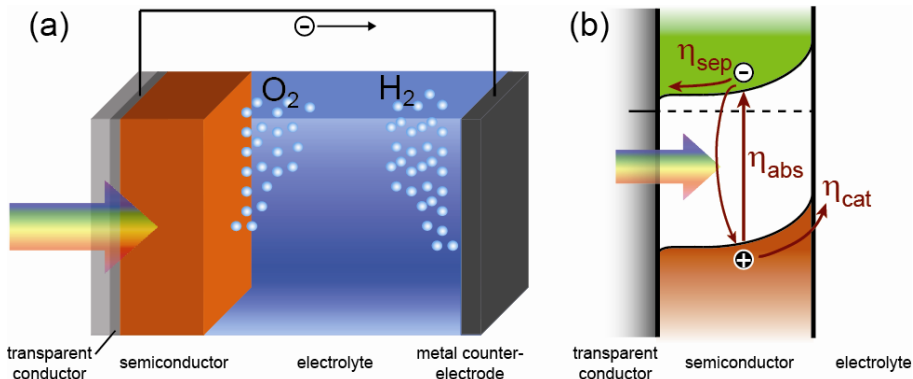
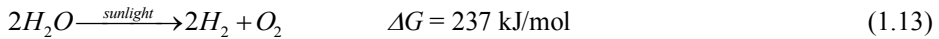


**Figure 1.6.** (a) Schematic diagram of a PEC cell setup. (b) Processes occurring in the semiconductor upon illumination.

Upon illumination, the semiconductor absorbs light with an energy larger than its bandgap, and converts these photons to electron-hole pairs. The schematic processes in an n-type semiconductor are depicted in Fig. 1.6b. The absorption efficiency ( $\eta_{abs}$ ) is defined as the ratio of the electron-hole pairs created to the amount of incident photons. These photo-generated electrons and holes are then separated by two possible transport mechanisms: (i) drift and (ii) diffusion. Drift is the motion of these charged-particles in response to the electric field inside the semiconductor, while diffusion is associated with a gradient in the local concentration of the charged particles. In this n-type semiconductor, the photo-generated holes are swept toward the semiconductor/electrolyte interface, and the photo-generated electrons are swept toward the semiconductor/transparent conductor interface. Depending on the mobility



of the carriers in the semiconductor, some of these electrons and holes will actually recombine before reaching their respective interfaces. The ratio between the amount of electrons and holes reaching the interfaces to the photo-generated electron-hole pairs is called the separation efficiency ( $\eta_{sep}$ ). The holes that arrive at the semiconductor/electrolyte interface will undergo a water oxidation reaction, as described in equation 1.10 or 1.12. The amount of holes that undergo the water oxidation reaction normalized to the ones reaching the semiconductor/electrolyte interface is the catalytic efficiency ( $\eta_{cat}$ ). On the other hand, the electrons will be transported by an external circuit to the metal counter electrode (e.g. platinum), where they will undergo the water reduction reaction (equation 1.9 or 1.11). The same processes occur for PEC water splitting using a p-type semiconductor, except that water is reduced on its surface and oxidized at the counter electrode. Based on the half-reactions at the surface, an n-type semiconductor in PEC water splitting is called a photoanode (oxidation) and a p-type semiconductor is called a photocathode (reduction).

The total efficiency of the PEC water splitting process (also called solar-to-hydrogen or STH efficiency,  $\eta_{STH}$ ) can therefore be defined as the product of all the efficiencies described above:

$$\eta_{STH} = \eta_{abs} \times \eta_{sep} \times \eta_{cat} \quad (1.14)$$

Alternatively, STH efficiency can also be defined as the ratio of the chemical energy in the generated hydrogen to the solar energy input:

$$\eta_{STH} = \frac{\Delta G \times R_{H_2}}{P \times A} \quad (1.15)$$

where  $R_{H_2}$  is the rate of hydrogen production,  $P$  is the incident power of the solar energy input (1000 W/m<sup>2</sup> is normally used for standard AM1.5G condition), and  $A$  is the area of the electrode. If 100% Faradaic conversion efficiency is assumed, replacing the Gibbs free energy with the corresponding voltage (1.23 V) and the rate of hydrogen evolution with the photocurrent density ( $j$ ), equation 1.15 can be modified to the following:

$$\eta_{STH} = \frac{j \times 1.23}{P} \quad (1.16)$$

Finally, it is important to note that STH efficiency is the only efficiency term that can be used to describe the overall performance of a PEC water splitting device in terms of energy conversion. Other (quantum) efficiency expressions exist, but they

should only be carefully used for diagnostic purposes of a certain photoelectrode. These terms will be discussed in more detail in the following chapters and appendices of this thesis.

#### 1.4 Materials for PEC water splitting

For a semiconductor to be considered as a good material for PEC water splitting, it needs to fulfill several requirements. First, it needs to have high visible light absorption. Most of the photons in sunlight, as shown in Fig. 1.7, are in the visible light regime. The absorption of a material is defined by its respective bandgap size. If we consider the minimum energy needed to thermodynamically split water to hydrogen and oxygen, photons with energy higher than 1.23 eV are of interest. This corresponds to the light absorption up to  $\sim 1000$  nm ( $\lambda_{\max}$ ). However, if the thermodynamic losses and the overpotentials required for sufficiently fast reaction kinetics are considered,<sup>16-18</sup> the semiconductor needs to have a minimum bandgap of  $\sim 1.9$  eV ( $\lambda_{\text{abs}} < 650$  nm). To achieve the DOE target of 10% STH efficiency, a minimum photocurrent density of  $\sim 8$  mA/cm<sup>2</sup> is necessary (equation 1.16), which means a maximum bandgap of  $\sim 2.3$ - $2.4$  eV. Therefore, the optimum value of the bandgap should be between 1.9 and 2.4 eV. This is consistent with a prediction by Murphy et al. of a hypothetically ideal material with a bandgap of  $\sim 2.03$  eV.<sup>18</sup>

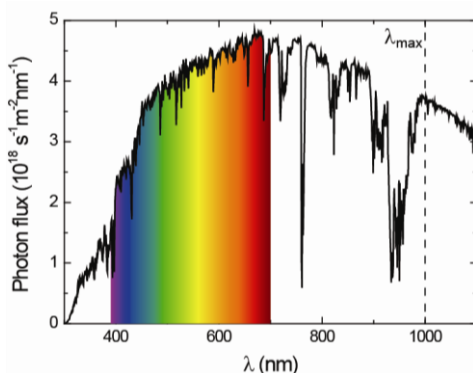


**Figure 1.7.** AM1.5 spectrum indicating the visible light regime. The maximum wavelength of light that is thermodynamically able to perform the water splitting reaction ( $\lambda_{\max}$ ) is identified with the vertical dashed line.

The second requirement for a single material to split water is that the band edges of the semiconductor need to be suitably positioned to enable reduction and oxidation

reaction of water. This means both the conduction and valence band need to straddle the redox potential of water ( $E_c > E_{red}$  and  $E_v < E_{ox}$ ). This way, the photo-generated electrons and holes will have enough driving force to perform the reduction and oxidation of water. Additionally, the charge transport within the semiconductor needs to be highly efficient. This is often determined by intrinsic properties of the material, such as electron and hole mobilities, but extrinsic properties (e.g. the presence of defects) often also play an important role. The fourth requirement is that the semiconductor has a high catalytic activity toward oxidation or reduction of water. For an n-type semiconductor, this means that the transfer of the photo-generated holes across the semiconductor/electrolyte interface should be relatively fast to avoid hole accumulation at the surface, which will increase the electron-hole recombination.

The semiconductor must also have high chemical stability in the dark and under illumination. This requirement is very crucial, since many excellent photo-active materials are prevented from being a good material for PEC water splitting due to their instability, or by the formation of an electrically-insulating passivation layer (e.g. Si, GaAs, GaP, CdSe). The general rule for material's stability in PEC water splitting is shown in Fig. 1.8. For a stable photoanode (n-type semiconductor), the oxidation potential of the material in aqueous solution ( $\phi_{ox}$ ) needs to be lower than the oxygen evolution potential. On the other hand, the reduction potential ( $\phi_{red}$ ) of a photocathode (p-type semiconductor) needs to be higher than the hydrogen evolution potential for it to be stable.

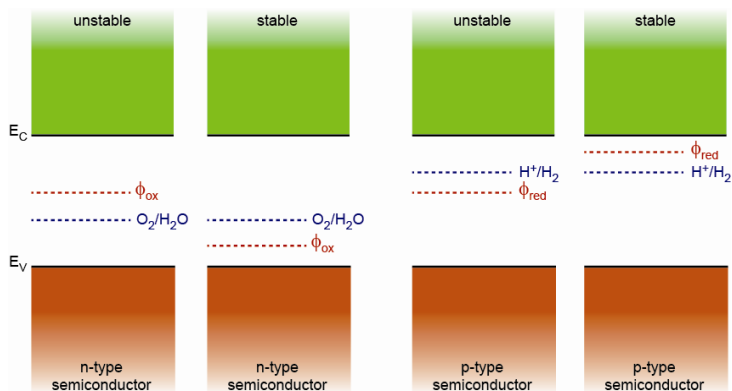


**Figure 1.8.** General stability rule of semiconductor in PEC water splitting.  $\phi_{ox}$  and  $\phi_{red}$  are the oxidation and reduction potential of the semiconductor in aqueous solution, respectively.

Finally, the semiconductor must be economically viable. A recent techno-economical analysis shows that the corresponding PEC device needs to cost less than

US\$ 160 per m<sup>2</sup>.<sup>14</sup> Combined with the large scale of the application, the semiconductor therefore must be composed of cheap, abundant materials. The production technique also needs to be largely scalable, as high production rate of the PEC device is required. A back-of-the-envelope calculation shows that a full conversion to a solar-driven society in 2050, based on 10% efficient devices, requires production rates in the order of 500 m<sup>2</sup>/s. This means the semiconductor for PEC water splitting will ideally be able to be synthesized by a large-scale technique, such as roll-to-roll printing and spray deposition.

Due to these stringent requirements, it is very difficult to find an ideal semiconductor material for PEC water splitting. To some, this is even considered as the 'Holy Grail' in photoelectrochemistry. Metal oxides are often considered as the class of material suitable for water splitting, mainly due to their general stability in aqueous solution and relatively low cost. However, they usually do not have very good semiconducting properties, such as carrier mobility, compared to III-V semiconductors or even silicon. The challenge is therefore to overcome these limitations while taking advantage of the stability and the low-cost of the metal oxides, which will be addressed in this thesis.

## **1.5 Bismuth vanadate (BiVO<sub>4</sub>) as a photoelectrode material**

In the decades of study on metal oxide photoelectrodes, much emphasis has been placed on binary metal oxides. However, only few of these can be identified as promising (photocurrent density > 1 mA/cm<sup>2</sup>),<sup>19-21</sup> and they even do not fulfill all the strict requirements described in the previous section. The development of more complex metal oxides, such as ternary metal oxides, can therefore not be avoided. Bismuth vanadate (BiVO<sub>4</sub>) is one of the most promising complex metal oxide photoanodes known to date, and the metal oxide of interest in this thesis. In this section, a brief overview of the crystal and electronic structures of BiVO<sub>4</sub> in relation to the photoelectrochemical properties is presented.

### **1.5.1 Crystal structure**

There are three polymorphs of BiVO<sub>4</sub> crystal: pucherite, dreyerite and clinobisvanite. Pucherite is the form of BiVO<sub>4</sub> found in nature, named after the location where it was found (Pucher Shaft, Wolfgang Maaßen mine field, Schneeberg, Germany). It has an orthorhombic crystal structure (space group *Pnca* with  $a = 5.332$  Å,  $b = 5.06$  Å and  $c = 12.02$  Å).<sup>22</sup> BiVO<sub>4</sub> prepared in the laboratory normally does not have the pucherite structure. Dreyerite has a tetragonal (zircon-type) crystal structure

(space group  $I4_1/amd$  with  $a = b = 7.303 \text{ \AA}$  and  $c = 6.584 \text{ \AA}$ ),<sup>23</sup> while clinobisvanite has a monoclinic (scheelite-type) crystal structure (space group  $C_2/c$  with  $a = 7.247 \text{ \AA}$ ,  $b = 11.697 \text{ \AA}$ ,  $c = 5.09 \text{ \AA}$  and  $\beta = 134.226^\circ$ ).<sup>24, 25</sup> Figure 1.9 shows these different crystal structures for  $\text{BiVO}_4$ . A scheelite-type tetragonal crystal structure also exists, which is a slight modification of the monoclinic clinobisvanite  $\text{BiVO}_4$  in terms of the atomic positions of Bi, V, and O (space group  $I4_1/a$  with  $a = b = 5.147 \text{ \AA}$ , and  $c = 11.7216 \text{ \AA}$ ).<sup>24</sup>

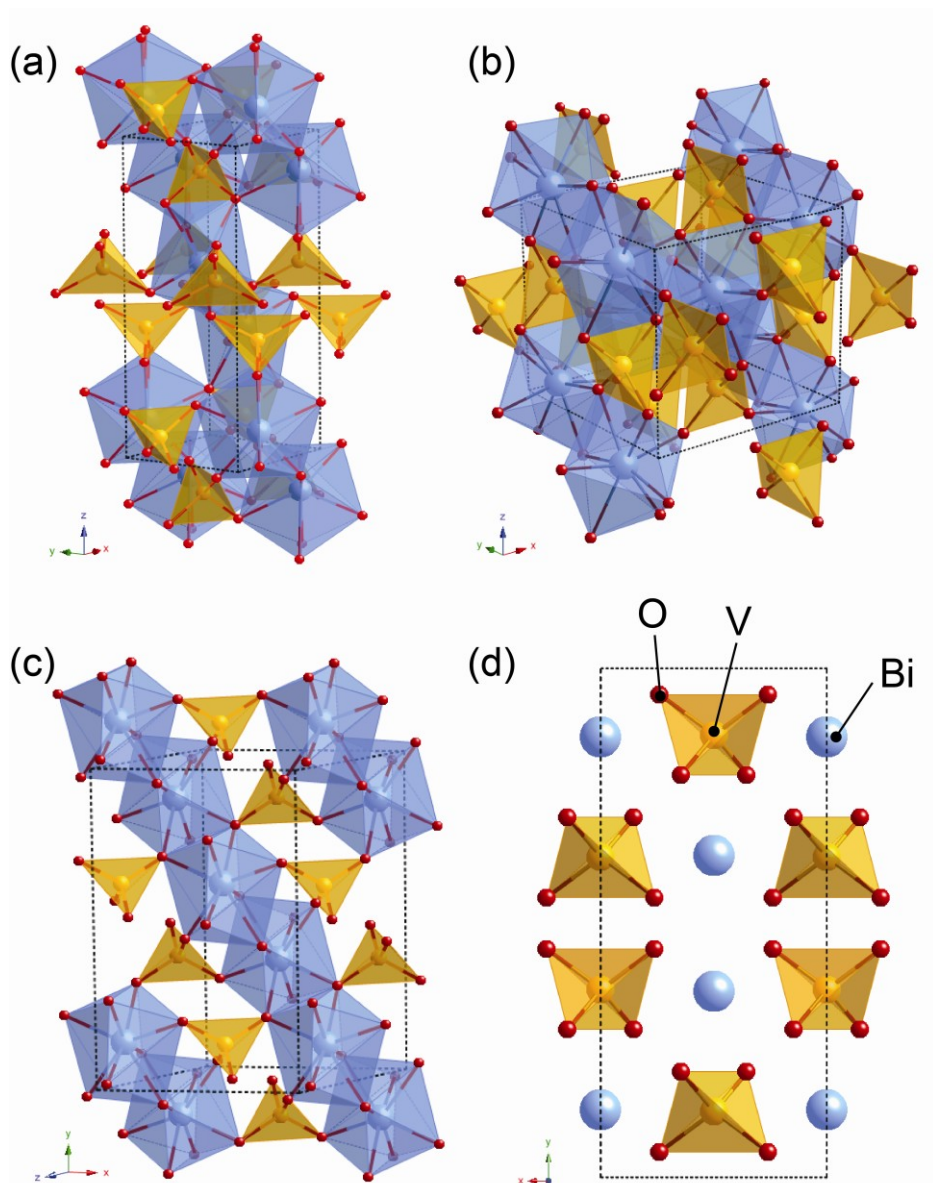


**Figure 1.9.** Crystal structures of different  $\text{BiVO}_4$  polymorphs: (a) pucherite (orthorhombic), (b) dreyerite (tetragonal zircon), (c) clinobisvanite (monoclinic scheelite). The side view (c axis) of the clinobisvanite structure is shown in (d).

Each V ion in all BiVO<sub>4</sub> polymorphs is coordinated by four O atoms (tetrahedral), and each Bi ion is coordinated by eight O atoms (dodecahedral). In the scheelite structure, each BiO<sub>8</sub> dodecahedral unit is surrounded by eight different VO<sub>4</sub> units. Each oxygen atom is coordinated to two Bi centers and one V center. This is true for both monoclinic and tetragonal scheelite structure. However, in the monoclinic scheelite, more distortion in the local environments of Bi and V ions is observed. As a result, the four-fold symmetry is lost. It can be seen from the difference in bond angles between these two structures, as shown in Table 1.2. In a tetragonal scheelite, all four V-O bond lengths are equal (1.73 Å), and only two different Bi-O bond lengths exist (2.4 and 2.47 Å).<sup>24</sup> On the other hand, there are two different V-O bond lengths (1.69 and 1.76 Å) and four different Bi-O bond lengths (2.35, 2.37, 2.52 and 2.63 Å) in a monoclinic scheelite structure.<sup>24</sup> This distortion in the monoclinic scheelite is claimed to be responsible for a higher photocatalytic activity when compared to the tetragonal scheelite structure, as shown by Tokunaga et al.<sup>26</sup> This distortion enhances the local polarization, which improves the electron-hole separation and, thereby, the photocatalytic activity.

**Table 1.2.** Bond lengths of Bi-O and V-O in different crystal structures of BiVO<sub>4</sub>.

Bond	Bond Length (Å)			
	Monoclinic Scheelite	Tetragonal Scheelite	Tetragonal Zircon	Orthorhombic
Bi-O	2.35			2.2
	2.37	2.4	2.41	2.31
	2.52	2.47	2.55	2.53
	2.63			2.73
V-O	1.69	1.73	1.7	1.76
	1.76			1.95

In the zircon structure, each BiO<sub>8</sub> dodecahedral unit is surrounded only by six VO<sub>4</sub> tetrahedral units. Two VO<sub>4</sub> units provide two O atoms, while four units provide one O atom to Bi. Finally, each BiO<sub>8</sub> unit is surrounded by seven VO<sub>4</sub> units in the orthorhombic structure, since one VO<sub>4</sub> unit gives two O atoms to Bi. The bond lengths for these two crystal structures can also be found in Table 1.2.

The zircon-type structure is normally obtained from low-temperature synthesis, such as aqueous precipitation at room temperature, while the monoclinic scheelite structure is obtained by high-temperature preparation methods.<sup>27, 28</sup> The zircon-type structure can be phase transformed irreversibly to monoclinic scheelite at ~400-500°C.<sup>27, 29</sup> The tetragonal scheelite phase is obtained at higher temperatures than the monoclinic scheelite phase. The transition between tetragonal and monoclinic scheelite occur reversibly at 255°C.<sup>27</sup>

## 1.5.2 Electronic structure

The electronic structure of  $\text{BiVO}_4$  has a strong correlation to the photocatalytic activity. Early study by Kudo et al. showed that the monoclinic scheelite  $\text{BiVO}_4$  has a superior photocatalytic activity as compared to the zircon-type  $\text{BiVO}_4$ .<sup>27</sup> They proposed that this is mainly caused by the enhanced photon absorption in the scheelite  $\text{BiVO}_4$ , as a result of smaller bandgap (2.4 and 2.9 eV for scheelite- and zircon-type  $\text{BiVO}_4$ , respectively). The charge transition in zircon-type  $\text{BiVO}_4$  occurs between O 2p orbitals and empty V 3d orbitals, whereas transition between Bi 6s or hybrid Bi 6s-O 2p orbitals and empty V 3d orbitals occurs in scheelite-type  $\text{BiVO}_4$ . This difference is illustrated in Figure 1.10.

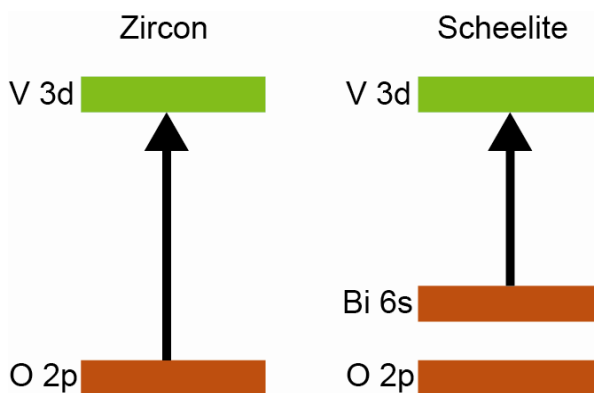


**Figure 1.10.** Schematic band structure of zircon- and scheelite-type  $\text{BiVO}_4$ .

Further analysis based on density functional theory (DFT) calculations and x-ray spectroscopy studies was performed in the last decade.<sup>25,30-33</sup> It was found that zircon-type  $\text{BiVO}_4$  indeed has different arrangements of the density of states, as compared to the scheelite-type  $\text{BiVO}_4$ . In zircon-type  $\text{BiVO}_4$ , there is a strong interaction between Bi and O atoms, as indicated by the relatively shorter Bi-O bonds. The valence band maximum is composed of mainly O 2p orbitals, which is located quite low, causing poor photocatalytic response in the visible light regime.<sup>32</sup> The analysis also confirmed that the scheelite-type  $\text{BiVO}_4$  has a smaller bandgap. However, these studies indicate that, despite the presence of Bi 6s above the O 2p orbital, the transition originating from visible light still occurs between O  $2p_\pi$  and empty V 3d orbital. This distance is however decreased as a result of the crystal distortion, especially in monoclinic scheelite  $\text{BiVO}_4$ , which pulls the O 2p states upwards and reduces the bandgap.<sup>25</sup> This is in agreement with the indication that there is no overlap between the wave functions at the edges of the valence and conduction band, and the large spatial distance between



Bi and V atoms ( $\sim 3.61\text{-}3.85 \text{ \AA}$ ). Therefore, an electronic transition from the occupied Bi 6s to the V 3d states, as suggested earlier, is rather unlikely. The molecular orbital bonding diagram for the monoclinic scheelite  $\text{BiVO}_4$  is shown in Fig. 1.11.

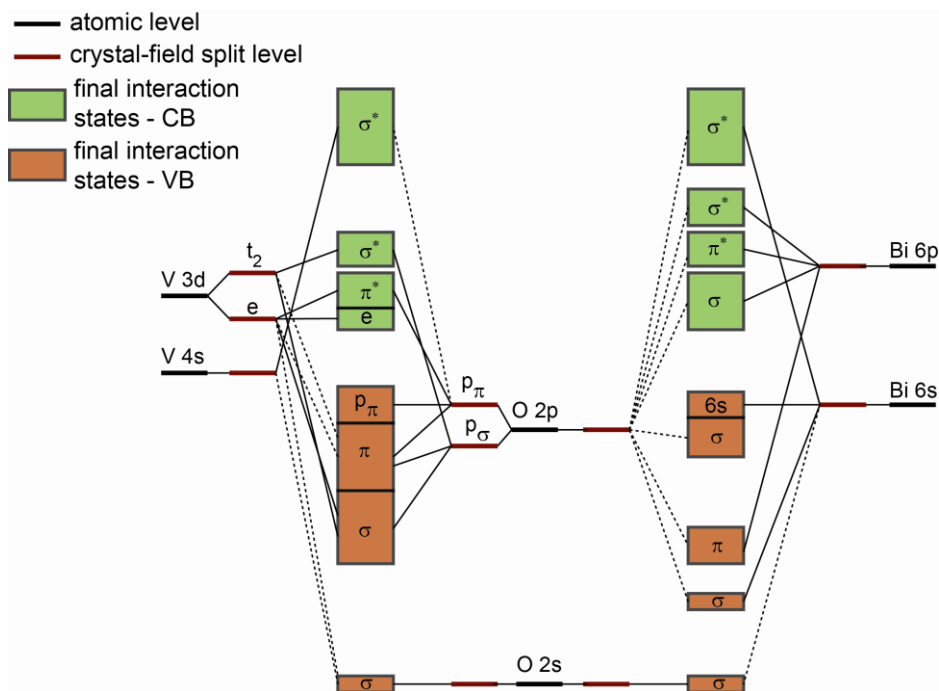


**Figure 1.11.** Molecular-orbital bonding diagram of monoclinic scheelite  $\text{BiVO}_4$ .

The effective masses of carriers of the monoclinic scheelite  $\text{BiVO}_4$  are also calculated to be lower than the other type of  $\text{BiVO}_4$ . The minimum effective mass of electrons ( $m_e^*$ ) at the bottom of the conduction band is  $\sim 0.9 m_0$  ( $m_0$ : the rest mass of electron), while the minimum effective mass of holes ( $m_h^*$ ) at the top of the valence band is  $\sim 0.7 m_0$ .<sup>25</sup> These values are smaller than that of the other oxide semiconductors for photocatalysis; for example, anatase  $\text{TiO}_2$  has the effective masses of electrons and holes of  $\sim 10$  and  $0.8 m_0$ , respectively. Lighter carriers are desired since the probability to reach the interfaces is increased. This then serves as another factor in superior photocatalytic activity of monoclinic scheelite  $\text{BiVO}_4$ , as compared to the other structures.

## 1.6 This thesis

As mentioned above, photoanodes based on monoclinic scheelite  $\text{BiVO}_4$  thin films are investigated in this thesis. This material was chosen for two reasons. First, the initially reported photocatalytic activities, although still modest, were promising. Second, prior to the start of the work presented in this thesis, there were conflicting reports on the performance level of different  $\text{BiVO}_4$  photoanodes, i.e. there was limited understanding on the factors that affect its PEC performance.

The aim of the work is two-fold: (i) to investigate the performance limiting factor(s) in  $\text{BiVO}_4$  thin film photoanodes, and (ii) to introduce and demonstrate simple, low-cost, yet effective strategies to overcome these limitations. These two aims are directed towards a bigger, more general objective, which is to achieve and demonstrate highly efficient unassisted photoelectrochemical water splitting, which will be presented at the end of the thesis.

Two performance limiting factors of  $\text{BiVO}_4$  thin film photoanodes are identified. In chapter 2, hole accumulation is shown to be present at the  $\text{BiVO}_4$ /electrolyte interface under AM1.5 illumination, as a result of slow hole transfer. This can be overcome by the electrodeposition of a low-cost cobalt phosphate (Co-Pi) co-catalyst at the surface of  $\text{BiVO}_4$ . Additionally, the efficiency decrease of  $\text{BiVO}_4$  as a function of light intensity is explored, which suggests poor electron transport in  $\text{BiVO}_4$  causing electron accumulation and carrier recombination. The performance limiting factors are further addressed in chapter 3, where a complete analysis of the absorption, separation and catalytic efficiency is presented. The separation efficiency, which is related to the carrier transport properties, is shown to be limiting, and tungsten (W) is introduced as a donor-type dopant to improve the carrier concentration, and thus the conductivity. As a result, the separation efficiency as well as the photoelectrochemical performance is greatly improved.

Despite the improvement by W-doping, the separation efficiency is limited to lower than 50%. In chapter 4, the origin of this limitation is investigated by time-resolved microwave conductivity (TRMC) measurements. It is shown that further improvement of efficiency is prevented due to the low intrinsic carrier mobility in  $\text{BiVO}_4$ . The effect of W-doping to the carrier dynamics in  $\text{BiVO}_4$  is also discussed in detail.

To overcome the poor carrier separation limitation, a simple and elegant strategy is introduced in chapter 5. A homojunction based on the gradient dopant concentration is shown to improve the carrier separation efficiency due to the presence of additional band bending. A record AM1.5 photocurrent of  $3.6 \text{ mA/cm}^2$  at 1.23 V vs RHE is demonstrated, which is more than 20-fold improvement of performance as compared to the photocurrent achieved before the start of the work.

Additionally, a hybrid photoelectrode device based on this record  $\text{BiVO}_4$ -based photoanode and an amorphous silicon solar cell is fabricated to avoid the need for additional bias potential. Solar-to-hydrogen efficiencies of 3.6% and 4.9% are

achieved for the device based on single junction and double junction amorphous silicon solar cell, respectively.

The advantages of the hybrid photoelectrode concept are discussed in comparison to other PEC water splitting device architectures in chapter 6. Analysis from the point of view of the photoanode, the solar cell, and the device in conjunction are presented to formulate a general design rule for the highly efficient hybrid photoelectrode device for water splitting.

Finally, it is important to note that although the strategies presented in this thesis are shown for BiVO<sub>4</sub>-based photoanodes, they are generally applicable in other semiconductor photoelectrode materials. This thesis can therefore be used as a guideline in the development of materials for PEC water splitting. Considering that the four-year effort in this thesis has resulted in a 20-fold performance improvement and efficiency of ~5%, the solar-to-hydrogen efficiency target of 10% should be within reach in the next few years.

## 1.7 References

1. Murray, J. & King, D. Climate policy: Oil's tipping point has passed, *Nature* **481**, 433-435 (2012).
2. The Energy Report: 100% Renewable Energy by 2050, **2011**.
3. <http://co2now.org/> accessed February 2013.
4. IPCC Fourth Assessment Report: Climate Change 2007, Working Group I Report: "The Physical Science Basis", **2007**.
5. European Commission, A Roadmap for moving to a low carbon economy in 2050, **2011**.
6. "Basic research needs for solar energy utilization", report of the US Department of Energy, Office of Basic Energy Sciences, **2005**.
7. R. van de Krol, M. Grätzel, *Photoelectrochemical Hydrogen Production*, Springer **2012**.
8. Lewis, N. S. & Nocera, D. G. Powering the planet: Chemical challenges in solar energy utilization, *Proc. Nat. Acad. Sci. USA* **103**, 15729-15735 (2006).
9. Nocera, D. G. Personalized Energy presentation at PopTech 2009.
10. Haije, W. & Geerlings, H. Efficient Production of Solar Fuel Using Existing Large Scale Production Technologies, *Environ. Sci. Technol.* **45**, 8609-8610 (2011).
11. C. A. Grimes, O. K. Varghese, S. Ranjan, *Light, Water, Hydrogen - The Solar Generation of Hydrogen by Water Photoelectrolysis*, Springer **2008**.
12. K. Rajeshwar, R. McConnell, S. Licht, *Solar Hydrogen Generation - Toward a Renewable Energy Future*, Springer **2008**.

13. James, B. D. et al. Technoeconomic Analysis of Photoelectrochemical (PEC) Hydrogen Production, *DOE Report* (2009).
14. Keable, J. & Holcroft, B. Economic and Business Perspectives, *Photoelectrochemical Hydrogen Production*, 277-292 (2012).
15. A. J. Bard, L. R. Faulkner, *Electrochemical Methods*, Wiley, New York **1980**.
16. Weber, M. F. & Dignam, M. J. Splitting Water with Semiconducting Photoelectrodes Efficiency Considerations, *Int. J. Hydrogen Energy* **11**, 225-232 (1986).
17. Bolton, J. R., Strickler, S. J., & Connolly, J. S. Limiting and Realizable Efficiencies of Solar Photolysis of Water, *Nature* **316**, 495-500 (1985).
18. Murphy, A. B. et al. Efficiency of solar water splitting using semiconductor electrodes, *Int. J. Hydrogen Energy* **31**, 1999-2017 (2006).
19. Tilley, S. D., Cornuz, M., Sivula, K., & Grätzel, M. Light-Induced Water Splitting with Hematite: Improved Nanostructure and Iridium Oxide Catalysis, *Angew. Chem. Int. Ed.* **49**, 6405-6408 (2010).
20. Alexander, B. D. et al. Metal oxide photoanodes for solar hydrogen production, *J. Mater. Chem.* **18**, 2298-2303 (2008).
21. Paracchino, A. et al. Highly active oxide photocathode for photoelectrochemical water reduction, *Nature Mater.* **10**, 456-461 (2011).
22. Bierlein, J. D. & Sleight, A. W. Ferroelasticity in BiVO<sub>4</sub>, *Solid State Communications* **16**, 69-70 (1975).
23. Dreyer, G. & Tillmanns, E. Dreyerite - Natural, Tetragonal Bismuth Vanadate from Hirschhorn-Pfalz, *Neues Jahrbuch für Mineralogie-Monatshefte*, 151-154 (1981).
24. Sleight, A. W., Chen, H. Y., Ferretti, A., & Cox, D. E. Crystal-Growth and Structure of BiVO<sub>4</sub>, *Mater. Res. Bull.* **14**, 1571-1581 (1979).
25. Zhao, Z. Y., Luo, W. J., Li, Z. S., & Zou, Z. G. Density functional theory study of doping effects in monoclinic clinobisvanite BiVO<sub>4</sub>, *Physics Letters A* **374**, 4919-4927 (2010).
26. Tokunaga, S., Kato, H., & Kudo, A. Selective preparation of monoclinic and tetragonal BiVO<sub>4</sub> with scheelite structure and their photocatalytic properties, *Chem. Mater.* **13**, 4624-4628 (2001).
27. Kudo, A., Omori, K., & Kato, H. A novel aqueous process for preparation of crystal form-controlled and highly crystalline BiVO<sub>4</sub> powder from layered vanadates at room temperature and its photocatalytic and photophysical properties, *J. Am. Chem. Soc.* **121**, 11459-11467 (1999).
28. Bhattacharya, A. K., Mallick, K. K., & Hartridge, A. Phase transition in BiVO<sub>4</sub>, *Mater. Lett.* **30**, 7-13 (1997).
29. Roth, R. S. & Waring, J. L. Synthesis and Stability of Bismutotantalite, Stibiotantalite and Chemically Similar ABO<sub>4</sub> Compounds, *American Mineralogist* **48**, 1348-& (1963).
30. Walsh, A. et al. Band Edge Electronic Structure of BiVO<sub>4</sub>: Elucidating the Role of the Bi s and V d Orbitals, *Chem. Mater.* **21**, 547-551 (2009).

31. Payne, D. et al. The nature of electron lone pairs in  $\text{BiVO}_4$ , *Appl. Phys. Lett.* **98** (2011).
32. Ding, K., Chen, B., Fang, Z., & Zhang, Y. Density functional theory study on the electronic and optical properties of three crystalline phases of  $\text{BiVO}_4$ , *Theoretical Chemistry Accounts* **132**, 1-7 (2013).
33. Wadnerkar, N. & English, N. J. Density functional theory investigations of bismuth vanadate: Effect of hybrid functionals, *Computational Materials Science* **74**, 33-39 (2013).

## 2 Nature and Light Dependence of Bulk Recombination in Co-Pi-Catalyzed BiVO<sub>4</sub> Photoanodes

BiVO<sub>4</sub> is considered to be a promising photoanode material for solar water splitting applications. Its performance is limited by two main factors: slow water oxidation kinetics and poor charge separation. We confirm recent reports that cobalt phosphate (Co-Pi) is an efficient water oxidation catalyst for BiVO<sub>4</sub>, and report an AM1.5 photocurrent of 1.7 mA/cm<sup>2</sup> at 1.23 V vs. RHE for 100 nm spray-deposited, compact and undoped BiVO<sub>4</sub> films with an optimized Co-Pi film thickness of 30 nm. The charge separation of these films depends strongly on light intensity, ranging from 90% at low light intensities to less than 20% at intensities corresponding to 1 sun. These observations indicate that the charge separation efficiency in BiVO<sub>4</sub> is limited by poor electron transport, and not by the presence of bulk defect states, interface traps, or the presence of a Schottky junction at the back contact.

---

This chapter has been published: F. F. Abdi and R. van de Krol, *J. Phys. Chem. C* 116 (2012) 9398

## 2.1 Introduction

Photoelectrochemical water splitting has attracted widespread attention recently due to the potential for the clean production of H<sub>2</sub> and O<sub>2</sub> from water using sunlight. Most of these efforts have been focused on the development of binary metal oxides as semiconducting photo-electrode materials. This is mainly driven by the easy synthesis, generally good stability in aqueous solutions and relatively low cost. However, after numerous studies only a few candidates have emerged that show promising photocurrents (> 2 mA/cm<sup>2</sup>) under AM1.5 illumination: Fe<sub>2</sub>O<sub>3</sub>,<sup>1</sup> WO<sub>3</sub>,<sup>2</sup> (photo-anodes) and Cu<sub>2</sub>O (photo-cathode).<sup>3</sup> This rather limited number of options has sparked interest in the development of a new generation of photoelectrode materials based on ternary metal oxides, giving a huge number of additional possibilities.

Among the relatively few ternary metal oxides that have been explored, bismuth vanadate (BiVO<sub>4</sub>) is one of the most promising photo-anode candidates showing visible light photoactivity.<sup>4,5</sup> The photoactive phase is the monoclinic scheelite phase with a bandgap of ~2.4 eV.<sup>6</sup> This implies that as much as 11% of the solar spectrum can be absorbed, compared to 4% for the standard UV-sensitive TiO<sub>2</sub> photocatalyst. Although several efforts have been reported in employing BiVO<sub>4</sub> as a photoanode in the past 5 years,<sup>5, 7-10</sup> significant improvements of its performance have been reported only very recently.<sup>11-14</sup> Luo et al. have reported the highest photocurrent density so far: ~2.8 mA/cm<sup>2</sup> at 1.23 V<sub>RHE</sub> under AM1.5 illumination.<sup>14</sup> In order to achieve this, they had to catalyze their Mo-doped BiVO<sub>4</sub> with a prohibitively expensive rhodium oxide catalyst. Since rare-earth catalysts based on Ir, Rh or Ru are unlikely to be used in economically viable devices, many groups are now trying to develop alternative water oxidation catalysts based on earth-abundant materials, such as Co,<sup>15, 16</sup> Fe,<sup>17</sup> and Mn.<sup>18</sup> A particularly effective and easy-to-synthesize co-catalyst is the amorphous cobalt-phosphate (CoPi) catalyst developed by Nocera et al.<sup>19</sup> This catalyst has been shown to enhance the performance of Fe<sub>2</sub>O<sub>3</sub>,<sup>20-22</sup> WO<sub>3</sub>,<sup>23</sup> and several other photoanode materials under near-neutral pH conditions.<sup>24-26</sup> Very recently, during the final phase of the preparation of this manuscript, Co-Pi was reported to successfully catalyze water oxidation at doped BiVO<sub>4</sub> photoanodes.<sup>27-29</sup> Zhong et al. achieved the highest AM1.5 photocurrents so far for Co-Pi catalyzed BiVO<sub>4</sub>, reaching a value of 1.4 mA/cm<sup>2</sup> at 1.23 V<sub>RHE</sub>. They showed that the Co-Pi increases the efficiency of the water oxidation reaction to nearly 100%, and that the overall performance of their Co-Pi catalyzed W:BiVO<sub>4</sub> is limited by bulk recombination processes.<sup>28</sup> Bulk recombination is therefore the next bottleneck to be solved in the quest for efficient BiVO<sub>4</sub>-based photoanodes. The nature of this recombination process is, however, still unclear.

In this chapter, we report a new AM1.5 photocurrent benchmark of 1.7 mA/cm<sup>2</sup> (at 1.23 V<sub>RHE</sub>) for undoped, Co-Pi catalyzed BiVO<sub>4</sub> photoanodes with a thickness of only 100 nm. Moreover, we show that external quantum efficiencies as high as 90% can be reached at low light intensities, which rules out the possibility of defect-mediated bulk recombination as the main performance bottleneck in these films. Instead, we provide evidence that poor electron transport is the key issue to be addressed in BiVO<sub>4</sub>.

## 2.2 Experimental details

### Preparation of BiVO<sub>4</sub> thin film photoanode

Dense thin films of BiVO<sub>4</sub> were prepared by spray pyrolysis. The precursor solution was made by dissolving 4 mM Bi(NO<sub>3</sub>)<sub>3</sub>·5H<sub>2</sub>O (98%, Alfa Aesar) in acetic acid (98%, Sigma Aldrich), and adding an equimolar amount of vanadium in the form of VO(AcAc)<sub>2</sub> (99%, Alfa Aesar) dissolved in absolute ethanol (Sigma Aldrich). The films were sprayed onto FTO-coated glass substrates (fluorine-doped tin dioxide, 15 Ω/□, TEC-15, Hartford Glass Co.), which were cleaned by three successive 15 min. ultrasonic rinsing treatments in a Triton® solution, acetone and ethanol. The substrate temperature during spraying was maintained at 450°C, as measured by a thermocouple pressed to the top of the substrate surface. The spray deposition was carried out using an automated spray setup with Quickmist Air Atomizing Spray nozzle driven by an overpressure of 0.06 MPa of nitrogen gas. The nozzle-substrate distance was kept at 20 cm. The precursor solution was placed 20 cm below the nozzle and fed to the nozzle via the siphoning effect induced by the nitrogen gas flow. Each spray cycle consisted of 5 seconds of spray time and 55 seconds of delay time to allow solvent evaporation, and a total of 100 cycles were used to deposit the films.

Prior to deposition of the BiVO<sub>4</sub>, a SnO<sub>2</sub> interfacial layer (~80 nm) was deposited onto the FTO substrate to prevent recombination at the FTO/BiVO<sub>4</sub> interface.<sup>30, 31</sup> A 0.1 M SnCl<sub>4</sub> (99%, Acros Organics) solution in ethyl acetate (99.5%, J. T. Baker) was used as the precursor solution. The SnO<sub>2</sub> layer was deposited at 425°C using 5 spray cycles (5 s on, 55 s off) in a gravity-assisted siphoning mode, where the precursor solution was placed 30 cm above the nozzle.

After deposition, the SnO<sub>2</sub>/BiVO<sub>4</sub> samples were subjected to an additional 2-hour heat treatment in a tube furnace at 450°C in air.

### Co-Pi catalyst electrodeposition and characterization

The Co-Pi catalyst was electrodeposited onto BiVO<sub>4</sub> in an electrochemical cell using a three-electrode configuration. An aqueous 0.1 M KH<sub>2</sub>PO<sub>4</sub> (99.5%, Fluka)



solution was first prepared and titrated to pH 7 with 1 M KOH (85%, J. T. Baker). Then, 0.5 mM Co(NO<sub>3</sub>)<sub>2</sub> (99%, Acros Organics) was added, and the resulting solution was used as the electrolyte. The potential of the working electrode was controlled by a potentiostat (EG&G PAR 283). An Ag/AgCl electrode (XR300, saturated KCl+AgCl solution (KS120), Radiometer Analytical) and a coiled Pt wire were used as the reference and counter electrodes, respectively. The potentials vs Ag/AgCl were converted to the reversible hydrogen electrode (RHE) using the following relationship,

$$V_{RHE} = V_{Ag/AgCl} + V_{Ag/AgCl-NHE}^0 + 0.059 pH \quad (2.1)$$

where  $V_{Ag/AgCl-NHE}^0$  is 0.199 V at 25 °C. For the conversion to the normal hydrogen scale, NHE, the pH-dependent term of Eq. 2.1 should be ignored. The electrodeposition was carried out at constant voltage of 1.3 V<sub>NHE</sub> for varying deposition times. For thickness measurements, the Co-Pi catalyst was electrodeposited onto a bare FTO substrate following the same procedure. A profilometer (Dektak-3) was used to measure the thickness of the catalyst. The optical absorption of the catalyst was measured with a UV-Vis spectrometer (Perkin Elmer Lambda 900).

### Photoelectrochemical measurements

Photoelectrochemical characterization was carried out in an aqueous 0.5 M K<sub>2</sub>SO<sub>4</sub> (99%, Alfa Aesar) solution buffered to pH ~5.6 with 0.09 M KH<sub>2</sub>PO<sub>4</sub> (99.5%, Fluka)/0.01 M K<sub>2</sub>HPO<sub>4</sub> (99%, J. T. Baker). The measurements were done in the same three-electrode configuration as described for the Co-Pi electrodeposition. White-light photocurrent measurements were performed under simulated AM1.5 solar illumination (100 mW/cm<sup>2</sup>) with a Newport Sol3A Class AAA Solar Simulator (type 94023A-SR3). The spectrum of the simulator is shown in Figure A1 of Appendix A. The photocurrents for the Co-Pi thickness optimization experiments were measured with a different solar simulator (100 mW/cm<sup>2</sup>, EPS 1200S, KH Steuernagel Lichttechnik GmbH). Monochromatic photocurrents were measured with a 200 W quartz tungsten-halogen lamp coupled into a grating monochromator (Acton SpectraPro 150i). An electronic shutter (Uniblitz LS6) was used, and a long-pass colored glass filter (Schott, 3 mm thick) was placed between the monochromator and the sample to remove second-order diffracted light. The shutter was actuated every 10 seconds, and the photocurrent was taken as the difference between the current when the shutter is opened and closed (3 seconds integration time and ~1.5 nm step size). The light intensities ranged between 0.3 – 8 μW/cm<sup>2</sup>, as shown in Figure A2 of Appendix A. The Incident Photon to Current Efficiency (IPCE, sometimes called the External Quantum Efficiency or EQE) is then calculated based on the following formula:

$$IPCE(\%) = \frac{1240 \times j_{ph} \text{ (mA/cm}^2\text{)}}{P_{light} \text{ (mW/cm}^2\text{)} \times \lambda \text{ (nm)}} \times 100\% \quad (2.2)$$

The IPCE as a function of light intensity was measured using a combination of a 457 nm cw argon ion laser (Coherent Innova 90C Series) and multiple neutral density filters (metal film, OD 0.1-3, Melles Griot). The illumination intensities from the argon ion laser and the tungsten halogen source were measured with a calibrated photodiode (Ophir PD300-UV).

## 2.3 Results and discussion

### Photoresponse of unmodified BiVO<sub>4</sub>

Figure 2.1 shows the absorption and IPCE as a function of wavelength for a spray-deposited BiVO<sub>4</sub> photoelectrode at an applied bias of 1.23 V<sub>RHE</sub>. At these low light intensities (few μW/cm<sup>2</sup>), illumination via the substrate (back-illumination) is found to give the highest efficiencies, with IPCE values exceeding 80% between 340 and 420 nm. In the range between 360 and 440 nm, these values are nearly identical to the light harvesting efficiency (LHE). This implies internal quantum efficiencies of nearly 100%, i.e., every absorbed photon yields an electron in the outer circuit. Such high charge carrier collection efficiencies indicate that bulk recombination is virtually absent in these films. Figure 2.1 also shows that front-side illumination results in ~2 times lower quantum efficiencies than back-side illumination. Such a pronounced difference is a clear indication that the overall photoresponse is limited by the electron transport properties of the material.<sup>31, 32</sup>

It should be noted that the films show some light scattering at longer wavelengths. This indicates that the films are not perfectly smooth, which is mainly due to the roughness of the FTO substrate (vide infra). Extrapolation of the LHE curve to shorter wavelengths suggests that the amount of scattering becomes negligible at wavelengths below 450 nm, consistent with similar observations in the literature.<sup>33, 34</sup> Moreover, any contribution of scattering to the LHE below 450 nm would imply an internal quantum efficiency exceeding 100%, which is physically unrealistic.

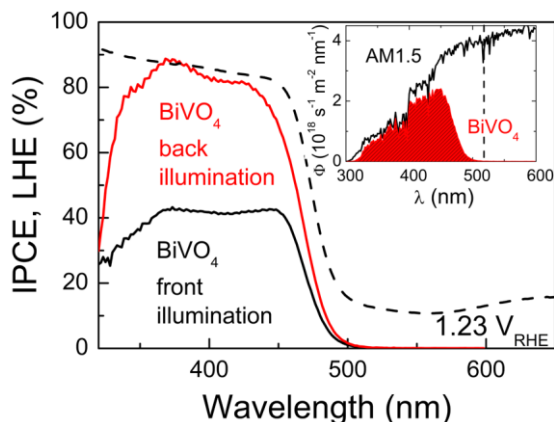


**Figure 2.1.** Incident Photon to Current Efficiency (IPCE) of a  $\text{BiVO}_4$  photoanode under front- (black) and back-side illumination (red) at  $1.23 \text{ V}_{\text{RHE}}$ . The dashed line represents the Light Harvesting Efficiency (LHE) of the same electrode, i.e., the absorbance spectrum. The inset shows the product of the IPCE of  $\text{BiVO}_4$  under back illumination with the AM1.5 solar spectrum. The dashed vertical line in the inset corresponds to the absorption edge of  $\text{BiVO}_4$ .

Multiplying the IPCE with the AM1.5 solar spectrum (red area in inset of Fig. 2.1) and subsequently integrating this over the appropriate wavelength range allows us to estimate the expected photoresponse under 1 sun illumination. The predicted AM1.5 photocurrent density is  $3.6 \text{ mA/cm}^2$  at  $1.23 \text{ V}_{\text{RHE}}$ , which is only a factor of 2 below the theoretical maximum value of  $7.5 \text{ mA/cm}^2$  for  $\text{BiVO}_4$  with a bandgap of 2.4 eV. The actual measurements shown in Figure 2.2a, however, reveal a much lower AM1.5 photocurrent than predicted: at  $1.23 \text{ V}_{\text{RHE}}$ , the photocurrent is  $0.6 \text{ mA/cm}^2$  (solid black curve), 6 times less than the predicted value. The large anodic current transient after switching on the light (Fig. 2.2b, black curve) indicates that the difference between the predicted and observed photocurrent density is caused by extensive electron-hole recombination.

Initially, one might expect poor electron transport to be the cause of the recombination. However, in contrast to the IPCE results shown in Figure 2.1, the difference between front- and back-side illumination is found to be negligible under these high light intensity conditions (Figure A3, Appendix A). This means that poor electron transport can be ruled out as the cause of recombination. We attribute this to photodoping of the material. At high illumination intensities, the generation rate approaches or exceeds the rate at which the electrons can be transported to the back contact. The resulting accumulation of electrons increases the electronic conductivity of the material and thereby eliminates the electron transport limitation.

The main cause of recombination in these BiVO<sub>4</sub> films at high illumination intensities is slow kinetics of water oxidation, i.e., slow hole transfer across the semiconductor/electrolyte interface. This causes photogenerated holes to accumulate near the surface, which increases the chance of recombination with the electrons. This explanation is supported by the photocurrent transients shown in Figure 2.2b (black curve). The decrease in photocurrent shortly after the light is turned on is due to recombination of the photogenerated electrons with the accumulated holes. When turning off the light, the accumulated holes react with free electrons in the conduction band. This causes electrons to be withdrawn from the external circuit, which explains the transient cathodic response.

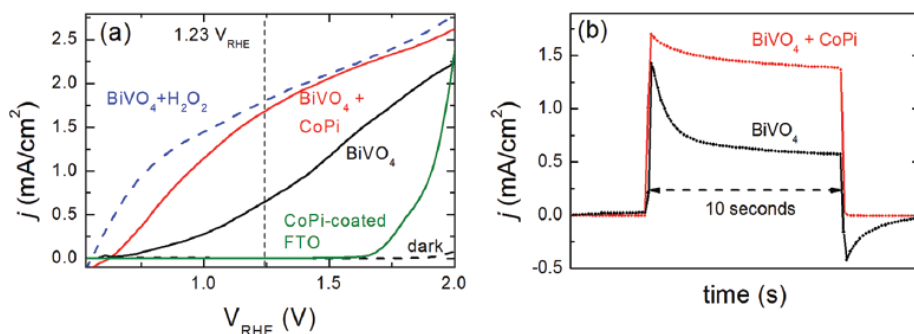


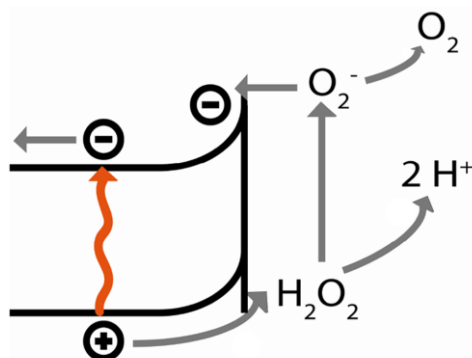
**Figure 2.2.** (a) AM1.5 (class AAA solar simulator) photocurrent vs. voltage for a BiVO<sub>4</sub> photoelectrode (with and without H<sub>2</sub>O<sub>2</sub> in the electrolyte) and a Co-Pi catalyzed BiVO<sub>4</sub> photoelectrode at a scan rate of 50 mV/s. The reference curve for Co-Pi coated FTO confirms the true photovoltaic nature of the photocurrents in BiVO<sub>4</sub>, and rules out that they are caused by photoconductivity effects. (b) Chopped AM1.5 chronoamperometry plot of uncatalyzed and Co-Pi catalyzed BiVO<sub>4</sub> photoelectrodes under back-side illumination at 1.23 V<sub>RHE</sub>.

To confirm that slow oxidation kinetics are responsible for the poor photoresponse, 0.5 M H<sub>2</sub>O<sub>2</sub> was added into the electrolyte as a hole scavenger.<sup>35-37</sup> H<sub>2</sub>O<sub>2</sub> has a much higher oxidation rate constant than water, which is due to its more negative reduction potential (+0.68 V<sub>RHE</sub> vs. +1.23 V<sub>RHE</sub>, respectively),<sup>37</sup> and the fact that only two holes are needed to oxidize it (vs. 4 holes for H<sub>2</sub>O oxidation). Figure 2.2a shows an AM1.5 photocurrent density of 1.8 mA/cm<sup>2</sup> at 1.23 V<sub>RHE</sub> after adding H<sub>2</sub>O<sub>2</sub>, which represents an impressive ~3-fold increase. This proves that slow water oxidation kinetics are indeed the performance-limiting factor for BiVO<sub>4</sub> under high light intensities. Interestingly, only a minor increase in photocurrent is observed for IPCE measurements in the presence of H<sub>2</sub>O<sub>2</sub> (not shown). The reason is that these measurements were carried out using much lower light intensities (few μW/cm<sup>2</sup>), and

under these conditions the rate of both  $\text{H}_2\text{O}$  and  $\text{H}_2\text{O}_2$  oxidation can still keep up with the supply of photo-generated holes.

It should be noted that the addition of  $\text{H}_2\text{O}_2$  into the electrolyte may be accompanied by current doubling,<sup>38-40</sup> a phenomenon that causes the oxidized form of  $\text{H}_2\text{O}_2$  to be oxidized again through injection of an electron into the conduction band of  $\text{BiVO}_4$ . The oxidation steps are illustrated in Scheme 2.1 and can be described by the following reactions:  $\text{H}_2\text{O}_2 + \text{h}^+ \rightarrow 2\text{H}^+ + \text{O}_2^-$ ;  $\text{O}_2^- \rightarrow \text{O}_2 + \text{e}^-$ . Although the possibility of current doubling cannot be completely ruled out, the 3-fold increase in photocurrent at 1.23  $V_{\text{RHE}}$  clearly shows that hole scavenging by  $\text{H}_2\text{O}_2$  improves the photocurrent by at least a factor of 1.5.

**Scheme 2.1.** Illustration of current doubling in the presence of  $\text{H}_2\text{O}_2$ , in which the oxidized form of  $\text{H}_2\text{O}_2$  (a superoxide anion) is oxidized again by electron injection into the conduction band of the semiconductor.



### Co-Pi catalyst deposition and properties

In order to improve the performance of the photoelectrode without the addition of sacrificial agents such as  $\text{H}_2\text{O}_2$ , a Co-Pi catalyst is deposited on the surface of the  $\text{BiVO}_4$  photoelectrode. Following the approach introduced by Nocera et al.,<sup>19</sup> we electrodeposited Co-Pi on  $\text{BiVO}_4$  in a 0.1 M KPi + 0.5 mM  $\text{Co}(\text{NO}_3)_2$  electrolyte solution at 1.3  $V_{\text{NHE}}$  (1.7  $V_{\text{RHE}}$ ) for different deposition times. Typical cyclic voltammetry and chronoamperometry plots of the Co-Pi electrodeposition step are shown in Figure A4 and A5 of Appendix A, respectively.

Since Co-Pi films have a brownish color, they should be kept thin enough to allow enough light to reach the underlying  $\text{BiVO}_4$  film. Figure 2.3a shows the absorption spectrum of Co-Pi, measured for a 275 nm thick film deposited on FTO. Based on an average absorption coefficient of  $\sim 3 \times 10^6 \text{ m}^{-1}$ , the Co-Pi thickness should be less than 35 nm to ensure that >90% of the incident light reaches the  $\text{BiVO}_4$ .

Now that the absorption coefficient of Co-Pi is known, the growth of the Co-Pi film can be monitored in situ and in a quantitative manner by optical transmission measurements. As shown in Figure 2.3b, the thickness increases linearly with the amount of charge at a deposition potential of 1.1 V<sub>NHE</sub> (1.5 V<sub>RHE</sub>). This confirms that at this potential, little or no interference from water oxidation occurs.<sup>41</sup> Assuming that all the charge is used to oxidize the Co<sup>2+</sup> ions in the electrolyte to Co<sup>3+</sup> in the Co-Pi, and assuming a Co:K:P composition of 2.7:1:1 in Co-Pi,<sup>42,43</sup> we estimate the effective gravimetric density of the Co-Pi film to be ~3 g/cm<sup>3</sup>.

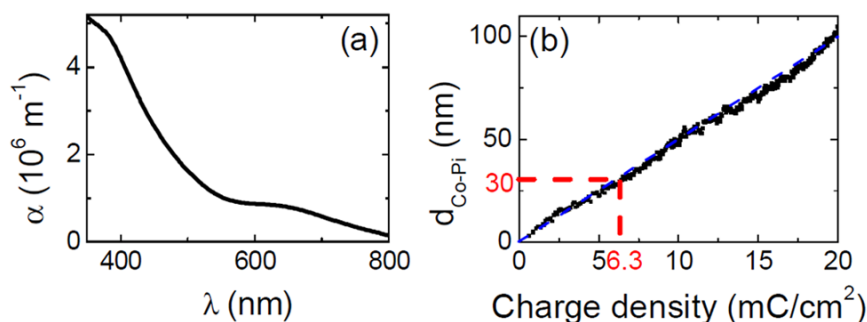


**Figure 2.3.** (a) Absorption coefficient of Co-Pi catalyst as a function of wavelength. (b) Correlation of Co-Pi catalyst thickness to the charge consumed during electrodeposition at 1.1 V<sub>NHE</sub> (1.5 V<sub>RHE</sub>).

#### Photoresponse of Co-Pi catalyzed BiVO<sub>4</sub>

Figure 2.4a shows that a Co-Pi thickness of 30 nm, obtained after 15 min. of electrodeposition (Fig. A5, Appendix A), gives the highest photocurrent density and is therefore the optimum thickness for Co-Pi on BiVO<sub>4</sub>. A cross-section SEM image of the sample, shown in Figure 2.4b, reveals complete coverage of the BiVO<sub>4</sub> surface. A likely explanation for the optimum of 30 nm is that thinner films may give incomplete coverage, while hole transport through the Co-Pi layer may become a problem for thicker films.

It should be noted that the thickness values in Fig. 2.4a are determined by step profilometry on CoPi films deposited on FTO. Deposition of these films on BiVO<sub>4</sub> under the same conditions (potential, deposition time, electrolyte) result in the same film thickness. This is evidenced by the nearly identical I-V curves of Co-Pi deposition on FTO and on BiVO<sub>4</sub> (Fig. A4, Appendix A), and confirmed by the fact that the same thickness (~30 nm) was found for CoPi deposited at 1.3 V<sub>NHE</sub> for 15 min. on FTO and BiVO<sub>4</sub> (Figs. A5b and c, Appendix A).

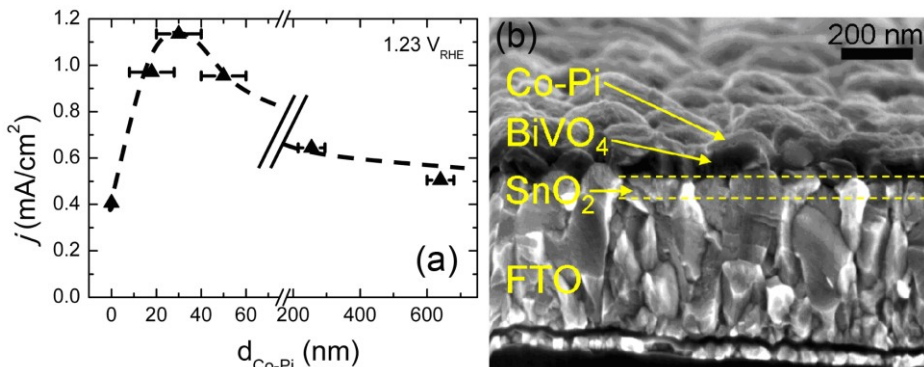


**Figure 2.4.** (a) Photocurrent density as a function of Co-Pi catalyst thickness on a BiVO<sub>4</sub> photoanode, indicating that 30 nm is the optimum thickness of the catalyst. The photocurrents were measured under simulated sunlight (100 mW/cm<sup>2</sup>) using back-side illumination. (b) Cross-section Scanning Electron Microscope (SEM) image of a 30 nm thick Co-Pi catalyzed BiVO<sub>4</sub> photoelectrode.

As shown in Figure 2.2a (red curve), a 30 nm Co-Pi catalyst film on BiVO<sub>4</sub> increases the AM1.5 photocurrent by a factor of ~3, resulting in a value of 1.7 mA/cm<sup>2</sup> at 1.23 V<sub>RHE</sub>. This photocurrent can be reproducibly achieved with our spray recipe, with variations less than 10% for different samples. Although the shift of the photocurrent onset potential is less pronounced than for the H<sub>2</sub>O<sub>2</sub> curve, the steeper increase in photocurrent at potentials positive of the onset potential clearly illustrates the improved catalytic activity for water oxidation. This strongly reduces the amount of hole accumulation near the semiconductor/electrolyte interface, as evidenced by the much less pronounced photocurrent transients shown in Figure 2.2b (red curve). While the photocurrent reported here is lower than the state-of-the-art photocurrent density of 2.8 mA/cm<sup>2</sup> recently reported for RhO<sub>2</sub>-catalyzed Mo:BiVO<sub>4</sub>,<sup>14</sup> our result has been obtained for a 10-times thinner compact film (~100 nm) and a low-cost, earth-abundant co-catalyst. Moreover, no dopant was used for the BiVO<sub>4</sub>. The photocurrent we report here exceeds the recently reported values of 1.1 and 1.4 mA/cm<sup>2</sup> (both also at 1.23 V<sub>RHE</sub>) for Co-Pi catalyzed Mo- and W-doped BiVO<sub>4</sub>, respectively.<sup>28, 29</sup>

To ensure that the Co-Pi catalyst itself is not oxidized by the photo-generated holes, we compare the photocurrent with the amount of charge needed to electrodeposit the Co-Pi. Integration of the photocurrent density recorded during a cyclic voltammogram gave a total charge of 234 mC/cm<sup>2</sup>, which is ~40 times larger than the charge needed to deposit the 30 nm-thick catalyst film (Figure 2.3b). This confirms that the Co-Pi indeed acts as a catalyst.

### Light intensity dependence

To further elucidate the influence of light intensity on the photoresponse of  $\text{BiVO}_4$ , we measured the Absorbed Photon to Current Efficiency (APCE, sometimes called Internal Quantum Efficiency or IQE) at different light intensities with a 457 nm cw argon ion laser in combination with multiple neutral density filters. The resulting APCE values as a function of the number of absorbed photons (which is proportional to the number of photo-generated charge carriers and the light intensity) are shown in Figure 2.5. The APCE decreases with increasing light intensity for both non-catalyzed and Co-Pi catalyzed  $\text{BiVO}_4$  photoelectrodes. However, at an electron-hole generation rate that corresponds to 1 sun ( $\sim 10^{16} \text{ s}^{-1} \text{ cm}^{-2}$ ), the Co-Pi catalyzed  $\text{BiVO}_4$  shows a 3 times higher APCE than the non-catalyzed  $\text{BiVO}_4$ . This is indeed consistent with the 3-fold increase in photocurrent observed in Figure 2.2a. The Co-Pi catalyst thus clearly provides an alternative, faster pathway for water oxidation at the surface of the  $\text{BiVO}_4$  photoelectrode.

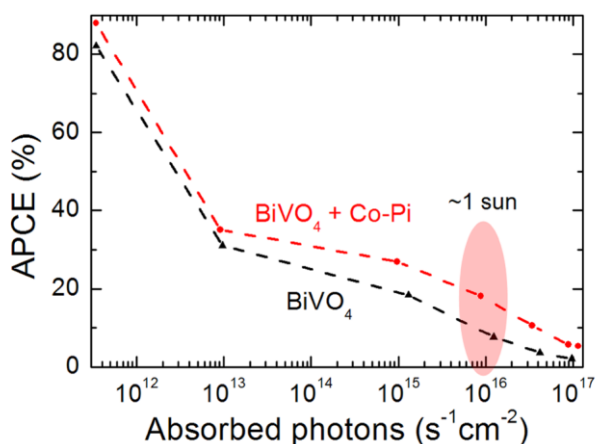


**Figure 2.5.** APCE of  $\text{BiVO}_4$  and Co-Pi catalyzed  $\text{BiVO}_4$  photoelectrodes as a function of the number of photons absorbed, measured with a 457 nm cw argon ion laser at a potential of  $1.23 V_{\text{RHE}}$ .

Despite the improvements by the Co-Pi, the data shown in Figure 2.5 indicate that a significant fraction ( $\sim 80\%$ ) of the photo-generated charge carriers still recombine at high light intensities. Assuming that the  $\text{H}_2\text{O}_2$  captures 100% of the holes arriving at the surface,<sup>28, 37</sup> the data in Figure 2.2a suggest that little—if anything—can be gained from further optimization of the water oxidation catalyst. Further efforts to improve  $\text{BiVO}_4$  should therefore be directed towards improving charge separation in the bulk.<sup>28</sup>



Possible factors affecting the charge separation efficiency are i) charge trapping at the interface with the back-contact, ii) recombination at bulk defects, iii) the presence of a Schottky barrier at the back-contact, or iv) charge accumulation due to slow electron and/or hole transport kinetics. In our case, charge trapping at the interface with the FTO back-contact is prevented by the presence of an interfacial  $\text{SnO}_2$  layer between the FTO and the  $\text{BiVO}_4$ . We recently showed that this layer prevents recombination by acting as a “hole mirror”.<sup>31</sup> Recombination via trapping at bulk defects or through electron accumulation in the bulk due to the presence of a Schottky barrier can also be ruled out; these effects would also occur at low light intensities, which is inconsistent with the high internal quantum efficiencies ( $\sim 100\%$ ) that we observe in Figure 2.1.

Instead, we believe that the bulk recombination in Co-Pi catalyzed  $\text{BiVO}_4$  at high light intensities is caused by electron accumulation in the conduction band. Electron transport in  $\text{BiVO}_4$  is known to be slow,<sup>31</sup> and at high illumination intensities the generation rate may exceed the rate at which they can be transported to the back contact. The electrons then accumulate in the conduction band, which decreases the space charge width, reduces the charge separation efficiency, and therefore increases the recombination rate.

We can now summarize our findings as follows. The photoresponse of unmodified  $\text{BiVO}_4$  at low light intensities is limited by the poor electron transport properties of the material. At high light intensities, electron accumulation in the conduction band increases the conductivity of the material (photodoping) and slow oxygen evolution kinetics now limit the performance. This limitation can be removed by depositing a Co-Pi catalyst on the surface of  $\text{BiVO}_4$ . Under these conditions, slow electron transport again limits the performance.

Finally, it is important to realize that the bias voltage needed to get reasonable photocurrents from  $\text{BiVO}_4$  severely reduces the overall energy conversion efficiency (any claims of which should *only* be made for two-electrode measurements under short-circuit conditions<sup>44</sup>). A bias voltage of 1.23 V vs. RHE—the somewhat arbitrary potential used by most researchers to allow easy comparison of results from different labs—corresponds to the thermodynamic potential for water splitting, and the solar-to-hydrogen conversion efficiency for a single  $\text{BiVO}_4$  photoelectrode biased at this potential is therefore zero. This is of course true for *all* metal oxide photoanodes, including  $\text{Fe}_2\text{O}_3$  and  $\text{WO}_3$ , but this important point is not always mentioned in the literature. The photoanode does, however, provide the *overpotential* that is needed to drive the kinetics of the water oxidation reaction. To illustrate the importance of this contribution, Figure 2.2a also shows a voltammogram in which the  $\text{BiVO}_4$  photoanode is replaced by a Co-Pi coated FTO electrode, which has a high electro-catalytic activity for water oxidation. The current at 1.23 V vs. RHE is only  $\sim 10 \mu\text{A}/\text{cm}^2$ , and a potential of  $\sim 2$  V is required to achieve a water splitting current of  $1.7 \text{ mA}/\text{cm}^2$ .

For practical energy conversion devices, metal oxide photoanodes such as BiVO<sub>4</sub> should be operated in a tandem cell configuration. The bias voltage in such a device is generated by a photovoltaic cell placed behind the photoanode, using the unabsorbed light that passes through. In such a configuration, our compact BiVO<sub>4</sub> films show an important advantage over most other highly efficient photoanodes: they are not nanostructured and show little light scattering (~15% at  $\lambda > 500$  nm). Although extensive scattering can sometimes be avoided in nanostructured electrodes,<sup>45</sup> this is not always possible. Any scattering would prevent the unabsorbed light to reach the PV cell behind the photoanode, and greatly reduce the overall efficiency.<sup>46</sup> When combined with a PV cell that generates 1.23 V from light transmitted by BiVO<sub>4</sub>, solar-to-hydrogen conversion efficiencies of 2.1% ( $1.23 \text{ V} \times 1.7 \text{ mA/cm}^2 / 100 \text{ mW/cm}^2$ ) can be readily achieved with the Co-Pi-catalyzed BiVO<sub>4</sub> electrode reported here.

## 2.4 Conclusions

In summary, we have demonstrated AM1.5 photocurrents of 1.7 mA/cm<sup>2</sup> at 1.23 V<sub>RHE</sub> for low-cost spray-deposited BiVO<sub>4</sub> films catalyzed with a 30 nm Co-Pi water oxidation catalyst. These dense compact films show little scattering, which is an important advantage in tandem device configurations based on a BiVO<sub>4</sub> photoanode placed in front of a PV junction. The high internal quantum efficiencies (close to 100%) at low light intensities indicate efficient charge separation. Trapping at bulk defects or interface states is negligible for these films, and the presence of a Schottky barrier at the back contact can be ruled out. The extensive recombination observed at high light intensities is due to the poor electron transport properties of BiVO<sub>4</sub>. Future efforts on this material should therefore be aimed to address this key issue. Recent studies show that doping with W or Mo improves the properties to some extent.<sup>28, 29</sup> However, to fully realize the potential of BiVO<sub>4</sub>, additional strategies based on guest-host nanostructures<sup>47</sup> in combination with plasmonic or resonance absorption enhancement<sup>48</sup> should be explored.

## 2.5 References

1. Tilley, S. D., Cornuz, M., Sivula, K., & Grätzel, M. Light-Induced Water Splitting with Hematite: Improved Nanostructure and Iridium Oxide Catalysis, *Angew. Chem. Int. Ed.* **49**, 6405-6408 (2010).

2. Solarzka, R., Krolikowska, A., & Augustynski, J. Silver Nanoparticle Induced Photocurrent Enhancement at WO<sub>3</sub> Photoanodes, *Angew. Chem. Int. Ed.* **49**, 7980-7983 (2010).
3. Paracchino, A. et al. Highly active oxide photocathode for photoelectrochemical water reduction, *Nature Mater.* **10**, 456-461 (2011).
4. Kudo, A., Ueda, K., Kato, H., & Mikami, I. Photocatalytic O<sub>2</sub> evolution under visible light irradiation on BiVO<sub>4</sub> in aqueous AgNO<sub>3</sub> solution, *Catal. Lett.* **53**, 229-230 (1998).
5. Sayama, K. et al. Photoelectrochemical decomposition of water into H<sub>2</sub> and O<sub>2</sub> on porous BiVO<sub>4</sub> thin-film electrodes under visible light and significant effect of Ag ion treatment, *J. Phys. Chem. B* **110**, 11352-11360 (2006).
6. Tokunaga, S., Kato, H., & Kudo, A. Selective preparation of monoclinic and tetragonal BiVO<sub>4</sub> with scheelite structure and their photocatalytic properties, *Chem. Mater.* **13**, 4624-4628 (2001).
7. Chatchai, P. et al. FTO/SnO<sub>2</sub>/BiVO<sub>4</sub> composite photoelectrode for water oxidation under visible light irradiation, *Electrochem. Solid State Lett.* **11**, H160-H163 (2008).
8. Li, M. T., Zhao, L. A., & Guo, L. J. Preparation and photoelectrochemical study of BiVO<sub>4</sub> thin films deposited by ultrasonic spray pyrolysis, *Int. J. Hydrogen Energy* **35**, 7127-7133 (2010).
9. Long, M. C., Cai, W. M., & Kisch, H. Visible light induced photoelectrochemical properties of n-BiVO<sub>4</sub> and n-BiVO<sub>4</sub>/p-CO<sub>3</sub>O<sub>4</sub>, *J. Phys. Chem. C* **112**, 548-554 (2008).
10. Dall'Antonia, L. H. et al. Electrosynthesis of Bismuth Vanadate Photoelectrodes, *Electrochem. Solid State Lett.* **13**, D29-D32 (2010).
11. Berglund, S. P. et al. Photoelectrochemical Oxidation of Water Using Nanostructured BiVO<sub>4</sub> Films, *J. Phys. Chem. C* **115**, 3794-3802 (2011).
12. Sayama, K. et al. Effect of Carbonate Ions on the Photooxidation of Water over Porous BiVO<sub>4</sub> Film Photoelectrode under Visible Light, *Chem. Lett.* **39**, 17-19 (2010).
13. Hong, S. J., Lee, S., Jang, J. S., & Lee, J. S. Heterojunction BiVO<sub>4</sub>/WO<sub>3</sub> electrodes for enhanced photoactivity of water oxidation, *Energy Environ. Sci.* **4**, 1781-1787 (2011).
14. Luo, W. J. et al. Solar hydrogen generation from seawater with a modified BiVO<sub>4</sub> photoanode, *Energy Environ. Sci.* **4**, 4046-4051 (2011).
15. Kay, A., Cesar, I., & Grätzel, M. New benchmark for water photooxidation by nanostructured alpha-Fe<sub>2</sub>O<sub>3</sub> films, *J. Am. Chem. Soc.* **128**, 15714-15721 (2006).
16. Yin, Q. S. et al. A Fast Soluble Carbon-Free Molecular Water Oxidation Catalyst Based on Abundant Metals, *Science* **328**, 342-345 (2010).
17. Fillol, J. L. et al. Efficient water oxidation catalysts based on readily available iron coordination complexes, *Nature Chemistry* **3**, 807-813 (2011).

18. Boppana, V. B. R. & Jiao, F. Nanostructured MnO<sub>2</sub>: an efficient and robust water oxidation catalyst, *Chem. Commun.* **47**, 8973-8975 (2011).
19. Kanan, M. W. & Nocera, D. G. In situ formation of an oxygen-evolving catalyst in neutral water containing phosphate and Co<sup>2+</sup>, *Science* **321**, 1072-1075 (2008).
20. Zhong, D. K., Sun, J. W., Inumaru, H., & Gamelin, D. R. Solar Water Oxidation by Composite Catalyst/alpha-Fe<sub>2</sub>O<sub>3</sub> Photoanodes, *J. Am. Chem. Soc.* **131**, 6086-+ (2009).
21. Zhong, D. K. et al. Photo-assisted electrodeposition of cobalt-phosphate (Co-Pi) catalyst on hematite photoanodes for solar water oxidation, *Energy Environ. Sci.* **4**, 1759-1764 (2011).
22. Zhong, D. K. & Gamelin, D. R. Photoelectrochemical Water Oxidation by Cobalt Catalyst ("Co-Pi")/alpha-Fe<sub>2</sub>O<sub>3</sub> Composite Photoanodes: Oxygen Evolution and Resolution of a Kinetic Bottleneck, *J. Am. Chem. Soc.* **132**, 4202-4207 (2010).
23. Seabold, J. A. & Choi, K. S. Effect of a Cobalt-Based Oxygen Evolution Catalyst on the Stability and the Selectivity of Photo-Oxidation Reactions of a WO<sub>3</sub> Photoanode, *Chem. Mater.* **23**, 1105-1112 (2011).
24. Steinmiller, E. M. P. & Choi, K. S. Photochemical deposition of cobalt-based oxygen evolving catalyst on a semiconductor photoanode for solar oxygen production, *Proc. Nat. Acad. Sci. USA* **106**, 20633-20636 (2009).
25. Pijpers, J. J. H. et al. Light-induced water oxidation at silicon electrodes functionalized with a cobalt oxygen-evolving catalyst, *Proc. Nat. Acad. Sci. USA* **108**, 10056-10061 (2011).
26. Young, E. R. et al. Photo-assisted water oxidation with cobalt-based catalyst formed from thin-film cobalt metal on silicon photoanodes, *Energy Environ. Sci.* **4**, 2058-2061 (2011).
27. Ye, H., Park, H. S., & Bard, A. J. Screening of Electrocatalysts for Photoelectrochemical Water Oxidation on W-Doped BiVO<sub>4</sub> Photocatalysts by Scanning Electrochemical Microscopy, *J. Phys. Chem. C* **115**, 12464-12470 (2011).
28. Zhong, D. K., Choi, S., & Gamelin, D. R. Near-Complete Suppression of Surface Recombination in Solar Photoelectrolysis by "Co-Pi" Catalyst-Modified W:BiVO<sub>4</sub>, *J. Am. Chem. Soc.* **133**, 18370-18377 (2011).
29. Pilli, S. K. et al. Cobalt-phosphate (Co-Pi) catalyst modified Mo-doped BiVO<sub>4</sub> photoelectrodes for solar water oxidation, *Energy Environ. Sci.* **4**, 5028-5034 (2011).
30. Liang, Y. Q., Enache, C. S., & van de Krol, R. Photoelectrochemical characterization of sprayed alpha-Fe<sub>2</sub>O<sub>3</sub> thin films: Influence of Si doping and SnO<sub>2</sub> interfacial layer, *International Journal of Photoenergy*, 739864 (2008).
31. Liang, Y. Q., Tsubota, T., Mooij, L. P. A., & van de Krol, R. Highly Improved Quantum Efficiencies for Thin Film BiVO<sub>4</sub> Photoanodes, *J. Phys. Chem. C* **115**, 17594-17598 (2011).

32. Lindquist, S. E., Finnstrom, B., & Tegner, L. Photoelectrochemical Properties of Polycrystalline TiO<sub>2</sub> Thin Film Electrodes on Quartz Substrates, *J. Electrochem. Soc.* **130**, 351 (1983).
33. Banerjee, S., Mohapatra, S. K., & Misra, M. Synthesis of TaON nanotube arrays by sonoelectrochemical anodization followed by nitridation: a novel catalyst for photoelectrochemical hydrogen generation from water, *Chemical Communications*, 7137-7139 (2009).
34. Chen, X. et al. Application of weak ferromagnetic BiFeO<sub>3</sub> films as the photoelectrode material under visible-light irradiation, *Applied Physics Letters* **91** (2007).
35. Itoh, K. & Bockris, J. O. Thin-Film Photoelectrochemistry - Iron-Oxide, *J. Electrochem. Soc.* **131**, 1266-1271 (1984).
36. Duret, A. & Grätzel, M. Visible light-induced water oxidation on mesoscopic alpha-Fe<sub>2</sub>O<sub>3</sub> films made by ultrasonic spray pyrolysis, *J. Phys. Chem. B* **109**, 17184-17191 (2005).
37. Dotan, H. et al. Probing the photoelectrochemical properties of hematite (alpha-Fe<sub>2</sub>O<sub>3</sub>) electrodes using hydrogen peroxide as a hole scavenger, *Energy Environ. Sci.* **4**, 958-964 (2011).
38. Theuwis, A., Vermeir, I. E., & Gomes, W. P. Chemical and electrochemical interaction of acidic H<sub>2</sub>O<sub>2</sub> solutions with (100) InP, *J. Electroanal. Chem.* **410**, 31-42 (1996).
39. Fujishima, A., Kato, T., Maekawa, E., & Honda, K. Mechanism of the Current Doubling Effect .1. the ZnO Photoanode in Aqueous-Solution of Sodium Formate, *Bulletin Of The Chemical Society Of Japan* **54**, 1671-1674 (1981).
40. Gerischer, H., Muller, N., & Haas, O. On the Mechanism of Hydrogen Evolution at GaAs Electrodes, *J. Electroanal. Chem.* **119**, 41-48 (1981).
41. Surendranath, Y., Kanan, M. W., & Nocera, D. G. Mechanistic Studies of the Oxygen Evolution Reaction by a Cobalt-Phosphate Catalyst at Neutral pH, *J. Am. Chem. Soc.* **132**, 16501-16509 (2010).
42. Surendranath, Y., Dinca, M., & Nocera, D. G. Electrolyte-Dependent Electrosynthesis and Activity of Cobalt-Based Water Oxidation Catalysts, *J. Am. Chem. Soc.* **131**, 2615-2620 (2009).
43. Kanan, M. W. et al. Structure and Valency of a Cobalt-Phosphate Water Oxidation Catalyst Determined by in Situ X-ray Spectroscopy, *J. Am. Chem. Soc.* **132**, 13692-13701 (2010).
44. Chen, Z. B. et al. Accelerating materials development for photoelectrochemical hydrogen production: Standards for methods, definitions, and reporting protocols, *J. Mater. Res.* **25**, 3-16 (2010).
45. Brilliet, J., Grätzel, M., & Sivula, K. Decoupling Feature Size and Functionality in Solution-Processed, Porous Hematite Electrodes for Solar Water Splitting, *Nano Lett.* **10**, 4155-4160 (2010).

46. Brillet, J. et al. Examining architectures of photoanode-photovoltaic tandem cells for solar water splitting, *J. Mater. Res.* **25**, 17-24 (2010).
47. Sivula, K., Le Formal, F., & Grätzel, M. WO<sub>3</sub>-Fe<sub>2</sub>O<sub>3</sub> Photoanodes for Water Splitting: A Host Scaffold, Guest Absorber Approach, *Chem. Mater.* **21**, 2862-2867 (2009).
48. Linic, S., Christopher, P., & Ingram, D. B. Plasmonic-metal nanostructures for efficient conversion of solar to chemical energy, *Nature Mater.* **10**, 911-921 (2011).

### **3 Efficient BiVO<sub>4</sub> Thin Film Photoanodes Modified with Cobalt Phosphate Catalyst and W-doping**

Bismuth vanadate (BiVO<sub>4</sub>) thin film photoanodes for light-induced water oxidation are deposited by a low-cost and scalable spray pyrolysis method. The resulting films are of high quality, as indicated by an internal quantum efficiency close to 100% between 360 and 450 nm. However, its performance under AM1.5 illumination is limited by slow water oxidation kinetics. This can be addressed by using cobalt phosphate (Co-Pi) as a water oxidation co-catalyst. Electrodeposition of 30 nm Co-Pi catalyst on the surface of BiVO<sub>4</sub> increases the water oxidation efficiency from ~30% to more than 90% at potentials higher than 1.2 V vs RHE. Once the surface catalysis limitation is removed, the performance of the photoanode is limited by low charge separation efficiency; more than 60% of the electron-hole pairs recombine before reaching the respective interfaces. Slow electron transport is shown to be the main cause of this low efficiency. We show that this can be remedied by introducing W as a donor type dopant in BiVO<sub>4</sub>, resulting in an AM1.5 photocurrent of ~2.3 mA/cm<sup>2</sup> at 1.23 V vs RHE for 1% W-doped Co-Pi-catalyzed BiVO<sub>4</sub>.

---

This chapter has been published: F. F. Abdi, N. Firet, and R. van de Krol, *ChemCatChem* 5 (2013) 490

### 3.1 Introduction

In order to achieve a 100% renewable energy-driven society by 2050, as recently envisioned by WWF,<sup>1</sup> the quest for new sustainable energy sources remains one of the biggest challenges. Sunlight has always been the most promising option, giving enough energy in an hour to fulfil the world's annual energy need. However, finding highly efficient and economically viable routes to harvest and use this energy source presents a formidable scientific challenge. One of the most elegant methods is photoelectrochemical water splitting, which produces hydrogen and oxygen. Hydrogen, the most simple of all solar fuels, can then be re-oxidized in a fuel cell or a combustion engine. The products of this oxidation process are energy and pure water, which makes this cycle both sustainable and renewable. To photo-electrochemically produce hydrogen, one needs to find a semiconductor material that absorbs light, separates the charge carriers, and catalyzes the water splitting half-reactions at the surface. Moreover, the material needs to be stable in aqueous solutions, and should not be prohibitively expensive.<sup>2</sup> The challenge is to find a material that fulfils all these requirements simultaneously.

Metal oxide semiconductors have drawn significant attention as photoelectrode materials. Although their semiconducting properties are usually rather poor compared to group IV or III-V semiconductors, they are generally stable in aqueous solutions, easily synthesized, and cheap. Their low carrier mobilities and short carrier lifetimes can be overcome by adopting suitable nanostructured morphologies. This approach has been particularly successful for  $\alpha$ -Fe<sub>2</sub>O<sub>3</sub> and WO<sub>3</sub>.<sup>3,4</sup> In fact, the numerous studies on metal oxide photoelectrodes in the past few decades have been focused almost exclusively on binary metal oxides. Only a few of these, most notably Fe<sub>2</sub>O<sub>3</sub>, WO<sub>3</sub> and Cu<sub>2</sub>O, can be identified as promising,<sup>5-7</sup> and none meet all the stringent requirements outlined above.<sup>2</sup> We therefore need to expand our materials database and include more complex multinary metal oxides.

Bismuth vanadate (BiVO<sub>4</sub>) is one of the most promising complex metal oxide photoanodes known thus far. Kudo et al. first showed that the monoclinic phase of BiVO<sub>4</sub> shows high visible light photoactivity.<sup>8,9</sup> The material has a bandgap of 2.4 eV,<sup>10</sup> and can absorb up to 11% of the solar spectrum. This means BiVO<sub>4</sub> can theoretically generate an AM1.5 photocurrent of 7.5 mA/cm<sup>2</sup>, assuming all photons with energies higher than 2.4 eV are absorbed. This corresponds to a solar-to-hydrogen energy conversion efficiency of 9%. Moreover, its conduction band edge is located close to the reversible hydrogen electrode (RHE) level,<sup>11-13</sup> which enables water splitting at modest external bias potentials. Nevertheless, the first efforts to apply BiVO<sub>4</sub> as a photoelectrode material have been hampered by fairly small



efficiencies, resulting in AM1.5 photocurrents less than 1 mA/cm<sup>2</sup>.<sup>11, 14-17</sup> Very recently, its performance has been greatly enhanced by modifying the material with oxygen evolution co-catalysts.<sup>18-26</sup> These include traditional noble metal catalysts such as IrO<sub>2</sub> and RhO<sub>2</sub>,<sup>27-29</sup> but also several exciting new oxygen evolution catalysts based on earth-abundant elements.<sup>23, 30</sup> However, little is known about the factor(s) that limit the performance of BiVO<sub>4</sub> after the slow water oxidation kinetics are addressed.

Our efforts have focussed on the use of a low-cost spray pyrolysis technique to deposit high-quality BiVO<sub>4</sub> films.<sup>26, 31, 32</sup> This technique is highly scalable, an important requirement for large-scale production of solar energy conversion devices. To illustrate this: for a full conversion to a solar-driven society in 2050 based on 10% efficient devices and with 24/7/365 production starting now, production rates in the order of 500 m<sup>2</sup>/s are required. This is one order of magnitude higher than the global spray-paint rate in the automotive industry (15 m<sup>2</sup>/s),<sup>33</sup> challenging, but certainly not impossible.

In this chapter, we demonstrate the high photocurrents that can be achieved with spray-deposited BiVO<sub>4</sub>. We first confirm earlier observations by showing that poor electronic conductivity and slow water oxidation kinetics are also limiting the performance of the latest generation of BiVO<sub>4</sub> films presented here. Next, quantitative insight into these limitations is obtained by unravelling the charge separation and water oxidation efficiencies, following an interesting approach that was recently reported by others. Based on these insights, we then address the poor electronic conductivity of BiVO<sub>4</sub> by doping our films with tungsten. We show that this results in a new performance record for BiVO<sub>4</sub> modified with a low-cost, earth-abundant water oxidation catalyst.

## 3.2 Experimental details

### Preparation of BiVO<sub>4</sub> and W-doped BiVO<sub>4</sub> thin film photoanodes

Dense thin films of BiVO<sub>4</sub> were prepared by spray pyrolysis. A BiVO<sub>4</sub> precursor solution was prepared by dissolving Bi(NO<sub>3</sub>)<sub>3</sub>·5H<sub>2</sub>O (98%, Alfa Aesar) in acetic acid (98%, Sigma Aldrich) and VO(AcAc)<sub>2</sub> (99%, Alfa Aesar) in absolute ethanol (Sigma Aldrich). The Bi solution was then added to the V solution, and the mixture was diluted to 4 mM with excess ethanol. For the preparation of W-doped BiVO<sub>4</sub> films, varying amounts of W(OC<sub>2</sub>H<sub>5</sub>)<sub>6</sub> (5% w/v in C<sub>2</sub>H<sub>5</sub>OH, 99.8% Alfa Aesar) were added to the precursor solution of Bi and V, resulting in a mixture containing Bi:(V+W) in a 1:1 ratio. To prevent premature oxidation by trace amounts of water, 1 vol% of triethyl orthoformate (TEOF, 98%, Fluka Analytical) was added to the mixture (TEOF converts to ethanol when reacting with water). The substrates are FTO-coated glass

(15  $\Omega/\square$ , TEC-15, Hartford Glass Co.), which had been cleaned by three successive 15 min. ultrasonic rinsing steps in 10 vol% Triton®, acetone, and ethanol. The substrates were placed on a heating plate that was set to 450 °C during deposition. The spray nozzle (Quickmist Air Atomizing Spray) was placed 20 cm above the heating plate and driven by an overpressure of 0.6 bar of nitrogen gas. A pulsed deposition mode was used, with one spray cycle consisting of 5 seconds of spray time followed by a delay of 55 seconds to allow solvent evaporation. The BiVO<sub>4</sub> thickness was controlled by the number of spray cycles, with a deposition rate of ~1 nm per cycle. Prior to BiVO<sub>4</sub> or W-doped BiVO<sub>4</sub> deposition, an ~80 nm SnO<sub>2</sub> layer was spray-deposited onto the FTO substrate to prevent recombination of electrons and holes at the FTO/BiVO<sub>4</sub> interface.<sup>26,32</sup> As a final step, the SnO<sub>2</sub>/BiVO<sub>4</sub> and SnO<sub>2</sub>/W-doped BiVO<sub>4</sub> samples were annealed for 2 hours at 450 °C in air to further improve the crystallinity.

### Co-Pi catalyst electrodeposition

A 30 nm Co-Pi catalyst was electrodeposited on the surface of BiVO<sub>4</sub> or W-doped BiVO<sub>4</sub> according to the recipe from Kanan and Nocera.<sup>30</sup> The electrolyte is made by dissolving 0.5 mM Co(NO<sub>3</sub>)<sub>2</sub> (99%, Acros Organics) in a 0.1 M KPi solution (pH~7). The potential of the working electrode was controlled by a potentiostat (EG&G PAR 283). A coiled Pt wire and an Ag/AgCl electrode (XR300, saturated KCl and AgCl solution, Radiometer Analytical) were used as the counter and reference electrodes, respectively. The electrodeposition was carried out at a constant voltage of 1.3 V<sub>NHE</sub> (1.7 V<sub>RHE</sub>) for 15 minutes.

### Photoelectrochemical measurements

Photoelectrochemical characterization was carried out using the same three-electrode configuration as described above. Two different electrolytes were used: (i) an aqueous 0.5 M K<sub>2</sub>SO<sub>4</sub> (99%, Alfa Aesar) solution buffered to pH ~5.6 with K<sub>2</sub>HPO<sub>4</sub> (99%, J.T. Baker) and KH<sub>2</sub>PO<sub>4</sub> (99.5%, Fluka), and (ii) an aqueous 0.1 M KPi solution (pH~7). White-light photocurrent measurements were performed under simulated AM1.5 solar illumination (100 mW/cm<sup>2</sup>) with a Newport Sol3A Class AAA solar simulator (type 94023A-SR3). Monochromatic photocurrents were measured with a 200 W quartz tungsten-halogen lamp coupled into a grating monochromator (Acton SpectraPro 150i). The monochromatic light intensities were measured with a calibrated photodiode (Ophir PD300-UV) and ranged between 0.3 and 8  $\mu\text{W}/\text{cm}^2$ .

### 3.3 Results and discussion

#### Photoelectrochemical characterization of BiVO<sub>4</sub> thin films

Figure 3.1a shows a photograph of a 100 nm BiVO<sub>4</sub> film on an F-doped SnO<sub>2</sub> (FTO) substrate (left) next to a bare FTO substrate (right). The yellow color indicates the presence of BiVO<sub>4</sub>, and only a small amount of scattering is shown by the sample. The microstructure of the film is characterized using planar and cross-sectional scanning electron microscopy, shown in Figure 3.1b and c, respectively. A typical particle size of ~100 nm is observed, which is much smaller than that of earlier samples prepared by less well-defined glass spray nozzles.<sup>32</sup>

Despite the simplicity of spray pyrolysis process, high quality BiVO<sub>4</sub> films can be made with this technique. This is evidenced by the high absorbed photon-to-current efficiency (APCE, also referred to as the *internal* quantum efficiency)<sup>34</sup> values shown in Figure 3.1d. In the wavelength range between 360 and 450 nm, the APCE values exceed 90% under back-illumination (illumination via the substrate). This implies that almost every absorbed photon yields an electron in the outer circuit. Such high carrier collection efficiencies indicate that there are few – if any – bulk and/or interface defects in the film that act as recombination centers.<sup>26</sup>

Another important observation from Figure 3.1d is that back-illumination results in ~2 times higher efficiencies than front-illumination (illumination via the electrolyte). The difference between the front- and back-illumination experiments is the location in the sample where the electron-hole pairs are generated; all other experimental conditions are the same. Under front-illumination, the holes are generated close to the semiconductor/electrolyte interface, while the electrons have to traverse the entire film in order to reach the back-contact. For back-illumination the situation is reversed; now the holes have to travel the longest distance. The observation that front-illumination gives the lowest photocurrent implies that electron transport is the performance-limiting factor in this material.<sup>26, 32</sup>

It should be noted that the APCE values were measured under relatively low light intensities of a few  $\mu\text{W}/\text{cm}^2$ . When extrapolating these quantum efficiencies to 1 sun ( $100 \text{ mW}/\text{cm}^2$ ),<sup>35</sup> a photocurrent of  $3.6 \text{ mA}/\text{cm}^2$  is predicted at 1.23 V vs. RHE. However, the actual measurements shown in Figure 3.2 (black curve) show a photocurrent of  $0.7 \text{ mA}/\text{cm}^2$ , which is a factor of ~5 lower. This is due to the slow water oxidation kinetics at the surface of BiVO<sub>4</sub>; at these high light intensities, charge transfer across the semiconductor/electrolyte interface simply cannot keep up with the rate at which the holes are generated. The oxidation kinetics can be greatly enhanced by electro-depositing a cobalt phosphate (Co-Pi) catalyst at the surface of the BiVO<sub>4</sub>. As shown by the red curve in Figure 3.2, this results in a ~2.6-times increase in photocurrent to  $\sim 1.8 \text{ mA}/\text{cm}^2$  at 1.23 V vs RHE. At lower potentials, the relative

increase is even higher, up to a factor of  $\sim 30$  at 0.75 V vs RHE. This clearly demonstrates the exceptional water oxidation activity of the Co-Pi catalyst.

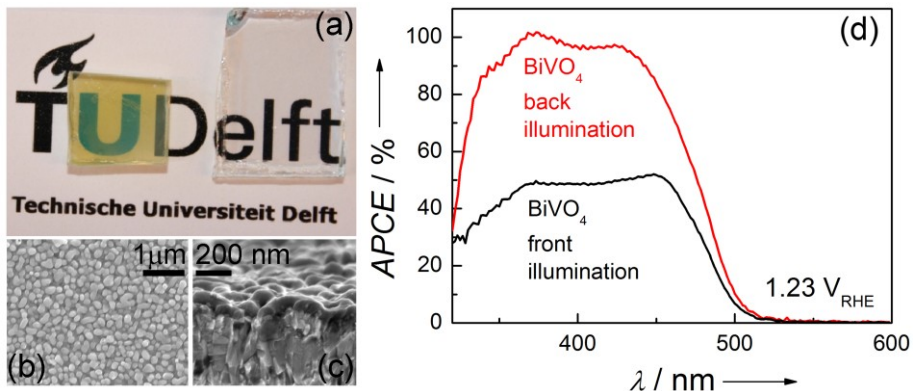


**Figure 3.1.** (a) Photograph of 100 nm thick BiVO<sub>4</sub> on an FTO-substrate (left) and a bare FTO-substrate (right). (b) Planar, and (c) cross-section scanning electron microscopy images of 100 nm thick BiVO<sub>4</sub> sample. (d) Absorbed photon-to-current efficiency (APCE) of a BiVO<sub>4</sub> photoanode under front-side (black) and back-side (red) illumination at 1.23 V vs RHE.

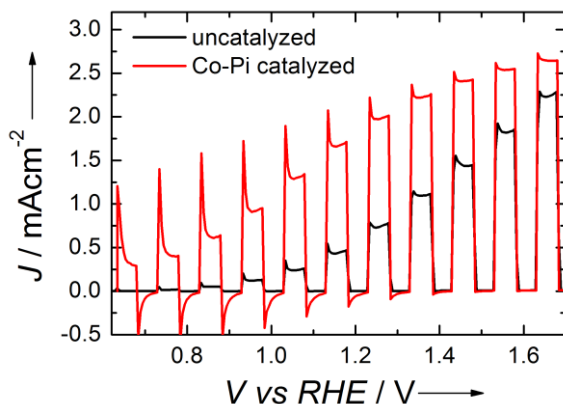


**Figure 3.2.** Chopped AM1.5 photocurrent-voltage measurement of uncatalyzed (black) and Co-Pi-catalyzed (red) BiVO<sub>4</sub> (200 nm thick) under back-side illumination. The scan rate is 10 mV/s.

In spite of the large enhancement of the catalytic activity, the red curve in Figure 3.2 still shows pronounced photocurrent transients at potentials lower than  $\sim 1.2$  V vs RHE. Such transients are a signature of slow water oxidation kinetics.<sup>[33]</sup> We attribute

this to sub-optimal coverage of the BiVO<sub>4</sub> with Co-Pi during the electrodeposition process. It has been shown that this problem can be remedied by performing *photo-assisted* electrodeposition of the Co-Pi, which ensures that the Co-Pi is deposited at those surface sites where the photo-generated holes are most readily available.<sup>18, 21, 36</sup>

### Performance-limiting factor of Co-Pi-catalyzed BiVO<sub>4</sub>

To further improve the performance of the photoanode, it is important to first determine the rate-limiting factor of the Co-Pi-catalyzed BiVO<sub>4</sub>. An elegant way to analyze the performance of a photoelectrode has recently been reported by Dotan et al.<sup>37</sup> The total water splitting photocurrent can be described by the following equation:

$$J_{H_2O} = J_{abs} \times \eta_{separation} \times \eta_{catalysis} \quad (3.1)$$

where  $J_{abs}$  is the photon absorption rate expressed as a current,  $\eta_{separation}$  is the charge separation efficiency, and  $\eta_{catalysis}$  is the catalytic efficiency for water oxidation at the surface. When hydrogen peroxide (H<sub>2</sub>O<sub>2</sub>) is added into the electrolyte, it acts as a highly effective hole scavenger.<sup>37-39</sup> This results in a 100% surface catalytic efficiency ( $\eta_{catalysis} = 1$ ) resulting in the following expression:

$$J_{H_2O_2} = J_{abs} \times \eta_{separation} \quad (3.2)$$

Based on equations 3.1 and 3.2, the charge separation efficiency and the surface catalytic efficiency can now be obtained from the following equations:

$$\eta_{separation} = \frac{J_{H_2O_2}}{J_{abs}} \quad (3.3)$$

$$\eta_{catalysis} = \frac{J_{H_2O}}{J_{H_2O_2}} \quad (3.4)$$

$J_{abs}$  is determined by multiplying the AM1.5G spectrum with the absorption spectrum, followed by integration over the wavelength.  $J_{H_2O_2}$  and  $J_{H_2O}$  must be measured. Figure 3.3a shows continuous photocurrent-voltage curves of 100 nm thick BiVO<sub>4</sub> sample in a normal electrolyte (black curve) and in the presence of 0.5 M H<sub>2</sub>O<sub>2</sub> (blue curve). The photocurrent of a Co-Pi-catalyzed sample is also shown (red curve). The rather positive onset potential of ~0.6 V vs RHE—BiVO<sub>4</sub>'s conduction band edge

is reported to be close to the RHE level<sup>11-13</sup>—is due to the overpotentials needed to compensate internal potential drops and to enhance the reaction kinetics at the surface. Based on these curves, the catalytic efficiency and the charge separation efficiency values of the samples are calculated using Eqs. 3.3 and 3.4. The results are shown in Figure 3.3b. At potentials positive of 1.2 V vs RHE, the catalytic efficiency exceeds 90%, i.e., it is nearly ideal. At low potentials, however, the catalytic efficiency drops sharply. This is consistent with the photocurrent transients observed in Figure 3.2, where the presence of both positive and negative spikes represent a signature of hole accumulation at the semiconductor/electrolyte interface.<sup>34, 40, 41</sup> As mentioned earlier, improvement may be achieved by performing *photo-assisted* electrodeposition of Co-Pi. The low catalytic efficiency and poor charge separation efficiency at potentials below ~0.75 V vs RHE also explain why the addition of the Co-Pi only results in a modest negative shift of the photocurrent onset potential.

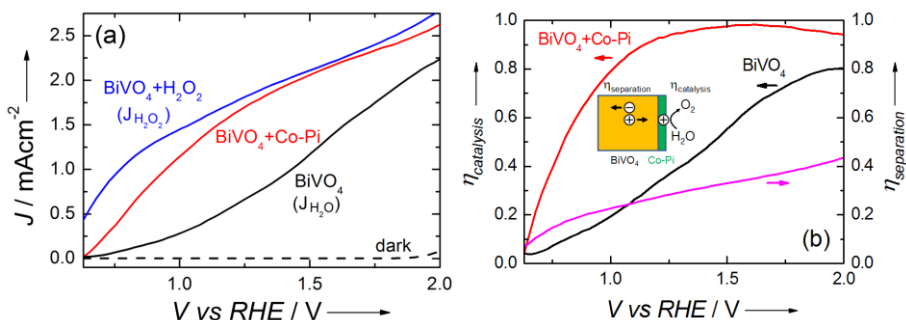


**Figure 3.3. (a)** AM1.5 photocurrent vs voltage for a 100 nm thick  $\text{BiVO}_4$  photoanode (with and without  $\text{H}_2\text{O}_2$  in the electrolyte) and a Co-Pi-catalyzed  $\text{BiVO}_4$  photoanode. The scan rate is 50 mV/s. The black dashed line represents the dark current. **(b)** Efficiencies for water oxidation catalysis and charge separation for uncatalyzed and Co-Pi-catalyzed  $\text{BiVO}_4$  as a function of applied bias. The inset illustrates both processes.

In contrast to the catalytic efficiency, the charge separation efficiency is not affected by the electrodeposition of Co-Pi on the surface of  $\text{BiVO}_4$ . Figure 3.3b shows that the charge separation efficiency (magenta curve) is the main problem to be addressed. About 60-80% of the electron-hole pairs recombine before reaching the interfaces.

To further confirm this, we measured the charge separation efficiency as a function of the thickness of  $\text{BiVO}_4$ . The results are shown in Figure 3.4. Apart from the 50 nm film, the separation efficiency clearly increases with decreasing  $\text{BiVO}_4$  thickness. This is consistent with the notion that electron transport is slow in  $\text{BiVO}_4$ . In thinner films, electrons have to travel shorter distances which decreases the chance of recombination

and increases the separation efficiency. As shown in Figure 3.4, this trend is broken for the thinnest film (50 nm). We tentatively attribute this to the presence of a photo-inactive “dead” layer near the substrate/BiVO<sub>4</sub> interface, as previously shown for  $\alpha$ -Fe<sub>2</sub>O<sub>3</sub>.<sup>39, 42, 43</sup> The exact physical origin of this dead layer is still unclear. Possible causes are substrate-film mismatch or the presence of high defect concentrations in a thin ionic space charge near the substrate/BiVO<sub>4</sub> interface.<sup>44, 45</sup>

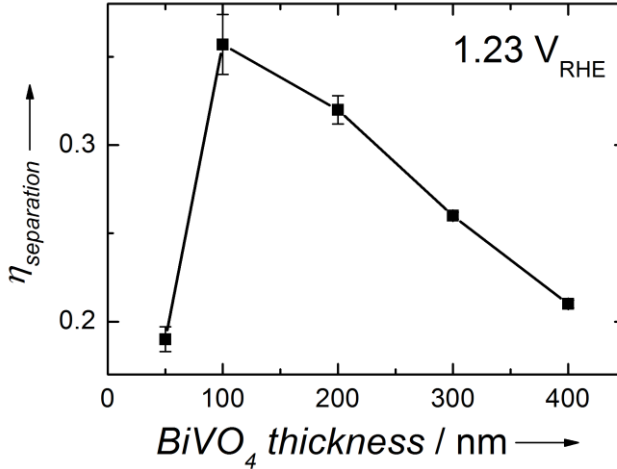


**Figure 3.4.** Charge separation efficiency of BiVO<sub>4</sub> photoanode as a function of the film thickness at applied bias of 1.23 V vs RHE.

#### W-doped BiVO<sub>4</sub> photoanodes

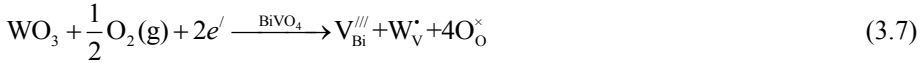
In order to improve the electron transport properties of BiVO<sub>4</sub>, its electron conductivity needs to be increased. The conductivity of a material is a function of the carrier concentration and the carrier mobility,  $\mu$ :

$$\sigma = ne\mu_e + pe\mu_h \cong ne\mu_e \quad (3.5)$$

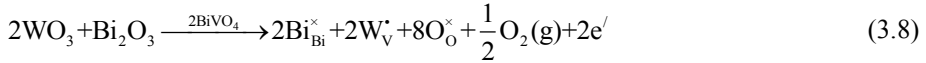
Here,  $e$  is the elementary charge, and  $n$  and  $p$  are the electron and hole concentrations, respectively. Since BiVO<sub>4</sub> is an n-type semiconductor,  $p \ll n$  so that the contribution of holes to the conductivity can be safely neglected. The carrier mobility of a material is mainly determined by its electronic band structure, and cannot be easily tuned. To increase the electronic conductivity of BiVO<sub>4</sub>, one therefore has to increase  $n$ . We do this by introducing W as a donor-type dopant. When tungsten (6 valence electrons)

substitutes for vanadium (5 valence electrons), the additional (free) electron significantly enhances the conductivity.

However, extra care has to be taken in terms of dopant incorporation in complex metal oxides such as BiVO<sub>4</sub>.<sup>34</sup> Simply adding W in the form of, for example, WO<sub>3</sub> does not produce the desired results. This is illustrated by the following defect-chemical reactions, written in the commonly-used Kröger-Vink notation:<sup>46, 47</sup>



In reaction (3.6), the W substituent is compensated by two electrically-charged vacancies, which is energetically unfavorable. In the electronic compensation reaction (3.7), the oxygen vacancy is removed. However, the consumption of electrons actually *decreases* the conductivity of BiVO<sub>4</sub>. These problems can be avoided by co-doping BiVO<sub>4</sub> with equal amounts of W and Bi:



This preserves the 1:1 stoichiometry of Bi and (W+V) sites, resulting in an overall composition of Bi(V<sub>1-x</sub>W<sub>x</sub>)O<sub>4</sub>.

The effect of adding a W dopant is illustrated by the photocurrent-voltage curves in Figure 3.5a. The 1% W-doped BiVO<sub>4</sub> (red curve) indeed shows significantly higher photocurrents than the undoped film (black curve). This improvement is in agreement with previous reports on W-doping of BiVO<sub>4</sub>.<sup>25, 32, 48-50</sup> We then modified the W-doped BiVO<sub>4</sub> with the Co-Pi catalyst (blue curve). This gives an even larger boost to the performance, resulting in a photocurrent of 2.3 mA/cm<sup>2</sup> at 1.23 V vs. RHE. This is significantly higher than the 1.7 mA/cm<sup>2</sup> we recently reported for Co-Pi-catalyzed undoped BiVO<sub>4</sub>, which demonstrates the beneficial influence of W-doping on the charge separation efficiency.

The influence of the tungsten concentration on the performance of BiVO<sub>4</sub> is shown in Figure 3.5b. For both uncatalyzed and Co-Pi-catalyzed BiVO<sub>4</sub>, 1% is the optimum W concentration. A lower concentration does not provide enough free electrons, while a higher concentration reduces the photocurrent due to e.g. lattice strain or even segregation of a WO<sub>3</sub> phase. An alternative, but less likely explanation for the decrease at high concentrations is that it reduces the width of the space charge region, *W*. This is the region where the separation of photo-generated electrons and holes is greatly enhanced due to the presence of an electric field. However, all efforts in the



literature to measure the donor density of  $\text{BiVO}_4$  indicate rather high values, in the order of  $10^{19}$ - $10^{20} \text{ cm}^{-3}$ .<sup>16, 49, 51</sup> For such high values (which one would indeed expect for dopant concentrations of 0.1-1%) the width of the space charge is just a few nanometers. It is doubtful that a decrease in the width of this already very narrow region significantly affects the photocurrent. Figure 3.5b also shows that the photocurrents under front- and back-illumination are about the same. This illustrates that for W-doped samples, electron transport no longer limits the photocurrent under high light intensities.

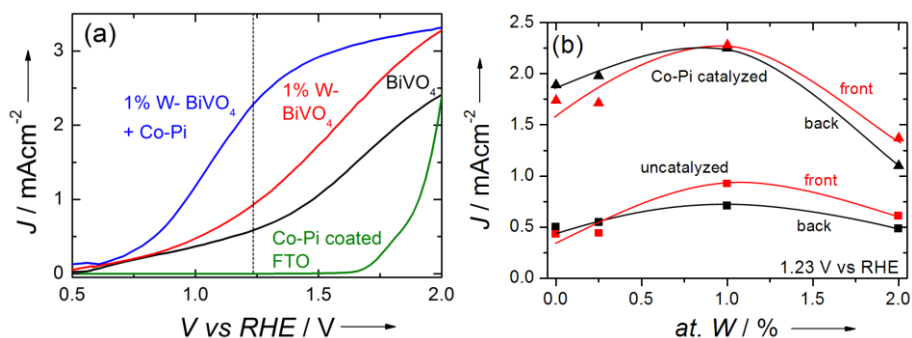


**Figure 3.5.** (a) AM1.5 photocurrent vs voltage for  $\text{BiVO}_4$ , 1% W-doped  $\text{BiVO}_4$ , and Co-Pi-catalyzed 1% W-doped  $\text{BiVO}_4$  photoanodes at a scan rate of 50 mV/s. All films are 200 nm thick. The reference curve for Co-Pi coated FTO is also shown as a confirmation of photovoltaic effect in  $\text{BiVO}_4$ . (b) AM1.5 photocurrent as a function of W concentration in uncatalyzed (■, ■) and Co-Pi catalyzed (▲, ▲)  $\text{BiVO}_4$  photoanodes under front-side (red) and back-side (black) illumination at 1.23 V vs RHE.

We now briefly compare the results of Figure 3.1d with those of Figure 3.5b for uncatalyzed, undoped  $\text{BiVO}_4$  (0% W). In Figure 3.1d, the light intensity is very low (few  $\mu\text{W}/\text{cm}^2$ ), and the surface reaction kinetics can easily keep up with the supply of photo-generated holes from the bulk. Under those conditions, the photocurrent is limited by slow electron transport in the bulk of the material, which leads to a large difference between front- and back-side illumination. In Figure 3.5b, on the other hand, the light intensity is much higher ( $100 \text{ mW}/\text{cm}^2$ ). Under such light intensities, the surface reaction kinetics can no longer keep up with the supply of photo-generated holes. Slow surface reaction kinetics then become the limiting factor, and this is not affected by the direction of illumination. For the Co-Pi catalyzed samples with 0% W in Figure 3.5b, the comparison is a bit more complicated. We believe that under these high light intensities, photo-doping can occur. This greatly enhances the electronic conductivity of the material, and explains why there is no longer a large difference

between front- and back-side illumination. For the undoped samples in Figure 3.1d, the light intensity is simply too low for photo-doping to occur.

Finally, it is important to separate the contributions of the applied bias potential and the photoanode to the overall photocurrent. Figure 3.5a also shows the photocurrent of a photo-inactive Co-Pi coated FTO electrode, which has a high electrocatalytic activity for water oxidation. In order to achieve a water splitting current of  $\sim 2.3$  mA/cm<sup>2</sup>, a potential of  $\sim 2$  V vs RHE is required. This confirms the true photovoltaic nature of the photocurrents in BiVO<sub>4</sub> and eliminates the possibility that they are caused by photoconductivity effects.

### 3.4 Conclusions

We have shown that high quality BiVO<sub>4</sub> films with internal quantum efficiencies approaching 100% can be made with a low-cost and scalable spray pyrolysis method. As previously reported, the efficiency is limited by the poor catalytic activity for oxygen evolution, which can be solved by electrodepositing a cobalt phosphate catalyst layer. The photocurrent of these catalyzed samples is then limited by a low charge separation efficiency due to the inherently slow electron transport in BiVO<sub>4</sub>. To solve this, W-doping is employed, and we found that 1% is the optimum W concentration. The combination of a Co-Pi catalyst and W-doping results in an AM1.5 photocurrent of 2.3 mA/cm<sup>2</sup> at 1.23 V vs RHE. To the best of our knowledge, this is the highest value reported thus far for a doped BiVO<sub>4</sub> photoanode modified with an earth-abundant catalyst. An important observation is that the catalytic efficiency for water oxidation is  $\sim 90\%$ . This means that little can be gained from further improvements of the catalyst. Instead, future efforts to improve the performance of BiVO<sub>4</sub> should be focused on enhancing the charge separation efficiency. Possible strategies to achieve this are the use of nanostructured heterojunctions<sup>43</sup> and/or plasmonic- or resonance-enhanced optical absorption improvements that would allow the use of thinner films.<sup>52, 53</sup>

### 3.5 References

1. The Energy Report: 100% Renewable Energy by 2050, **2011**.
2. van de Krol, R., Liang, Y. Q., & Schoonman, J. Solar hydrogen production with nanostructured metal oxides, *J. Mater. Chem.* **18**, 2311-2320 (2008).
3. Alexander, B. D. et al. Metal oxide photoanodes for solar hydrogen production, *J. Mater. Chem.* **18**, 2298-2303 (2008).

4. Sivula, K., Le Formal, F., & Grätzel, M. Solar Water Splitting: Progress Using Hematite ( $\alpha$ - $\text{Fe}_2\text{O}_3$ ) Photoelectrodes, *ChemSusChem* **4**, 432-449 (2011).
5. Paracchino, A. et al. Highly active oxide photocathode for photoelectrochemical water reduction, *Nature Mater.* **10**, 456-461 (2011).
6. Solarska, R., Krolikowska, A., & Augustynski, J. Silver Nanoparticle Induced Photocurrent Enhancement at  $\text{WO}_3$  Photoanodes, *Angew. Chem. Int. Ed.* **49**, 7980-7983 (2010).
7. Tilley, S. D., Cornuz, M., Sivula, K., & Grätzel, M. Light-Induced Water Splitting with Hematite: Improved Nanostructure and Iridium Oxide Catalysis, *Angew. Chem. Int. Ed.* **49**, 6405-6408 (2010).
8. Kudo, A., Ueda, K., Kato, H., & Mikami, I. Photocatalytic  $\text{O}_2$  evolution under visible light irradiation on  $\text{BiVO}_4$  in aqueous  $\text{AgNO}_3$  solution, *Catal. Lett.* **53**, 229-230 (1998).
9. Kudo, A., Omori, K., & Kato, H. A novel aqueous process for preparation of crystal form-controlled and highly crystalline  $\text{BiVO}_4$  powder from layered vanadates at room temperature and its photocatalytic and photophysical properties, *J. Am. Chem. Soc.* **121**, 11459-11467 (1999).
10. Tokunaga, S., Kato, H., & Kudo, A. Selective preparation of monoclinic and tetragonal  $\text{BiVO}_4$  with scheelite structure and their photocatalytic properties, *Chem. Mater.* **13**, 4624-4628 (2001).
11. Chatchai, P. et al. FTO/ $\text{SnO}_2$ / $\text{BiVO}_4$  composite photoelectrode for water oxidation under visible light irradiation, *Electrochem. Solid State Lett.* **11**, H160-H163 (2008).
12. Chen, S. & Wang, L. W. Thermodynamic Oxidation and Reduction Potentials of Photocatalytic Semiconductors in Aqueous Solution, *arXiv:1203.1970v1 [cond-mat.mtrl-sci]* (2012).
13. Hong, S. J., Lee, S., Jang, J. S., & Lee, J. S. Heterojunction  $\text{BiVO}_4/\text{WO}_3$  electrodes for enhanced photoactivity of water oxidation, *Energy Environ. Sci.* **4**, 1781-1787 (2011).
14. Berglund, S. P. et al. Photoelectrochemical Oxidation of Water Using Nanostructured  $\text{BiVO}_4$  Films, *J. Phys. Chem. C* **115**, 3794-3802 (2011).
15. Dall'Antonia, L. H. et al. Electrosynthesis of Bismuth Vanadate Photoelectrodes, *Electrochem. Solid State Lett.* **13**, D29-D32 (2010).
16. Li, M. T., Zhao, L. A., & Guo, L. J. Preparation and photoelectrochemical study of  $\text{BiVO}_4$  thin films deposited by ultrasonic spray pyrolysis, *Int. J. Hydrogen Energy* **35**, 7127-7133 (2010).
17. Long, M. C., Cai, W. M., & Kisch, H. Visible light induced photoelectrochemical properties of n- $\text{BiVO}_4$  and n- $\text{BiVO}_4/\text{p-CO}_3\text{O}_4$ , *J. Phys. Chem. C* **112**, 548-554 (2008).

18. Jeon, T. H., Choi, W., & Park, H. Cobalt-phosphate complexes catalyze the photoelectrochemical water oxidation of BiVO<sub>4</sub> electrodes, *Phys. Chem. Chem. Phys.* **13**, 21392-21401 (2011).
19. Luo, W. J. et al. Solar hydrogen generation from seawater with a modified BiVO<sub>4</sub> photoanode, *Energy Environ. Sci.* **4**, 4046-4051 (2011).
20. Pilli, S. K. et al. Cobalt-phosphate (Co-Pi) catalyst modified Mo-doped BiVO<sub>4</sub> photoelectrodes for solar water oxidation, *Energy Environ. Sci.* **4**, 5028-5034 (2011).
21. Pilli, S. K. et al. Light induced water oxidation on cobalt-phosphate (Co-Pi) catalyst modified semi-transparent, porous SiO<sub>2</sub>-BiVO<sub>4</sub> electrodes, *Phys. Chem. Chem. Phys.* **14**, 7032-7039 (2012).
22. Sayama, K. et al. Effect of Carbonate Ions on the Photooxidation of Water over Porous BiVO<sub>4</sub> Film Photoelectrode under Visible Light, *Chem. Lett.* **39**, 17-19 (2010).
23. Seabold, J. A. & Choi, K. S. Efficient and stable photo-oxidation of water by a bismuth vanadate photoanode coupled with an iron oxyhydroxide oxygen evolution catalyst, *J. Am. Chem. Soc.* **134**, 2186-2192 (2012).
24. Ye, H., Park, H. S., & Bard, A. J. Screening of Electrocatalysts for Photoelectrochemical Water Oxidation on W-Doped BiVO<sub>4</sub> Photocatalysts by Scanning Electrochemical Microscopy, *J. Phys. Chem. C* **115**, 12464-12470 (2011).
25. Zhong, D. K., Choi, S., & Gamelin, D. R. Near-Complete Suppression of Surface Recombination in Solar Photoelectrolysis by "Co-Pi" Catalyst-Modified W:BiVO<sub>4</sub>, *J. Am. Chem. Soc.* **133**, 18370-18377 (2011).
26. Abdi, F. F. & van de Krol, R. Nature and Light Dependence of Bulk Recombination in Co-Pi-Catalyzed BiVO<sub>4</sub> Photoanodes, *J. Phys. Chem. C* **116**, 9398-9404 (2012).
27. Harriman, A., Pickering, I. J., Thomas, J. M., & Christensen, P. A. Metal oxides as heterogeneous catalysts for oxygen evolution under photochemical conditions, *J. Chem. Soc., Faraday Trans. 1* **84**, 2795-2806 (1988).
28. Beni, G. et al. Electrocatalytic Oxygen Evolution on Reactively Sputtered Electrochromic Iridium Oxide-Films, *Nature* **282**, 281-283 (1979).
29. Kiwi, J. & Gratzel, M. Oxygen Evolution from Water Via Redox Catalysis, *Angewandte Chemie-International Edition in English* **17**, 860-861 (1978).
30. Kanan, M. W. & Nocera, D. G. In situ formation of an oxygen-evolving catalyst in neutral water containing phosphate and Co<sup>2+</sup>, *Science* **321**, 1072-1075 (2008).
31. Abdi, F. F., Firet, N., Dabirian, A., & van de Krol, R. Spray-deposited Co-Pi Catalyzed BiVO<sub>4</sub>: a low-cost route towards highly efficient photoanodes, *MRS Online Proceedings Library* **1446**, (2012).

32. Liang, Y. Q., Tsubota, T., Mooij, L. P. A., & van de Krol, R. Highly Improved Quantum Efficiencies for Thin Film BiVO<sub>4</sub> Photoanodes, *J. Phys. Chem. C* **115**, 17594-17598 (2011).
33. The global spray paint rate in the automotive industry of 15 m<sup>2</sup>s<sup>-1</sup> is calculated based on an annual production of ~80 million cars and commercial vehicles as reported by the OICA (International Organization of Motor Vehicle Manufacturers) in 2011, and assuming an average surface area of 6 m<sup>2</sup> per car.
34. R. van de Krol, M. Grätzel, *Photoelectrochemical Hydrogen Production*, Springer **2012**.
35. Kay, A., Cesar, I., & Grätzel, M. New benchmark for water photooxidation by nanostructured alpha-Fe<sub>2</sub>O<sub>3</sub> films, *J. Am. Chem. Soc.* **128**, 15714-15721 (2006).
36. Steinmiller, E. M. P. & Choi, K. S. Photochemical deposition of cobalt-based oxygen evolving catalyst on a semiconductor photoanode for solar oxygen production, *Proc. Nat. Acad. Sci. USA* **106**, 20633-20636 (2009).
37. Dotan, H. et al. Probing the photoelectrochemical properties of hematite (alpha-Fe<sub>2</sub>O<sub>3</sub>) electrodes using hydrogen peroxide as a hole scavenger, *Energy Environ. Sci.* **4**, 958-964 (2011).
38. Duret, A. & Grätzel, M. Visible light-induced water oxidation on mesoscopic alpha-Fe<sub>2</sub>O<sub>3</sub> films made by ultrasonic spray pyrolysis, *J. Phys. Chem. B* **109**, 17184-17191 (2005).
39. Itoh, K. & Bockris, J. O. Thin-Film Photoelectrochemistry - Iron-Oxide, *J. Electrochem. Soc.* **131**, 1266-1271 (1984).
40. Salvador, P. & Gutierrez, C. Analysis of the transient photocurrent-time behaviour of a sintered n-SrTiO<sub>3</sub> electrode in water photoelectrolysis, *Journal of Electroanalytical Chemistry and Interfacial Electrochemistry* **160**, 117-130 (1984).
41. Peter, L. M., Li, J., & Peat, R. Surface recombination at semiconductor electrodes: Part I. Transient and steady-state photocurrents, *Journal of Electroanalytical Chemistry and Interfacial Electrochemistry* **165**, 29-40 (1984).
42. Cesar, I. et al. Influence of Feature Size, Film Thickness, and Silicon Doping on the Performance of Nanostructured Hematite Photoanodes for Solar Water Splitting, *J. Phys. Chem. C* **113**, 772-782 (2009).
43. Sivula, K., Le Formal, F., & Grätzel, M. WO<sub>3</sub>-Fe<sub>2</sub>O<sub>3</sub> Photoanodes for Water Splitting: A Host Scaffold, Guest Absorber Approach, *Chem. Mater.* **21**, 2862-2867 (2009).
44. Kliewer, K. L. & Koehler, J. S. Space Charge in Ionic Crystals .I. General Approach with Application to NaCl, *Phys. Rev.* **140**, 1226-& (1965).
45. Maier, J. Ionic-Conduction In-Space Charge Regions, *Prog. Solid St. Chem.* **23**, 171-263 (1995).
46. The defect equations are described by using the so-called Kröger-Vink notation: A<sub>site</sub><sup>charge</sup>, in which A represents the ionic defect (or V for vacancy), "site" is the

- lattice on which the defect resides (i is used for interstitial sites), and "charge" is either negative (<sup>-</sup>), positive (<sup>+</sup>), or neutral (<sup>0</sup>).
47. Y.-M. Chiang, D. Birnie III, D. W. Kingery, *Physical Ceramics*, Wiley, New York **1997**.
  48. Berglund, S. P., Rettie, A. J. E., Hoang, S., & Mullins, C. B. Incorporation of Mo and W into nanostructured BiVO<sub>4</sub> films for efficient photoelectrochemical water oxidation, *Phys. Chem. Chem. Phys.* **14**, 7065-7075 (2012).
  49. Ye, H., Lee, J., Jang, J. S., & Bard, A. J. Rapid Screening of BiVO<sub>4</sub>-Based Photocatalysts by Scanning Electrochemical Microscopy (SECM) and Studies of Their Photoelectrochemical Properties, *J. Phys. Chem. C* **114**, 13322-13328 (2010).
  50. Yin, W. J. et al. Doping properties of monoclinic BiVO<sub>4</sub> studied by first-principles density-functional theory, *Phys. Rev. B* **83** (2011).
  51. Sayama, K. et al. Photoelectrochemical decomposition of water into H<sub>2</sub> and O<sub>2</sub> on porous BiVO<sub>4</sub> thin-film electrodes under visible light and significant effect of Ag ion treatment, *J. Phys. Chem. B* **110**, 11352-11360 (2006).
  52. Linic, S., Christopher, P., & Ingram, D. B. Plasmonic-metal nanostructures for efficient conversion of solar to chemical energy, *Nature Mater.* **10**, 911-921 (2011).
  53. Warren, S. C. & Thimsen, E. Plasmonic solar water splitting, *Energy Environ. Sci.* **5**, 5133-5146 (2012).

## **4 The Origin of Slow Carrier Transport in BiVO<sub>4</sub> Thin Film Photoanodes: a time-resolved microwave conductivity study**

We unravel for the first time the origin of the slow carrier transport in BiVO<sub>4</sub>, a promising metal oxide photoanode for solar water splitting, through a time-resolved microwave conductivity (TRMC) study. The measurements reveal a carrier mobility of  $\sim 2.75 \times 10^{-2} \text{ cm}^2/\text{Vs}$  at incident photons per pulse of  $10^{11} \text{ cm}^{-2}$ , which is relatively low for a photoanode material. We show that this low mobility is related to the occurrence of higher order recombination in BiVO<sub>4</sub> at these high intensities. These results thus confirm and quantify the poor carrier transport nature in BiVO<sub>4</sub>. However, the carrier lifetime of 40 ns translates to a relatively long diffusion length of 70 nm, consistent with the high photocurrents reported for BiVO<sub>4</sub> photoanodes. Tungsten (W) doping is found to decrease the carrier mobility in BiVO<sub>4</sub> significantly, which we attribute to the introduction of intermediate-depth donor defects as carrier traps. Finally, we relate the knowledge obtained in the TRMC study to explain the difference of the current-potential (J-V) characteristics between an undoped and a W-doped BiVO<sub>4</sub>. TRMC is thereby shown to be a very informative tool in analyzing metal oxide photoelectrodes for solar water splitting.

---

This chapter has been published: F. F. Abdi, T. J. Savenije, M. M. May, B. Dam and R. van de Krol, *J. Phys. Chem. Lett.* accepted (DOI: 10.1021/jz4013257)

## 4.1 Introduction

Photoelectrochemical (PEC) water splitting provides an attractive way of converting solar energy to chemical energy by forming hydrogen and oxygen. Hydrogen can be used directly as a fuel, or it can serve as a feedstock material in the formation of hydrocarbons by a Fischer-Tropsch process.<sup>1</sup> PEC water splitting takes advantage of semiconductor materials to absorb sunlight and perform the water splitting reactions at ambient temperature and pressure. Among the different classes of materials, a lot of emphasis is placed on metal oxides—due to their general stability and low cost—, and one of the most promising metal oxide photoelectrodes is bismuth vanadate ( $\text{BiVO}_4$ ).  $\text{BiVO}_4$  absorbs UV and visible light up to 520 nm, having a direct bandgap of 2.4 eV.<sup>2</sup> The material is stable in aqueous solutions with pH between 3 and 11.<sup>3</sup> The conduction and valence band are reported to straddle the water reduction and oxidation potentials.<sup>4,5</sup>  $\text{BiVO}_4$  is, however, limited by poor carrier transport properties. At high light intensities such as AM1.5 (100 mW/cm<sup>2</sup>), this limitation causes extensive carrier accumulation and recombination.<sup>6</sup> Tungsten (W) has been implemented as a donor type dopant to improve the conductivity. However, carrier transport remains an issue, as suggested by the modest carrier separation efficiency.<sup>7,8</sup> The underlying cause of the slow carrier transport is unclear, and quantitative data on e.g. carrier mobility and lifetimes is still lacking. In this chapter we investigate the nature of the carrier transport in  $\text{BiVO}_4$  to address these issues.

The time resolved microwave conductivity (TRMC) technique is a contactless measurement of the change in reflected microwave power from a microwave cell containing the sample upon nanosecond pulsed laser illumination.<sup>9-11</sup> Based on this measurement, the sample's photo-conductance—and essentially its carrier mobility—can be determined. The technique is widely applied in analyzing  $\text{TiO}_2$ -based systems, such as dye-sensitized solar cells and nanoparticles,<sup>11-13</sup> amorphous and microcrystalline silicon,<sup>14, 15</sup> organic solar cells,<sup>16, 17</sup> and carbon nanotubes;<sup>18, 19</sup> however, few TRMC studies have yet been reported on photoelectrode materials for PEC water splitting.

Here, we report on a TRMC study on undoped and 1% W-doped  $\text{BiVO}_4$  photoanode thin films. The measurements reveal a carrier mobility value for  $\text{BiVO}_4$  which is few orders of magnitude lower than typical metal oxides, confirming the poor carrier transport nature in  $\text{BiVO}_4$ . Other than increasing the carrier concentration, W-doping also introduces intermediate-depth donor states which act as carrier traps. Based on these findings, the PEC behaviors of undoped and W-doped  $\text{BiVO}_4$  can be explained, showing that TRMC is a simple yet informative tool to analyze metal oxide photoelectrodes for PEC water splitting.



## 4.2 Experimental details

### Synthesis of BiVO<sub>4</sub> thin films

Dense thin films of BiVO<sub>4</sub> and 1% W-doped BiVO<sub>4</sub> were prepared by spray pyrolysis. A BiVO<sub>4</sub> precursor solution was prepared by dissolving Bi(NO<sub>3</sub>)<sub>3</sub>·5H<sub>2</sub>O (98%, Alfa Aesar) in acetic acid (98%, Sigma Aldrich) and VO(AcAc)<sub>2</sub> (99%, Alfa Aesar) in absolute ethanol (Sigma Aldrich). The Bi solution was then added to the V solution, and the mixture was diluted to 4 mM with excess ethanol. In the case of 1% W-doped BiVO<sub>4</sub> films, 1 at% of W(OC<sub>2</sub>H<sub>5</sub>)<sub>6</sub> (5% w/v in C<sub>2</sub>H<sub>5</sub>OH, 99.8% Alfa Aesar) were added to the precursor solution of Bi and V, resulting in a mixture containing Bi:V+W in a 1:1 ratio. 1 vol% of triethyl orthoformate (TEOF, 98%, Fluka Analytical) was added to the mixture to prevent undesired hydrolysis in the presence of small amounts of water. Bare quartz substrates (S1-UV fused silica, Esco Products) were used for the TRMC study, whereas F-doped SnO<sub>2</sub> glass (15 Ω/sq., TEC-15, Hartford Glass Co.) was used for the photocurrent measurements. Prior to the deposition, the substrates were cleaned in successive 15 min. ultrasonic rinsing steps in acetone and isopropanol. The substrates were placed on a heating plate that was set to 450 °C during deposition. The spray nozzle (Quickmist Air Atomizing Spray) was placed 20 cm above the heating plate and driven by an overpressure of 0.6 bar of nitrogen gas. A pulsed deposition mode was used, with one spray cycle consisting of 5 seconds of spray time and 55 seconds of delay time to allow solvent evaporation. Each deposition was done for 200 cycles, with a deposition rate of ~1 nm per cycle. After the deposition, both samples were annealed for 2 hours at 450 °C in air to further improve the crystallinity.

BiVO<sub>4</sub> photoanodes for the AM1.5 photocurrent-voltage measurement were prepared with the same spray pyrolysis recipe; except that ~80 nm SnO<sub>2</sub> layer was spray deposited prior to BiVO<sub>4</sub> deposition according to the previously reported procedure.<sup>6, 7</sup>

### TRMC technique

For the TRMC measurements, the samples were mounted in a microwave cavity cell and placed within the setup described elsewhere.<sup>11, 12</sup> The X-band (8.2-12.4 GHz) microwaves are generated using a Gunn diode. The presented experiments were carried out at 8.44 and 8.43 GHz for undoped and 1% W-doped BiVO<sub>4</sub>, respectively; these frequencies were found to be the resonant frequencies of the loaded cavity. During the measurements, a change in the microwave power reflected by the cavity upon nanosecond pulse laser excitation (3.5 ns FWHM),  $\Delta P/P$ , was monitored and correlated to the photoinduced change in the conductance of the sample,  $\Delta G$ , by

$$\frac{\Delta P}{P}(t) = -K\Delta G(t) \quad (4.1)$$

where  $K$  is the sensitivity factor derived from the resonance characteristics of the cavity and the dielectric properties of the medium. The change in conductance is then associated with the product of the ratio of mobile charge carriers normalized to the number of absorbed photons ( $\phi$ ) and the sum of their mobility ( $\sum\mu$ ) according to

$$\phi\sum\mu = \frac{\Delta G}{I_0\beta eF_A} \quad (4.2)$$

where  $I_0$  is the incident intensity per pulse,  $e$  is the elementary charge,  $\beta$  is a factor related to the inner dimensions of the waveguide, and  $F_A$  is the fraction of incident photons attenuated within the sample.

#### Other experimental details

Photoelectrochemical characterization was carried out using a three-electrode configuration, with an aqueous 0.1 M KPi solution (pH~7) as the electrolyte. The potential of the working electrode was controlled by a potentiostat (EG&G PAR 283). A coiled Pt wire and an Ag/AgCl electrode (XR300, saturated KCl and AgCl solution, Radiometer Analytical) were used as the counter and reference electrodes, respectively. White light photocurrent measurements were performed under simulated AM1.5 solar illumination (100 mW/cm<sup>2</sup>) with a Newport Sol3A Class AAA solar simulator (type 94023A-SR3). Structural analysis was performed with a Bruker D8 Advance X-ray diffractometer (Co-K $\alpha$ ,  $\lambda = 0.178897$  nm) equipped with a LynxEye detector in a Bragg-Brentano configuration. Scanning electron micrographs were taken with JEOL JSM 6500F Scanning Electron Microscope. The UV-vis absorption was measured inside an integrating sphere using a Perkin Elmer Lambda 900 spectrometer.

### **4.3 Results and discussion**

#### Time-resolved microwave conductivity of undoped and 1% W-doped BiVO<sub>4</sub>

Figure 4.1 shows the microwave conductance transients of undoped and 1% W-doped BiVO<sub>4</sub> obtained after a 3.5 ns laser pulse of 450 nm with an intensity of  $1.3 \times 10^{-5}$  J/cm<sup>2</sup>. The photon energy used is well above the bandgap of BiVO<sub>4</sub>; hence, the optical excitation leads to the formation of free electrons and holes in the conduction

and valence bands, respectively. The microwave conductance is given by the product of the absorbance-normalized quantum yield ( $\phi$ ) and the mobility of the carriers ( $\Sigma\mu$ ). The maximum mobility of the carriers can be obtained from the peak of the measured signal, and the lifetime of the carriers can be deduced from the decay of the signal.<sup>20</sup>

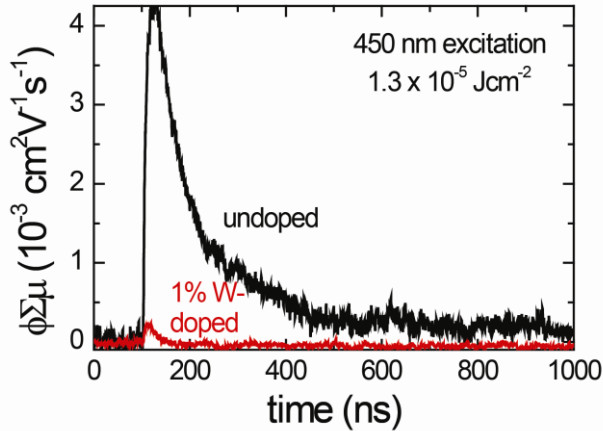


**Figure 4.1.** Time resolved microwave conductance signals recorded for undoped and 1% W-doped BiVO<sub>4</sub> thin films using a 450 nm nanosecond laser pulse of  $1.3 \times 10^{-5}$  J/cm<sup>2</sup>.

The maximum mobility of the carriers ( $\phi\Sigma\mu$ ) of undoped BiVO<sub>4</sub> as a function of incident photons per laser pulse is shown in Figure 4.2a. A carrier mobility value of  $\sim 2.75 \times 10^{-2}$  cm<sup>2</sup>/Vs is obtained at incident photons per pulse of  $10^{11}$  cm<sup>-2</sup>, which is the lowest intensity that still gives a good signal-to-noise ratio. The value of  $\phi\Sigma\mu$  decreases as the laser intensity increases, which is attributed to fast non-geminate electron-hole recombination. Based on the slope of the logarithmic plot ( $\phi\Sigma\mu \sim I_0^{1-\alpha}$ , where  $\alpha$  is the reciprocal of the order of electron-hole recombination), a combination of first and second order recombination takes place in this undoped BiVO<sub>4</sub> thin film ( $\alpha = 0.7$ ). Assuming that this recombination mechanism also occurs under AM1.5 illumination ( $\sim 10^9$  photons/cm<sup>2</sup> per pulse<sup>21</sup>), we can extrapolate the carrier mobility in Fig. 4.2a to arrive at a value of  $\sim 4.4 \times 10^{-2}$  cm<sup>2</sup>/Vs. This is a few orders of magnitude lower than typical semiconductors used for photoelectrodes in PEC water splitting.<sup>22-27</sup> This observation thus supports the poor carrier transport properties and the strong dependence of the quantum efficiency of BiVO<sub>4</sub> to the light intensity that we reported previously.<sup>6</sup>

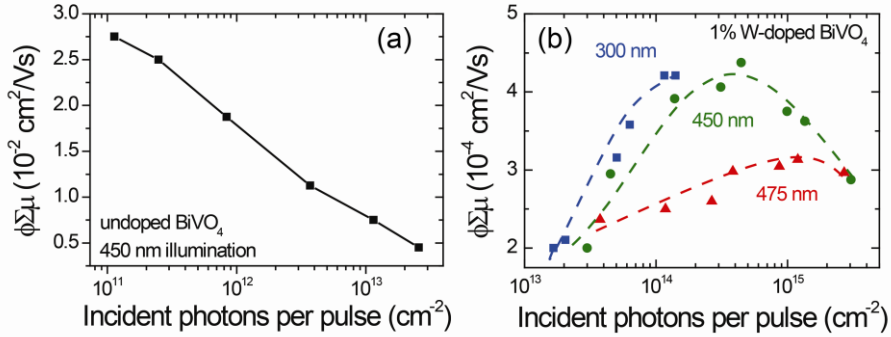


**Figure 4.2.** Maximum observed TRMC signals as a function of incident photons per laser pulse for (a) undoped  $\text{BiVO}_4$  on excitation at 450 nm, and (b) 1% W-doped  $\text{BiVO}_4$  on excitation at 300 nm (■), 450 nm (●), and 475 nm (▲). AM1.5 illumination is equivalent to an incident number of photons per pulse of  $\sim 10^9 \text{ cm}^{-2}$ .

Although the carrier mobility is low, Fig. 4.1 indicates that the lifetime of the carriers is relatively long. An exponential carrier lifetime of  $\sim 40 \text{ ns}$  is estimated for undoped  $\text{BiVO}_4$ , using fitting procedure previously reported in ref. 20 to the microwave conductance transient shown in Fig. 4.1 and taking into account the response time of the cavity. Based on the carrier lifetime,  $\tau$ , and the carrier mobility,  $\mu$ , we estimate a carrier diffusion length  $L$ , given by  $L=(D\tau)^{1/2}$  with  $D=kT\mu/e$ , of  $\sim 70 \text{ nm}$ . This suggests that despite their slow nature, the carriers are still able to reach the back and front interfaces in a thin film.

Table 4.1 summarizes the carrier lifetimes and mobilities of other promising photoelectrode materials, such as  $\text{Fe}_2\text{O}_3$ ,  $\text{WO}_3$  and  $\text{Cu}_2\text{O}$ , which are in the range of few picoseconds to few nanoseconds.<sup>28-32</sup> Although they show 1-2 orders of magnitude higher carrier mobilities, their lifetimes are 1-3 orders of magnitude shorter as compared to  $\text{BiVO}_4$ . From this, it appears that the relatively high quantum efficiencies reported for undoped  $\text{BiVO}_4$ ,<sup>6, 7</sup> are primarily due to the long lifetimes of the photogenerated charge carriers in the material.

The microwave conductance transient changes significantly upon doping with tungsten (W), as shown in Fig. 4.1. At a laser pulse intensity of  $1.3 \times 10^{-5} \text{ J/cm}^2$ , the maximum  $\phi \Sigma \mu$  for 1% W-doped  $\text{BiVO}_4$  is only  $\sim 2.2 \times 10^{-4} \text{ cm}^2/\text{Vs}$ , a factor of 20 lower than what is observed for undoped  $\text{BiVO}_4$ . Moreover, the lifetime of the carriers is reduced to  $\sim 5 \text{ ns}$ , and the TRMC signal levels off to zero after  $\sim 50 \text{ ns}$ . Despite the significant decreases in both lifetime and mobility of the photogenerated charge carriers, W-doped  $\text{BiVO}_4$  consistently show higher photocurrents than undoped samples.<sup>7, 8, 33-35</sup> The only way we can explain these seemingly contradictory results is by the enhanced electronic conductivity of the material due the tungsten dopant. This

is indeed consistent with our earlier assertion that poor electron transport limits the performance of BiVO<sub>4</sub>.

**Table 4.1.** Comparison of carrier mobility, lifetime, and diffusion length of several promising metal oxides

Photoelectrode material	Carrier mobility, $\mu$ (cm <sup>2</sup> /Vs)	Carrier lifetime, $\tau$	Diff. length, L (nm)	References
Fe <sub>2</sub> O <sub>3</sub>	0.5*	3 ps	2-4	[28-30]
WO <sub>3</sub>	10	1-9 ns*	150-500	[31]
Cu <sub>2</sub> O	6	147 ps	20	[32]
BiVO <sub>4</sub>	0.044	40 ns	70	this study

\*These values are calculated based on the other two reported properties

To understand the cause of the lower  $\phi\Sigma\mu$  values in W-doped BiVO<sub>4</sub>, the TRMC signal of 1% W-doped BiVO<sub>4</sub> was measured at different laser pulse intensities. The resulting plot of  $\phi\Sigma\mu$  as a function of incident photons per pulse is shown in Fig. 4.2b. Interestingly, the behavior is very different from what is observed for undoped BiVO<sub>4</sub> (Fig. 4.2a). At a laser excitation wavelength of 450 nm, a clear maximum of  $\sim 4 \times 10^{-4}$  cm<sup>2</sup>/Vs is observed at  $5 \times 10^{14}$  photons/cm<sup>2</sup>/pulse. A similar dependence of  $\phi\Sigma\mu$  on the light intensity has been observed in compact and mesoporous TiO<sub>2</sub> films,<sup>10, 11, 13</sup> where it is attributed to the competition between electron trap filling and higher-order recombination. We believe the same explanation applies in the case of our W-doped BiVO<sub>4</sub>. Below a flux of  $5 \times 10^{14}$  photons/cm<sup>2</sup>/pulse, the concentration of electron traps is higher than the number of absorbed photons. In this regime, the TRMC signal increases with light intensity since the chance of an electron being trapped decreases as a larger fraction of the traps get filled. When the signal reaches a maximum, the number of absorbed photons is comparable with the number of electron traps. At higher light intensities, the mobility decreases again due to the same higher order (non-geminate) recombination observed in undoped BiVO<sub>4</sub>.

Since evidence of carrier trapping is only observed in the TRMC signal of the W-doped samples, it is reasonable to assume that the nature of the traps is related to the tungsten dopant or an associated defect. Indeed, an incident intensity of  $5 \times 10^{14}$  photons/cm<sup>2</sup> in these 200 nm thick films corresponds to a carrier concentration of  $2.5 \times 10^{19}$  cm<sup>-3</sup>, which is in the order of the reported carrier concentration of W-doped BiVO<sub>4</sub>.<sup>36, 37</sup> Structural or morphological explanations for the decrease in carrier mobility can be ruled out, since no significant differences in the x-ray diffractograms, UV-vis absorption spectra or scanning electron micrographs are observed between the undoped and 1% W-doped BiVO<sub>4</sub> (Figs B1-3, Appendix B).

To further confirm the presence of electron traps in 1% W-doped BiVO<sub>4</sub>, the  $\phi\Sigma\mu$  values are also measured at different laser excitation wavelengths of 300 nm and 475

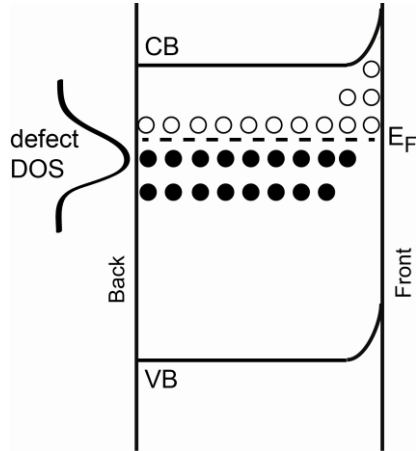
nm (Fig. 4.2b). Since the absorption coefficient of BiVO<sub>4</sub> decreases with longer wavelengths,<sup>38</sup> one would also expect the maximum of the  $\phi\Sigma\mu$  curve to shift to higher photon fluxes with longer wavelengths. This is indeed observed in Fig. 4.2b; the peak value of  $\phi\Sigma\mu$  is at 10<sup>14</sup> and 10<sup>15</sup> photons/cm<sup>2</sup> for excitation wavelengths of 300 and 475 nm, respectively.

Since the trap levels are unambiguously related to the presence of tungsten and spatially distributed throughout the entire film, we hypothesize that the electron traps are ionized (i.e., empty) tungsten donor states. Trapping of an electron in this empty donor state can be described as follows:



In order for this trapping process to be effective, the donor states cannot be too shallow and would have to be located at more than  $\sim 2kT$  below the conduction band edge. This implies that these intermediate-depth donor states are only partially filled, and that the Fermi level is located within the density-of-states (DOS) of the trap level. At the surface of the material, however, the donor level is expected to be mostly empty (ionized) due to the presence of a depletion layer. This layer usually forms upon hydroxylation of the metal oxide surface when exposed to air. No depletion layer is expected to form at the back contact due to the passivating nature of the SiO<sub>2</sub> substrate. The band diagram shown in Scheme 4.1 illustrates the partial occupation of the intermediate-depth donor states. The empty states (open circles) represent active electron traps, and it is clear from the diagram that their concentration is highest near the surface.

**Scheme 4.1.** Schematic energy band diagram of tungsten-doped BiVO<sub>4</sub>, showing the presence of defect states that could act as carrier traps. Black circles represent filled traps ( $W_V^x$ ), and white circles represent empty traps ( $W_V^\bullet$ ). CB is conduction band, VB is valence band, and  $E_F$  is Fermi energy level.



To test this model, we compare the  $\phi\Sigma\mu$  values for 1% W-doped BiVO<sub>4</sub> under front- and back-side illumination. To ensure a sufficiently sharp photon intensity profile in the film, an excitation wavelength of 300 nm was chosen; at this wavelength, the absorption depth ( $1/\alpha$ )  $\sim$  100 nm and most of the light is absorbed near one of the interfaces (Fig. B4, Appendix B). The results are shown in Fig. 4.3a. We find that front-side illumination results in  $\sim$ 30% lower  $\phi\Sigma\mu$  values compared to back-side illumination. This is indeed consistent with a larger concentration of electron traps at the surface of the material, as illustrated in Scheme 4.1. No differences between front- and back-side illumination are observed in the  $\phi\Sigma\mu$  values for undoped BiVO<sub>4</sub> (Fig. 4.3b). This is indeed expected, since no electron traps are present in the undoped material.

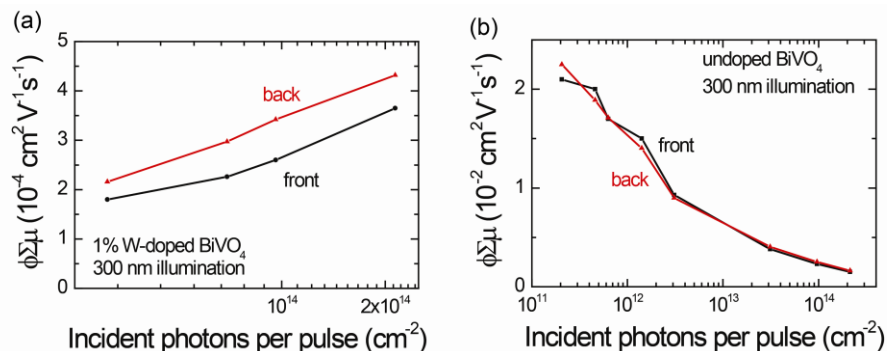


**Figure 4.3.** Maximum observed TRMC signals obtained for (a) 1% W-doped and (b) undoped BiVO<sub>4</sub> films under front- and back-side laser pulse illumination ( $\lambda=300$  nm).

#### Photoelectrochemical performance of undoped and 1% W-doped BiVO<sub>4</sub>

Finally, we relate the knowledge obtained in this study to the actual PEC performance of the BiVO<sub>4</sub> photoanodes under continuous illumination. Figure 4.5 shows the AM1.5 photocurrent-voltage (J-V) curve of both an undoped and a 1% W-doped BiVO<sub>4</sub> photoanode. Both photoanodes are modified with 30 nm thick electrodeposited cobalt phosphate (Co-Pi) catalyst to ensure fast water oxidation kinetics.<sup>7</sup> At  $V > 1.5$  V vs RHE (reversible hydrogen electrode), the photocurrent of both photoanodes approaches a plateau. The photocurrent plateau of the 1% W-doped BiVO<sub>4</sub> is  $\sim 30\%$  higher than that of the undoped BiVO<sub>4</sub>. This is consistent with the fact that poor electron transport is known to limit the photocurrent,<sup>6</sup> and that W-doping can solve this by increasing the concentration of free electrons.<sup>7</sup>

At potentials below 1 V vs RHE, however, the situation is reversed. Moreover, the photocurrent onset potential for the 1% W-doped BiVO<sub>4</sub> is  $\sim 200$  mV more positive than for the undoped BiVO<sub>4</sub>. The lower photocurrents at modest applied potentials are tentatively attributed to trapping of the photogenerated electrons in the intermediate-level donor states, followed by recombination. The comparatively steep increase of the photocurrent at more positive potentials might be a result of field-induced emission from these electron traps. One possibility is a Poole-Frenkel-type emission process, although it seems somewhat doubtful that a sufficiently strong electric field could develop in the bulk of the highly doped W:BiVO<sub>4</sub>. Another possibility is that under sufficiently large band bending, trapped electrons in the (narrow) depletion layer tunnel to nearby empty conduction band states in the bulk of the material. Further elucidation of the exact nature of these processes is beyond the scope of this study, and calls for further investigation.



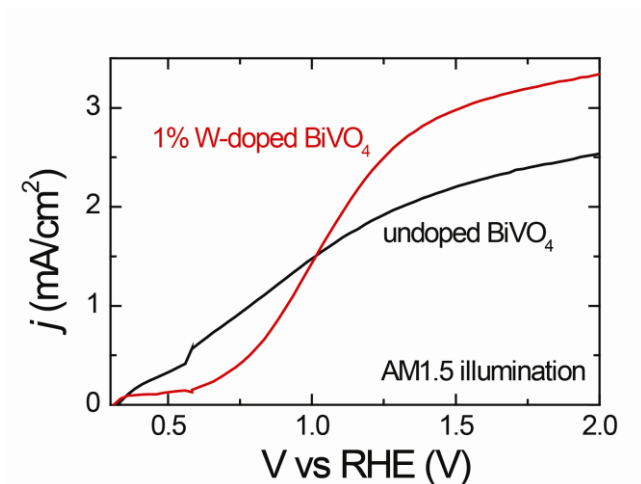


**Figure 4.5.** AM1.5 photocurrent-voltage curve of undoped and 1% W-doped BiVO<sub>4</sub> photoanodes measured under three-electrode configuration in a 0.1 M KPi (pH~7) electrolyte solution at a scan rate of 50 mV/s. Both photoanodes were modified with a 30 nm thick cobalt phosphate water oxidation catalyst.

#### 4.4 Conclusions

In conclusion, our time-resolved microwave conductivity study quantitatively confirms previous reports of poor carrier transport in BiVO<sub>4</sub> photoanodes. Undoped BiVO<sub>4</sub> shows an extrapolated carrier mobility of  $\sim 4 \times 10^{-2} \text{ cm}^2 \text{ V}^{-1} \text{ s}^{-1}$  under  $\sim 1$  sun illumination conditions, which is at least 1-2 orders of magnitude lower than in typical semiconductor photoelectrodes for water splitting. Despite the low mobility, high quantum efficiencies can nevertheless be achieved in BiVO<sub>4</sub> due to the long lifetime of the photogenerated charge carriers ( $\sim 40$  ns), which leads to relatively long carrier diffusion lengths. The long lifetime implies that there are few intrinsic recombination centers, from which we conclude that BiVO<sub>4</sub> is a highly “defect-tolerant” material. Doping with tungsten significantly improves the photocurrent of the material, despite the fact that it decreases the carrier lifetime and mobility with  $\sim 1$  order of magnitude due to (de-)trapping in intermediate-level W donor states. This confirms that bulk electronic conductivity is the main performance bottleneck for BiVO<sub>4</sub>. Finally, these results clearly demonstrate the rich and complex nature of the carrier dynamics in BiVO<sub>4</sub>, and illustrate the need for further studies to complete our understanding of the BiVO<sub>4</sub> photoanode.

## 4.5 References

1. Haije, W. & Geerlings, H. Efficient Production of Solar Fuel Using Existing Large Scale Production Technologies, *Environ. Sci. Technol.* **45**, 8609-8610 (2011).
2. Tokunaga, S., Kato, H., & Kudo, A. Selective preparation of monoclinic and tetragonal BiVO<sub>4</sub> with scheelite structure and their photocatalytic properties, *Chem. Mater.* **13**, 4624-4628 (2001).
3. Abdi, F. F., Firet, N., Dabirian, A., & van de Krol, R. Spray-deposited Co-Pi Catalyzed BiVO<sub>4</sub>: a low-cost route towards highly efficient photoanodes, *MRS Online Proceedings Library* **1446**, (2012).
4. Chatchai, P. et al. FTO/SnO<sub>2</sub>/BiVO<sub>4</sub> composite photoelectrode for water oxidation under visible light irradiation, *Electrochem. Solid State Lett.* **11**, H160-H163 (2008).
5. Chen, S. & Wang, L. W. Thermodynamic Oxidation and Reduction Potentials of Photocatalytic Semiconductors in Aqueous Solution, *Chem. Mater.* **24**, 3659-3666 (2012).
6. Abdi, F. F. & van de Krol, R. Nature and Light Dependence of Bulk Recombination in Co-Pi-Catalyzed BiVO<sub>4</sub> Photoanodes, *J. Phys. Chem. C* **116**, 9398-9404 (2012).
7. Abdi, F. F., Firet, N., & van de Krol, R. Efficient BiVO<sub>4</sub> Thin Film Photoanodes Modified with Cobalt Phosphate Catalyst and W-doping, *ChemCatChem* **5**, 490-496 (2013).
8. Zhong, D. K., Choi, S., & Gamelin, D. R. Near-Complete Suppression of Surface Recombination in Solar Photoelectrolysis by "Co-Pi" Catalyst-Modified W:BiVO<sub>4</sub>, *J. Am. Chem. Soc.* **133**, 18370-18377 (2011).
9. Infelta, P. P., Haas, M. P. D., & Warman, J. M. Study of Transient Conductivity of Pulse Irradiated Dielectric Liquids on A Nanosecond Timescale Using Microwaves, *Radiation Physics and Chemistry* **10**, 353-365 (1977).
10. Savenije, T. J., de Haas, M. P., & Warman, J. M. The yield and mobility of charge carriers in smooth and nanoporous TiO<sub>2</sub> films, *Zeitschrift Fur Physikalische Chemie-International Journal Of Research In Physical Chemistry & Chemical Physics* **212**, 201-206 (1999).
11. Kroeze, J. E., Savenije, T. J., & Warman, J. M. Electrodeless determination of the trap density, decay kinetics, and charge separation efficiency of dye-sensitized nanocrystalline TiO<sub>2</sub>, *J. Am. Chem. Soc.* **126**, 7608-7618 (2004).
12. Carneiro, J. T., Savenije, T. J., & Mul, G. Experimental evidence for electron localization on Au upon photo-activation of Au/anatase catalysts, *Phys. Chem. Chem. Phys.* **11**, 2708-2714 (2009).

13. Savenije, T. J., Huijser, A., Vermeulen, M. J., & Katoh, R. Charge carrier dynamics in TiO<sub>2</sub> nanoparticles at various temperatures, *Chem. Phys. Lett.* **461**, 93-96 (2008).
14. Kunst, M., Wunsch, F., & von Aichberger, S. Recombination at high charge carrier concentrations in a-Si:H films, *Thin Solid Films* **383**, 274-276 (2001).
15. Vanderhaghen, R. et al. Electronic transport in microcrystalline silicon controlled by trapping and intra-grain mobility, *Journal Of Non-Crystalline Solids* **299**, 365-369 (2002).
16. Baumann, A. et al. Influence of Phase Segregation on Recombination Dynamics in Organic Bulk-Heterojunction Solar Cells, *Adv. Funct. Mater.* **21**, 1687-1692 (2011).
17. Moehl, T. et al. Relaxation of Photogenerated Carriers in P3HT:PCBM Organic Blends, *ChemSusChem* **2**, 314-320 (2009).
18. Ferguson, A. J. et al. Photoinduced Energy and Charge Transfer in P3HT:SWNT Composites, *J. Phys. Chem. Lett.* **1**, 2406-2411 (2010).
19. Umeyama, T. et al. Selective Formation and Efficient Photocurrent Generation of [70]Fullerene—Single-Walled Carbon Nanotube Composites, *Adv. Mater.* **22**, 1767-1770 (2010).
20. Savenije, T. J. et al. Spatially resolved photoconductive properties of profiled polycrystalline silicon thin films, *J. Appl. Phys.* **91**, 5671-5676 (2002).
21. The number of incident photons in AM1.5 illumination is  $\sim 4.3 \times 10^{17} \text{ s}^{-1} \text{ cm}^{-2}$ . Multiplying this with the laser pulse of 3.5 ns, there are  $\sim 1.5 \times 10^9$  photons/cm<sup>2</sup>.
22. Berak, J. M. & Sienko, M. J. Effect of oxygen-deficiency on electrical transport properties of tungsten trioxide crystals, *J. Solid State Chem.* **2**, 109-133 (1970).
23. Bosman, A. J. & Vandaal, H. J. Small-Polaron Versus Band Conduction in Some Transition-Metal Oxides, *Advances in Physics* **19**, 1-& (1970).
24. Brus, L. Electron-electron and electron-hole interactions in small semiconductor crystallites: The size dependence of the lowest excited electronic state, *J. Chem. Phys.* **80**, 4403 (1984).
25. Jeong, B. S., Norton, D. P., & Budai, J. D. Conductivity in transparent anatase TiO<sub>2</sub> films epitaxially grown by reactive sputtering deposition, *Solid-State Electronics* **47**, 2275-2278 (2003).
26. Matsuzaki, K. et al. Epitaxial growth of high mobility Cu<sub>2</sub>O thin films and application to p-channel thin film transistor, *Appl. Phys. Lett.* **93** (2008).
27. S. M. Sze, *Physics of Semiconductor Devices*, John Wiley & Sons, New York **1981**.
28. Joly, A. G. et al. Carrier dynamics in alpha-Fe<sub>2</sub>O<sub>3</sub> (0001) thin films and single crystals probed by femtosecond transient absorption and reflectivity, *J. Appl. Phys.* **99** (2006).

29. Cherepy, N. J. et al. Ultrafast studies of photoexcited electron dynamics in gamma- and alpha-Fe<sub>2</sub>O<sub>3</sub> semiconductor nanoparticles, *J. Phys. Chem. B* **102**, 770-776 (1998).
30. Kennedy, J. H. & Frese, K. W., Jr. Photooxidation of water at alpha-Fe<sub>2</sub>O<sub>3</sub> electrodes, *J. Electrochem. Soc.* **125**, 709-714 (1978).
31. Butler, M. A. Photoelectrolysis and physical properties of the semiconducting electrode WO<sub>3</sub>, *J. Appl. Phys.* **48**, 1914-1920 (1977).
32. Paracchino, A. et al. Synthesis and Characterization of High-Photoactivity Electrodeposited Cu<sub>2</sub>O Solar Absorber by Photoelectrochemistry and Ultrafast Spectroscopy, *The Journal of Physical Chemistry C* **116**, 7341-7350 (2012).
33. Berglund, S. P., Rettie, A. J. E., Hoang, S., & Mullins, C. B. Incorporation of Mo and W into nanostructured BiVO<sub>4</sub> films for efficient photoelectrochemical water oxidation, *Phys. Chem. Chem. Phys.* **14**, 7065-7075 (2012).
34. Liang, Y. Q., Tsubota, T., Mooij, L. P. A., & van de Krol, R. Highly Improved Quantum Efficiencies for Thin Film BiVO<sub>4</sub> Photoanodes, *J. Phys. Chem. C* **115**, 17594-17598 (2011).
35. Ye, H., Park, H. S., & Bard, A. J. Screening of Electrocatalysts for Photoelectrochemical Water Oxidation on W-Doped BiVO<sub>4</sub> Photocatalysts by Scanning Electrochemical Microscopy, *J. Phys. Chem. C* **115**, 12464-12470 (2011).
36. Ye, H., Lee, J., Jang, J. S., & Bard, A. J. Rapid Screening of BiVO<sub>4</sub>-Based Photocatalysts by Scanning Electrochemical Microscopy (SECM) and Studies of Their Photoelectrochemical Properties, *J. Phys. Chem. C* **114**, 13322-13328 (2010).
37. Li, M. T., Zhao, L. A., & Guo, L. J. Preparation and photoelectrochemical study of BiVO<sub>4</sub> thin films deposited by ultrasonic spray pyrolysis, *Int. J. Hydrogen Energy* **35**, 7127-7133 (2010).
38. Zhao, Z. Y., Li, Z. S., & Zou, Z. G. Electronic structure and optical properties of monoclinic clinobisvanite BiVO<sub>4</sub>, *Phys. Chem. Chem. Phys.* **13**, 4746-4753 (2011).

## 5 Efficient Solar Water Splitting with a Silicon PV-biased Gradient-doped Oxide Homojunction Photoanode

We describe a simple yet efficient water splitting device based on a compact, non-porous metal oxide photoanode connected to a single- or double-junction amorphous silicon cell in a tandem configuration. Metal oxides are generally very stable in aqueous solutions and cheap, but their photochemical performance is usually limited by poor charge carrier separation. We show that this problem can be solved by introducing a gradient dopant concentration in the metal oxide film, thereby creating a distributed  $n^+ - n$  homojunction. This concept is demonstrated with a low-cost, spray-deposited W-doped  $\text{BiVO}_4$  photoanode in which carrier separation efficiencies of up to 80% are achieved. By combining this state-of-the-art photoanode with an earth-abundant cobalt phosphate water oxidation catalyst and a double- or single-junction amorphous Si solar cell, stable short-circuit water splitting photocurrents of  $\sim 4 \text{ mA/cm}^2$  and  $3 \text{ mA/cm}^2$ , respectively, are achieved under 1 sun illumination. The  $4 \text{ mA/cm}^2$  photocurrent corresponds to a solar-to-hydrogen (STH) efficiency of 4.9%, which is the highest efficiency yet reported for a stand-alone water splitting device based on a metal oxide photoanode.

---

This chapter has been published: F. F. Abdi, L. Han, A. H. M. Smets, M. Zeman, B. Dam and R. van de Krol, *Nat. Commun.* 4:2195 (2013)

## 5.1 Introduction

The development of solar water splitting devices has been the focus of many researchers recently, since the realization of such devices provides an attractive route to convert sunlight into a chemical fuel in the form of hydrogen. Various tandem device configurations have been proposed, but the optimal design is still not clear.<sup>1-6</sup> One approach is to combine a solar cell with hydrogen and oxygen evolution catalysts. Devices with a solar-to-hydrogen (STH) efficiency of up to 2.5%, consisting of triple-junction amorphous silicon (3-jn a-Si) solar cells with hydrogen and oxygen evolution catalysts, were demonstrated as early as 20 years ago.<sup>5,6</sup> Based on the same concept, along with a breakthrough in the development of cobalt-based water oxidation catalysts that work in near-neutral pH conditions,<sup>7</sup> Nocera and coworkers demonstrated an improved STH efficiency of up to 4.7%.<sup>8</sup> In all these cases, however, a photovoltaic (PV) cell with a rather high open circuit potential ( $>1.6$  V) is needed in order to provide the thermodynamic potential for water splitting (1.23 V) plus the necessary overpotentials.<sup>9</sup> Since the catalytic efficiency of the cobalt-based water oxidation catalyst is already close to one,<sup>10</sup> any major efficiency improvements for this approach would require PV devices with higher operating voltages and currents. Considering that triple-junction a-Si solar cells are already quite complex, the feasibility of such a strategy is doubtful.

Alternatively, one may replace one or two of the p-i-n junctions in a 3-jn a-Si solar cell with a single semiconducting metal oxide film. Metal oxides are generally stable in water and form a junction at the semiconductor/water interface, providing an elegant, simple, and low-cost alternative to the p-i-n junction. Moreover, the larger bandgap of the metal oxide allows better use of the solar spectrum and can lead to higher efficiencies than a pure Si-based device. Miller et al. have argued that such a 'hybrid photoelectrode' has the potential of achieving 16% STH efficiency. By combining a 2-jn a-Si solar cell and a tungsten trioxide ( $\text{WO}_3$ ) photoanode, they predicted a 2.2% STH efficiency and demonstrated a practical efficiency of 0.6%.<sup>4</sup> Later, they improved the performance and demonstrated an efficiency of 3%.<sup>11</sup> In a similar concept, Brillet et al. recently showed a 3.1% efficient system by combining a  $\text{WO}_3$  photoanode and a dye-sensitized solar cell.<sup>12</sup> The rather modest efficiency of these efforts is a result of the low conduction band energy and the large bandgap of the  $\text{WO}_3$  photoanode. In order to achieve the 10% STH efficiency target, a metal oxide with a maximum bandgap of 2.3-2.4 eV is required.

Here, we demonstrate a solar water splitting device based on the combination of a W-doped  $\text{BiVO}_4$  photoanode and a double-junction amorphous silicon (2-jn a-Si) solar cell. By introducing a gradient in the dopant profile it is possible to create a distributed

$n^+ - n$  homojunction in  $\text{BiVO}_4$  which greatly enhances the charge separation efficiency, thereby effectively removing its main performance bottleneck. In combination with an efficient earth-abundant water oxidation catalyst and an amorphous silicon solar cell connected in tandem, this provides a new and highly effective strategy for developing efficient solar water splitting devices.

## 5.2 Experimental details

### Synthesis

Dense thin films of  $\text{BiVO}_4$  were prepared using spray pyrolysis. The preparation of the precursor solution and the spray pyrolysis setup are described elsewhere.<sup>10, 13</sup> The spray deposition rate is  $\sim 1$  nm per cycle. The 1% W-doped  $\text{BiVO}_4$  sample was prepared by spraying 200 cycles of the  $\text{BiVO}_4$  precursor solution containing 1 at% of W. The W: $\text{BiVO}_4$  homojunction was prepared by spraying 100 cycles of the  $\text{BiVO}_4$  precursor solution containing 1 at% of W, followed by 100 cycles of the  $\text{BiVO}_4$  reverse homojunction. This sequence was reversed for the deposition of the W: $\text{BiVO}_4$  reverse homojunction. To deposit the gradient-doped W: $\text{BiVO}_4$ , the concentration of W in the  $\text{BiVO}_4$  precursor solution was changed in step every 20 cycles, starting from 1 at% to 0 at%. Prior to every deposition,  $\sim 80$  nm of  $\text{SnO}_2$  layer was deposited onto FTO substrate to prevent recombination of electrons and holes at the FTO/ $\text{BiVO}_4$  interface.<sup>14</sup> The substrates used are either TEC-15 (15  $\Omega/\text{sq}$ , Hartford Glass Co.) or Asahi UV (8  $\Omega/\text{sq}$ , Asahi Glass Co.) FTO-coated glass. After the deposition, all samples were annealed for 2 hours at 450 °C in air to further improve the crystallinity. 30 nm Co-Pi catalyst was electro-deposited according to the recipe from Kanan and Nocera.<sup>7</sup> The electro-deposition was performed at a constant voltage of 1.7 V vs RHE for 15 min. Care was taken to always keep the electrodeposited Co-Pi layer wet, as intermediate drying of the Co-Pi was found to adversely affect the stability.

The 2-jn a-Si and 1-jn a-Si solar cells were deposited on Asahi UV substrates. For the 2-jn a-Si, boron doped hydrogenated amorphous silicon carbide (a-SiC:H(B)), intrinsic a-SiC:H and hydrogenated amorphous silicon (a-Si:H) are used as p-layers, buffer-layers and i-layers, respectively. The n-layer of the top cell is a single layer of phosphorus-doped microcrystalline silicon oxide ( $\mu\text{c-SiO}_x\text{:H(P)}$ ) whereas the n-layer of the bottom cell is a double layer of  $\mu\text{c-SiO}_x\text{:H(P)}$  and phosphorus-doped hydrogenated amorphous silicon (a-Si:H(P)). For the 1-jn a-Si solar cell, boron doped hydrogenated amorphous silicon carbide (a-SiC:H(B)) is used as the p-layer, while the i-layer and n-layer are intrinsic hydrogenated amorphous silicon (a-Si:H) and phosphorus-doped hydrogenated amorphous silicon (a-Si:H(P)), respectively. These various silicon alloys were deposited using the radio frequency plasma enhanced

chemical vapor deposition (RF-PECVD) technique in a multi-chamber tool. After the deposition of the silicon thin films, the front contact (300 nm Al) and the back contact (100 nm Ag, 30 nm Cr, 400 nm Al) were deposited by a rotating Provac evaporator. The metal back contacts have a diameter of 7 mm and a size of 1×1 cm for the 2-jn a-Si and 1-jn a-Si, respectively.

The gradient-doped BiVO<sub>4</sub> photoanode and the amorphous silicon solar cell were then assembled to fabricate an integrated “hybrid photoelectrode” device (as shown in Fig. 5.5 and Fig. C9 of Appendix C) using an ultra-clear two-component epoxy adhesive (Loctite Hysol 3430), pasted on the glass side of each devices.

### Photoelectrochemical characterization

Photoelectrochemical characterization was carried out in an aqueous 0.1 M potassium phosphate electrolyte solution (KPi, pH~7.3). The potential of the working electrode was controlled by a potentiostat (EG&G PAR 283). In three electrode measurements, a coiled Pt wire and an Ag/AgCl electrode (XR300, saturated KCl and AgCl solution, Radiometer Analytical) were used as the counter and reference electrodes, respectively. Two-electrode measurements were conducted by connecting the working electrode lead of the potentiostat to the BiVO<sub>4</sub> photoanode and the reference and counter electrode leads of the potentiostat to the coiled Pt wire. Cyclic voltammetry measurements were performed with a scan rate of 50 mV/s. White light photocurrent measurements were performed under simulated AM1.5 solar illumination (100 mW/cm<sup>2</sup>) with a Newport Sol3A Class AAA solar simulator (type 94023A-SR3). Electrical contact to the sample was made using a silver wire and a graphite paste. A Keithley 2001 multimeter was used as the ammeter in the current vs time measurement of the tandem device.

### Physical characterization

Structural analysis was performed with a Bruker D8 Advance X-ray diffractometer (Co-K<sub>α</sub>, λ = 0.178897 nm) equipped with a LynxEye detector in the Bragg-Brentano configuration. Scanning electron micrographs were taken with JEOL JSM 6500F Scanning Electron Microscope at an accelerating voltage of 15 kV. The UV-vis absorption was measured with a Perkin Elmer Lambda 900 spectrometer.



### 5.3 Results and discussion

#### Gradient-doped W:BiVO<sub>4</sub> homojunction

In the monoclinic phase, BiVO<sub>4</sub> is an n-type photoactive semiconductor with a bandgap of 2.4 eV,<sup>15-17</sup> with a conduction band positioned close to the hydrogen evolution potential.<sup>18</sup> In the last two years, the photoelectrochemical performance of BiVO<sub>4</sub> has been significantly improved.<sup>13, 19-22</sup> This has been largely due to the development of novel water oxidation catalysts based on e.g. cobalt- and iron oxyhydroxide-based materials.<sup>7, 19</sup> As a result, the best-performing BiVO<sub>4</sub> photoanodes are no longer limited by slow water oxidation kinetics, but by poor carrier separation due to slow electron transport in BiVO<sub>4</sub>.<sup>13</sup> Although the introduction of a donor type dopant, such as W or Mo,<sup>20-23</sup> can increase the conductivity of BiVO<sub>4</sub>, this is by itself not sufficient because of the low intrinsic mobility of BiVO<sub>4</sub>.<sup>24</sup> Since one cannot easily modify the intrinsic mobility, a different strategy is needed to improve the carrier separation.

To achieve good carrier separation in a semiconductor photoanode, the presence of a built-in electric field (band bending) is required. One of the most common ways to enhance band bending in a photoanode is by combining it with another semiconductor, creating a heterojunction.<sup>18, 24, 25</sup> It is, however, not always trivial to find materials with suitably aligned energy levels, and a clean heterostructure can be difficult to synthesize. Improper growth conditions may lead to the presence of large amounts of defects at the interface that might act as carrier traps and recombination centers.<sup>26, 27</sup> Moreover, the high carrier concentration in doped BiVO<sub>4</sub>—which is needed to address its low intrinsic mobility—reduces the extent of the space charge region to just a few nm.

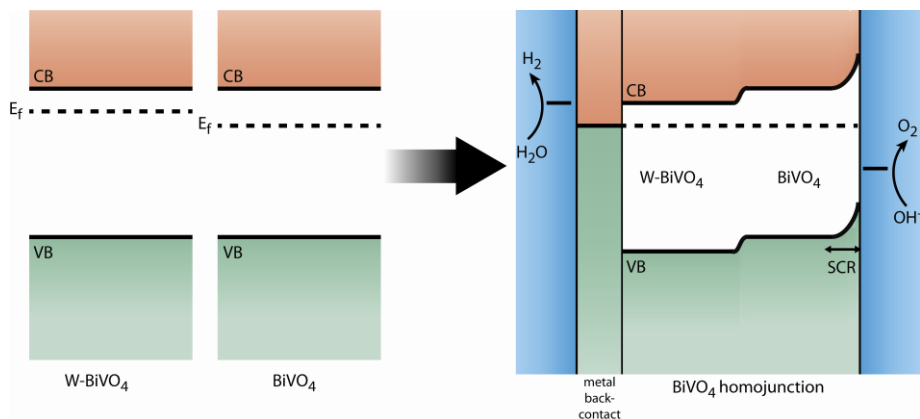


**Figure 5.1.** Energy band schematic of W-doped BiVO<sub>4</sub> and BiVO<sub>4</sub> (left), showing the valence band (VB), conduction band (CB), and the Fermi level energy (E<sub>F</sub>). When they are brought into contact, the Fermi level energy will equilibrate and additional band bending is introduced, on top of the existing one at the space charge region (SCR), forming a BiVO<sub>4</sub> homojunction (right).

To avoid these complications, we introduce a step in the dopant concentration to generate additional band bending in the bulk of the sample, and thereby improve the carrier separation. The principle is illustrated in Fig. 5.1. Undoped BiVO<sub>4</sub> is an n-type semiconductor, and donor-doping it with tungsten (W) raises its Fermi level. When W-doped and undoped BiVO<sub>4</sub> are brought into contact, the Fermi energy levels equilibrate by electron transfer from the W-doped part to the undoped part of the material. A modest depletion layer at the interface between W-doped and undoped BiVO<sub>4</sub> is then formed that enhances charge separation. In contrast to a heterojunction, the synthesis of a homojunction is usually trivial, and the extent of the band bending can be tailored by simply varying the dopant concentration.

The use of a homojunction to enhance carrier separation is a well established concept in semiconductor physics. Both p-n homojunctions and homojunctions in which a gradient in the composition causes a corresponding gradient in the band gap (e.g. In<sub>x</sub>Ga<sub>1-x</sub>N, CdS<sub>1-x</sub>Se<sub>x</sub>, Ga<sub>1-x</sub>Al<sub>x</sub>As) are well known methods to enhance bulk carrier separation. The physical principles are, however, somewhat different than the one we employ here. Our approach resembles the Back Surface Field (BSF) method,<sup>28</sup> which is usually implemented as a  $p^+-p$  junction near the back contact of a Si or GaAs solar cell that reflects the minority carriers and minimizes recombination at the interface. The main difference is that our distributed  $n^+-n$  homojunction enhances charge separation throughout the bulk of the material, not just at the interface. To the best of our knowledge, this concept has not yet been reported before. This is perhaps not as surprising as it seems, since this approach only makes sense for very highly

doped semiconductors, a class of materials that is not typically used as a light absorber.

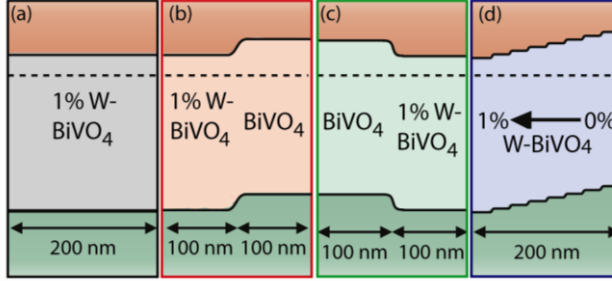


**Figure 5.2.** (a) 1% W-doped BiVO<sub>4</sub>, (b) W:BiVO<sub>4</sub> homojunction, (c) W:BiVO<sub>4</sub> reverse homojunction, and (d) gradient-doped W:BiVO<sub>4</sub>. In all cases, the light enters from the right-hand side (through the electrolyte) and the FTO back-contact is situated on the left. The space charge region at the semiconductor/electrolyte interface is not depicted for clarity.

To demonstrate this concept, ~200 nm thick BiVO<sub>4</sub> photoanode samples with different dopant profiles were synthesized by spray pyrolysis. We first compare a 1% W-doped BiVO<sub>4</sub> sample (Fig. 5.2a) with a homojunction of 1% W-doped / undoped BiVO<sub>4</sub> (Fig. 5.2b). Due to the additional band bending in the W:BiVO<sub>4</sub> homojunction, we expect an enhanced carrier separation. In order to quantify the carrier separation efficiency, we use an elegant formulation first reported by Dotan et al.<sup>29</sup>:

$$J_{ph} = J_{abs} \times \eta_{sep} \times \eta_{cat} \quad (5.1)$$

where  $J_{ph}$  is the total photocurrent density,  $J_{abs}$  is the photon absorption rate expressed as current density,  $\eta_{sep}$  is the carrier separation efficiency, and  $\eta_{cat}$  is the catalytic efficiency for water oxidation. The differences between the internal/external quantum efficiencies and the carrier separation efficiency are explained in Appendix C. When a highly effective hole scavenger such as hydrogen peroxide (H<sub>2</sub>O<sub>2</sub>) is added into the electrolyte, the catalytic efficiency can be assumed to be ~100% ( $\eta_{cat} = 1$ ).<sup>29-31</sup> This allows one to directly calculate the separation and oxidation efficiencies from the measured photocurrents with and without hydrogen peroxide:  $\eta_{sep} = J_{H_2O_2} / J_{abs}$  and  $\eta_{cat} = J_{H_2O} / J_{H_2O_2}$ .<sup>29</sup> As expected, the carrier separation efficiency of the W:BiVO<sub>4</sub> homojunction is higher than that of the W:BiVO<sub>4</sub> reference sample (Fig. 5.3), indicating that the dopant concentration difference can indeed be used to create additional band bending and thus improve carrier separation.

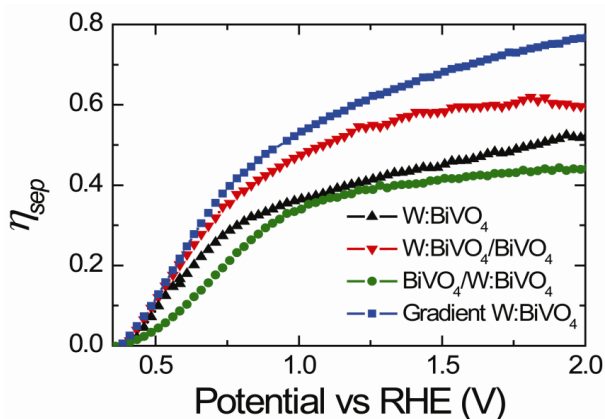


**Figure 5.3.** Carrier separation efficiency ( $\eta_{sep}$ ) as a function of applied potential for 1% W-doped BiVO<sub>4</sub> (▲), W:BiVO<sub>4</sub>/BiVO<sub>4</sub> homojunction (▼), BiVO<sub>4</sub>/W:BiVO<sub>4</sub> reverse homojunction (●), and gradient-doped W:BiVO<sub>4</sub> (■).

To confirm the presence of the homojunction, we also prepared a reverse homojunction in which the W-doped side is now closest to the electrolyte (Fig. 5.2c). In this case, the band bending is present in the opposite direction and should act as a barrier for carrier separation. As shown in Fig. 5.3, the carrier separation efficiency indeed decreases and is even lower than that of the homogeneously-doped reference sample. The decrease is, however, not as big as one might have expected; the reason is that this barrier is actually small enough for a few electrons to overcome thermally (see Appendix C). Nevertheless, this observation provides compelling support for our claim that the improvement in carrier separation efficiency is caused by the additional band bending at the W:BiVO<sub>4</sub>/BiVO<sub>4</sub> homojunction interface.

To fully leverage this effect, we synthesized a BiVO<sub>4</sub> photoanode with a 10-step gradient in W-doping, starting from 1% W at the interface with the back contact to 0% W at the semiconductor/electrolyte interface (Fig. 5.2d). This extends the presence of band bending over the entire thickness of the photoanode. As a result, we find that the carrier separation efficiency increases to ~60% at 1.23 V vs RHE (Fig. 5.3, blue curve), compared to ~38% for homogeneously doped BiVO<sub>4</sub>. This 1.6× improvement shows that a gradient in dopant concentration can be used as a simple, yet highly effective method to enhance the carrier separation in highly-doped semiconductor photoelectrodes.

To further correlate the improvement in carrier separation efficiency to the presence of band bending, we measure the change in open circuit potential ( $\Delta\text{OCP}$ ) upon AM1.5 illumination. At this illumination intensity, the number of carriers is sufficiently high to cause the bands to flatten (Fig. C1, Appendix C). The difference

between the open circuit potentials with and without illumination thus represents the maximum amount of band bending in the photoanode. The  $\Delta\text{OCP}$  value systematically increases when going from the reference sample  $\rightarrow$  W:BiVO<sub>4</sub> homojunction sample  $\rightarrow$  gradient-doped W:BiVO<sub>4</sub> sample (Fig. C2, Appendix C). This observation thus confirms the presence of additional band bending in the homojunction and the gradient-doped samples.

One would expect that the W:BiVO<sub>4</sub> homojunction sample and the gradient-doped W:BiVO<sub>4</sub> sample will have the same amount of band bending and thus a similar  $\Delta\text{OCP}$  value, since the difference in dopant concentration is the same (Fig. 5.2b and 5.2d, both from 0%  $\rightarrow$  1%). However, the fact that the gradient-doped W:BiVO<sub>4</sub> sample shows a higher  $\Delta\text{OCP}$  clearly indicates that there is less recombination in this sample. This is consistent with the larger number of space charge regions, one for each step in the concentration (Fig. 5.2d). We also observe in Fig. C2 that the  $\Delta\text{OCP}$  for the W:BiVO<sub>4</sub> reverse homojunction sample reaches the same value as that of the reference sample. This is as expected, since in both cases the maximum amount of band bending is determined by the space charge region in the 1% W-doped BiVO<sub>4</sub> next to the semiconductor/electrolyte interface. Finally, we note that the appearance, optical absorption, morphology, and crystal structure of all samples are the same, i.e., these properties are not affected by the tungsten dopant (Figs. C3-6, Appendix C).

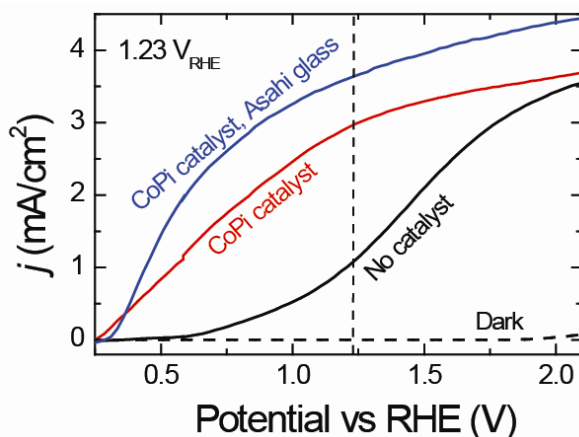


**Figure 5.4.** Three-electrode AM1.5 photocurrent vs voltage (J-V) curve of uncatalyzed gradient-doped W:BiVO<sub>4</sub> on TEC-15 (black), Co-Pi-catalyzed gradient-doped W:BiVO<sub>4</sub> on TEC-15 (red) and on Asahi conducting glass (blue). The dark current is shown as a dashed black curve. The electrolyte used is 0.1 M potassium phosphate (KPi) buffer at pH  $\sim$ 7.3.

Under AM1.5 illumination, the gradient-doped W:BiVO<sub>4</sub> shows a photocurrent of ~1.1 mA/cm<sup>2</sup> at 1.23 V vs RHE (Fig. 5.4, solid black curve). To improve the oxygen evolution kinetics, we electro-deposited a 30 nm thick cobalt phosphate (Co-Pi) catalyst layer. Based on our previous study,<sup>13</sup> this thickness gives an optimum catalytic improvement for BiVO<sub>4</sub> and ensures that more than 90% of the incident light reaches the BiVO<sub>4</sub>. This results in a ~3-fold improvement of the AM1.5 photocurrent, up to 3 mA/cm<sup>2</sup> at 1.23 V vs RHE (Fig. 5.4, red curve). To improve the performance even further, we replace the standard TEC-15 substrate with a textured Asahi UV conducting glass substrate. As a result of higher absorption and effective surface area (Fig. C7, Appendix C), this further improves the AM1.5 photocurrent to ~3.6 mA/cm<sup>2</sup> at 1.23 V vs RHE (Fig. 5.4, blue curve). This is the highest photocurrent ever reported for BiVO<sub>4</sub>, and represents a ~1.6× improvement compared to the best Co-Pi catalyzed W:BiVO<sub>4</sub> photoanode reported previously.<sup>10</sup> It also exceeds the highest AM1.5 photocurrents reported at this potential for α-Fe<sub>2</sub>O<sub>3</sub><sup>32</sup> and WO<sub>3</sub><sup>33</sup> (both ~3 mA/cm<sup>2</sup>) by a considerable margin, which firmly establishes BiVO<sub>4</sub> as the new leading performer amongst oxide photoanodes.

### Hybrid photoelectrode

To fabricate a complete device for solar water splitting that does not depend on an externally applied bias potential, we combined the state-of-the-art CoPi-W:BiVO<sub>4</sub> photoanode with a 2-jn a-Si superstrate photovoltaic cell placed behind the PEC cell, as shown in Fig. 5.5. Details of the photovoltaic cell and a photograph of the hybrid device are shown in Figs. C8 and C9 of Appendix C, respectively. In this tandem configuration, photons with energies less than the bandgap of the BiVO<sub>4</sub> are absorbed by the a-Si/a-Si PV structure (Fig. C11, Appendix C). Figure 5.6a shows the J-V curve of the 2-jn a-Si solar cell (black curve) which has been optimized—by tuning the thickness of the individual absorber layers—to match the two-electrode J-V curve of the state-of-the-art BiVO<sub>4</sub> photoanode (blue curve). It should be noted that the J-V curve of the BiVO<sub>4</sub> photoanode in the two-electrode measurement of Fig. 5.6a shows slightly larger photocurrents than the curve in the three-electrode measurement of Fig. 5.4; the reason for this is explained in the Appendix C. Based on the intersection of the two curves in Fig. 5.6a, an operating photocurrent of ~4 mA/cm<sup>2</sup> is predicted for the integrated device.

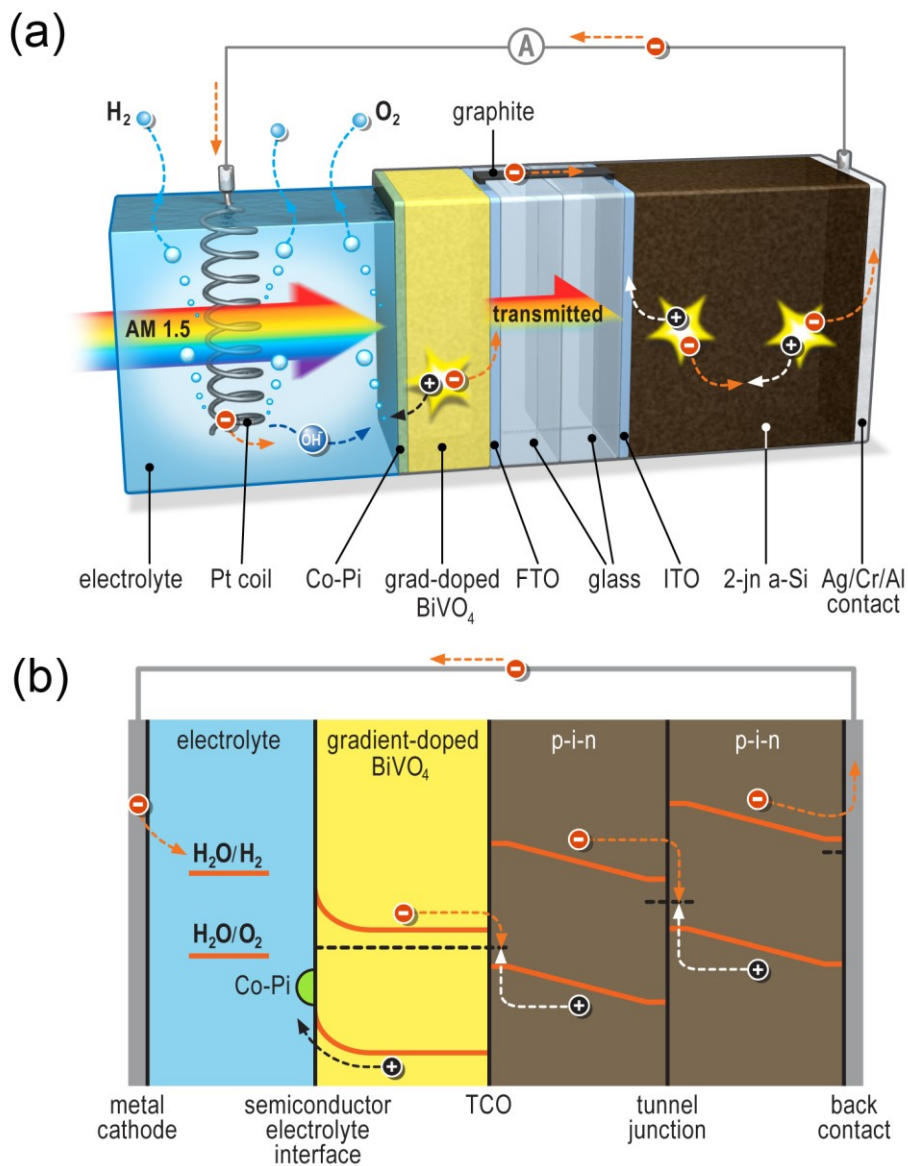


**Figure 5.5.** (a) Schematic diagram of the combined device of gradient-doped W: $\text{BiVO}_4$  and a-Si solar cell. (b) The corresponding band diagram of the hybrid photoelectrode device.

Figure 5.6b shows the AM1.5 photocurrent of the tandem PEC/PV device as a function of time. A stable photocurrent of  $\sim 4$  mA/cm<sup>2</sup> is achieved, which indeed corresponds to the working point of the J-V curve of Fig. 5.6a. Since the Faradaic efficiency of this system is 100%,<sup>21</sup> this corresponds to a STH conversion efficiency of  $\sim 4.9\%$ , which is a 60% improvement compared to a similar device based on 2-jn a-Si / WO<sub>3</sub> reported by Miller et al.<sup>4,11</sup> This efficiency is also superior to the 4.7% efficiency benchmark recently reported by Nocera et al.<sup>8</sup>, who were the first to report on the remarkable efficiency of the CoPi catalyst under pH-neutral conditions.<sup>7</sup> While the water oxidation catalyst that we use is the same, the double-junction a-Si cell we use is much easier to fabricate than the triple-junction device reported in ref [8].

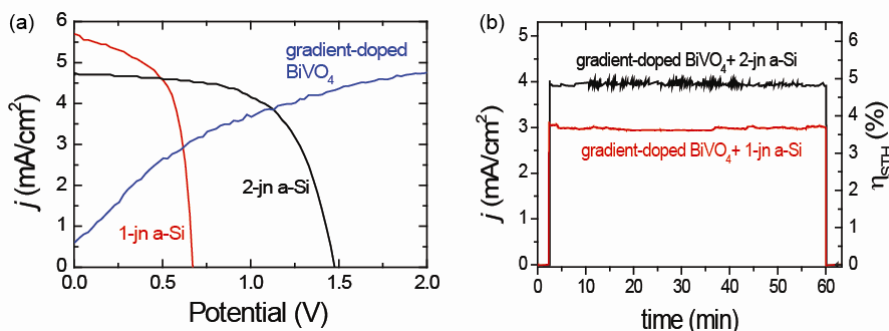


**Figure 5.6.** (a) Two-electrode AM1.5 J-V curve of Co-Pi-catalyzed gradient-doped BiVO<sub>4</sub> on Asahi TCO glass (gradient-doped BiVO<sub>4</sub>, blue curve). Also shown are the J-V curves of double-junction a-Si (black) and single-junction a-Si (red) solar cells placed behind the CoPi-BiVO<sub>4</sub>:W photoanode. The intersection of the BiVO<sub>4</sub> curve with either one of the a-Si curves indicates the operating point of the combined water splitting device. (b) Current vs. time for the CoPi-BiVO<sub>4</sub>:W/2-jn a-Si device and the CoPi-BiVO<sub>4</sub>:W/1-jn a-Si device in the hybrid photoelectrode configuration under AM1.5 illumination. The electrolyte used is 0.1 M potassium phosphate (KPi) buffer at pH  $\sim 7.3$ .

To illustrate that the gradient-doped W:BiVO<sub>4</sub> generates part of the total photovoltage, the same AM1.5 photocurrent measurement was done with the 2-jn a-Si cell connected to a Co-Pi film deposited directly on FTO (i.e., without the BiVO<sub>4</sub>). This results in a much lower photocurrent of  $\sim 1.5$  mA/cm<sup>2</sup> (Fig. C12, Appendix C), despite the fact that the Co-Pi/FTO electrode transmits a much larger part of the solar spectrum to the underlying 2-jn a-Si cell. This confirms that BiVO<sub>4</sub> provides additional electromotive driving force, and that the CoPi-W:BiVO<sub>4</sub> / 2-jn a-Si device is effectively a triple-junction system.



An important advantage of using  $\text{BiVO}_4$  instead of other metal oxides in the hybrid photoelectrode configuration is its higher conduction band energy. This translates into a modest photocurrent onset potential of +0.25 V vs RHE for  $\text{BiVO}_4$  (Fig. 5.4). For comparison, the photocurrent onset potentials for  $\text{Fe}_2\text{O}_3$  and  $\text{WO}_3$  are +0.8 V vs RHE and +0.5 V vs RHE, respectively.<sup>33, 34</sup> A lower onset potential directly relaxes the demand on the voltage provided by the PV cell, and allows simpler and cheaper designs to be pursued. In fact, based on the intersection of the J-V curves, Fig. 5.6a suggests that photocurrent of 3  $\text{mA}/\text{cm}^2$  can be achieved by combining the gradient-doped  $\text{BiVO}_4$  with a single-junction a-Si solar cell (Fig. C8, Appendix C). This photocurrent is indeed obtained for an actual hybrid 1-jn a-Si / CoPi-W: $\text{BiVO}_4$  device, as shown by the red curve in Fig. 5.6b. This relatively simple device shows a 3.6% STH efficiency with no sign of degradation within the 1-hour measurement period.

Another advantage of  $\text{BiVO}_4$  is that high photocurrents can be obtained for compact, thin film electrodes. In contrast, many other metal oxide photoelectrodes require highly optimized nanostructures to ensure that the minority carriers can reach the surface before they recombine, or to avoid limitations due to slow surface reaction kinetics. Apart from the fact that they are easier to make, compact films also avoid potential mass transport problems that may arise due to gas bubble formation within mesoporous structures. Another advantage of non-porous electrodes is the limited amount of light scattering, which may prevent the low-energy photons from reaching the bottom cell. This was found to be a problem for tandem water splitting devices based on nanostructured  $\alpha\text{-Fe}_2\text{O}_3$  electrodes and dye sensitized solar cells (DSSCs). These devices showed efficiencies of 1.36%, significantly below the predicted value of 3.3%.<sup>35</sup> Recently, the EPFL group solved these problems and reported STH efficiencies of 1.17 and 3.1% for stand-alone water splitting devices based on nanostructured  $\text{Fe}_2\text{O}_3/\text{DSSC}$  and  $\text{WO}_3/\text{DSSC}$  devices, respectively.<sup>12</sup>

The shapes of the J-V curves of the a-Si /  $\text{BiVO}_4$  devices shown in Fig. 5.6a indicate that little or no further improvement can be gained from improving the currents delivered by the silicon PV devices. Instead, future efforts should initially focus on improving the light absorption and carrier separation efficiency in  $\text{BiVO}_4$ . The current films absorb 75% of the incident AM1.5 light with  $h\nu > E_g$ , while the carrier separation efficiency is still below 60% at the working point of the device—despite the large improvement by the gradient doping profile. Based on the near-unity internal quantum efficiencies that can be achieved in this defect-tolerant material,<sup>10</sup> addressing these remaining issues may lead to AM1.5 photocurrents that are close to the theoretical value of 7.5  $\text{mA}/\text{cm}^2$ .

Further development of these efficient hybrid photoelectrodes into practical solar water splitting modules requires several engineering challenges to be solved. While the near-neutral pH of the electrolyte solution ensures that the  $\text{BiVO}_4$  is photochemically stable,<sup>36</sup> proton transport is markedly slower than in strongly alkaline or acidic electrolytes. The consequences of such mass transport limitations are clearly

illustrated by the results of Nocera et al.<sup>8</sup>, who showed that their solar-to-H<sub>2</sub> efficiency dropped from 4.7% to 2.5% when changing the cell configuration from two electrodes that face each other, to a configuration in which H<sub>2</sub> and O<sub>2</sub> evolve from opposite sides of an ‘artificial leaf’. The design of new device architectures that efficiently manage proton transport and avoid local pH changes in near-neutral solutions thus represents an important challenge for future photoelectrochemical energy conversion studies. Once the optimal device configuration is chosen, the evolved gasses need to be transported away efficiently without the risk of mixing. Finally, the platinum counter electrode that we used here for convenience needs to be replaced by an earth-abundant alternative. Such alternatives, for example in the form of NiMo(Zn),<sup>8</sup> CoMo, or NiFeMo alloys,<sup>37</sup> are already available and show high activities at modest overpotentials.

## 5.4 Conclusions

In summary, we have shown that the poor carrier separation efficiency in BiVO<sub>4</sub> photoanode can be overcome by implementing a multi-step gradient in the tungsten dopant concentration, resulting in the formation of a series of homojunctions in the bulk of the material. A 10-step gradient-doped Co-Pi-catalyzed W:BiVO<sub>4</sub> photoanode generates an AM1.5 photocurrent of 3.6 mA/cm<sup>2</sup> at 1.23 V vs RHE, representing a ~60% improvement over the same electrode with a homogeneous W dopant concentration.<sup>10</sup> Combining this electrode with a 2-jn a-Si solar cell results in a water splitting device with a ~4.9% STH efficiency. This represents a significant improvement over other oxide-based tandem devices that have been reported recently,<sup>11, 12</sup> and sets a new performance benchmark for hybrid photoelectrodes for water splitting. It also exceeds the efficiency of more complicated silicon-based PEC devices based on three p-i-n junctions.<sup>8</sup> Replacing one p-i-n stack (and the accompanying tunnel junction) with a single wide-bandgap metal oxide absorber both simplifies the design and increases the efficiency that can be achieved. Further improvements require a better utilization of the solar spectrum by BiVO<sub>4</sub>, especially for wavelengths close to the band edge, and plasmonic- and/or resonance-enhanced optical absorption<sup>38, 39</sup> seem promising routes to achieve this. Finally, the distributed  $n^+ - n$  homojunction concept represents a generally applicable strategy for improving carrier separation in any high-donor density photoelectrode material. Combined with the hybrid photoelectrode concept, this offers new pathways toward low-cost, efficient devices for solar hydrogen generation.

## 5.5 References

1. Khaselev, O. & Turner, J. A. A monolithic photovoltaic-photoelectrochemical device for hydrogen production via water splitting, *Science* **280**, 425-427 (1998).
2. Grätzel, M. Photoelectrochemical cells, *Nature* **414**, 338-344 (2001).
3. Licht, S. et al. Efficient solar water splitting, exemplified by RuO<sub>2</sub>-catalyzed AlGaAs/Si photoelectrolysis, *J. Phys. Chem. B* **104**, 8920-8924 (2000).
4. Miller, E. L., Marsen, B., Paluselli, D., & Rocheleau, R. Optimization of hybrid photoelectrodes for solar water-splitting, *Electrochem. Solid State Lett.* **8**, A247-A249 (2005).
5. Yamada, Y. et al. One chip photovoltaic water electrolysis device, *Int. J. Hydrogen Energy* **28**, 1167-1169 (2003).
6. Delahoy, A. E. et al. A one-unit photovoltaic electrolysis system based on a triple stack of amorphous silicon (pin) cells, *Int. J. Hydrogen Energy* **10**, 113-116 (1985).
7. Kanan, M. W. & Nocera, D. G. In situ formation of an oxygen-evolving catalyst in neutral water containing phosphate and Co<sup>2+</sup>, *Science* **321**, 1072-1075 (2008).
8. Reece, S. Y. et al. Wireless Solar Water Splitting Using Silicon-Based Semiconductors and Earth-Abundant Catalysts, *Science* **334**, 645-648 (2011).
9. Koper, M. T. Thermodynamic theory of multi-electron transfer reactions: Implications for electrocatalysis, *J. Electroanal. Chem.* **660**, 254-260 (2011).
10. Abdi, F. F., Firet, N., & van de Krol, R. Efficient BiVO<sub>4</sub> Thin Film Photoanodes Modified with Cobalt Phosphate Catalyst and W-doping, *ChemCatChem* **5**, 490-496 (2013).
11. N. Gaillard, Y. Chang, J. Kaneshiro, A. Deangelis, E. L. Miller, Status of Research on Tungsten Oxide-based Photoelectrochemical Devices at the University of Hawai'i, *Proc. SPIE* **7770**, 7770V-1-14 (2010).
12. Brillet, J. et al. Highly efficient water splitting by a dual-absorber tandem cell, *Nat Photon* **6**, 824-828 (2012).
13. Abdi, F. F. & van de Krol, R. Nature and Light Dependence of Bulk Recombination in Co-Pi-Catalyzed BiVO<sub>4</sub> Photoanodes, *J. Phys. Chem. C* **116**, 9398-9404 (2012).
14. Liang, Y. Q., Tsubota, T., Mooij, L. P. A., & van de Krol, R. Highly Improved Quantum Efficiencies for Thin Film BiVO<sub>4</sub> Photoanodes, *J. Phys. Chem. C* **115**, 17594-17598 (2011).
15. Kudo, A., Omori, K., & Kato, H. A novel aqueous process for preparation of crystal form-controlled and highly crystalline BiVO<sub>4</sub> powder from layered vanadates at room temperature and its photocatalytic and photophysical properties, *J. Am. Chem. Soc.* **121**, 11459-11467 (1999).

16. Kudo, A., Ueda, K., Kato, H., & Mikami, I. Photocatalytic O<sub>2</sub> evolution under visible light irradiation on BiVO<sub>4</sub> in aqueous AgNO<sub>3</sub> solution, *Catal. Lett.* **53**, 229-230 (1998).
17. Tokunaga, S., Kato, H., & Kudo, A. Selective preparation of monoclinic and tetragonal BiVO<sub>4</sub> with scheelite structure and their photocatalytic properties, *Chem. Mater.* **13**, 4624-4628 (2001).
18. Hong, S. J., Lee, S., Jang, J. S., & Lee, J. S. Heterojunction BiVO<sub>4</sub>/WO<sub>3</sub> electrodes for enhanced photoactivity of water oxidation, *Energy Environ. Sci.* **4**, 1781-1787 (2011).
19. Seabold, J. A. & Choi, K. S. Efficient and stable photo-oxidation of water by a bismuth vanadate photoanode coupled with an iron oxyhydroxide oxygen evolution catalyst, *J. Am. Chem. Soc.* **134**, 2186-2192 (2012).
20. Luo, W. J. et al. Solar hydrogen generation from seawater with a modified BiVO<sub>4</sub> photoanode, *Energy Environ. Sci.* **4**, 4046-4051 (2011).
21. Zhong, D. K., Choi, S., & Gamelin, D. R. Near-Complete Suppression of Surface Recombination in Solar Photoelectrolysis by "Co-Pi" Catalyst-Modified W:BiVO<sub>4</sub>, *J. Am. Chem. Soc.* **133**, 18370-18377 (2011).
22. Pilli, S. K. et al. Cobalt-phosphate (Co-Pi) catalyst modified Mo-doped BiVO<sub>4</sub> photoelectrodes for solar water oxidation, *Energy Environ. Sci.* **4**, 5028-5034 (2011).
23. Berglund, S. P., Rettie, A. J. E., Hoang, S., & Mullins, C. B. Incorporation of Mo and W into nanostructured BiVO<sub>4</sub> films for efficient photoelectrochemical water oxidation, *Phys. Chem. Chem. Phys.* **14**, 7065-7075 (2012).
24. Zhang, K., Shi, X. J., Kim, J. K., & Park, J. H. Photoelectrochemical cells with tungsten trioxide/Mo-doped BiVO<sub>4</sub> bilayers, *Phys. Chem. Chem. Phys.* **14**, 11119-11124 (2012).
25. Saito, R., Miseki, Y., & Sayama, K. Highly efficient photoelectrochemical water splitting using a thin film photoanode of BiVO<sub>4</sub>/SnO<sub>2</sub>/WO<sub>3</sub> multi-composite in a carbonate electrolyte, *Chem. Commun.* **48**, 3833-3835 (2012).
26. Eron, M. & Rothwarf, A. Interface Charging and Solar-Cell Characteristics - CuInSe<sub>2</sub>/CdS, *J. Appl. Phys.* **57**, 2275-2279 (1985).
27. Saad, M. & Kassis, A. Effect of interface recombination on solar cell parameters, *Solar Energy Materials and Solar Cells* **79**, 507-517 (2003).
28. Fossum, J. G. Physical operation of back-surface-field silicon solar cells, *Electron Devices, IEEE Transactions on* **24**, 322-325 (1977).
29. Dotan, H. et al. Probing the photoelectrochemical properties of hematite (alpha-Fe<sub>2</sub>O<sub>3</sub>) electrodes using hydrogen peroxide as a hole scavenger, *Energy Environ. Sci.* **4**, 958-964 (2011).
30. Duret, A. & Grätzel, M. Visible light-induced water oxidation on mesoscopic alpha-Fe<sub>2</sub>O<sub>3</sub> films made by ultrasonic spray pyrolysis, *J. Phys. Chem. B* **109**, 17184-17191 (2005).

31. Itoh, K. & Bockris, J. O. Thin-Film Photoelectrochemistry - Iron-Oxide, *J. Electrochem. Soc.* **131**, 1266-1271 (1984).
32. Tilley, S. D., Cornuz, M., Sivula, K., & Grätzel, M. Light-Induced Water Splitting with Hematite: Improved Nanostructure and Iridium Oxide Catalysis, *Angew. Chem. Int. Ed.* **49**, 6405-6408 (2010).
33. Alexander, B. D. et al. Metal oxide photoanodes for solar hydrogen production, *J. Mater. Chem.* **18**, 2298-2303 (2008).
34. Sivula, K., Le Formal, F., & Grätzel, M. Solar Water Splitting: Progress Using Hematite ( $\alpha\text{-Fe}_2\text{O}_3$ ) Photoelectrodes, *ChemSusChem* **4**, 432-449 (2011).
35. Brilliet, J. et al. Examining architectures of photoanode-photovoltaic tandem cells for solar water splitting, *J. Mater. Res.* **25**, 17-24 (2010).
36. Abdi, F. F., Firet, N., Dabirian, A., & van de Krol, R. Spray-deposited Co-Pi Catalyzed  $\text{BiVO}_4$ : a low-cost route towards highly efficient photoanodes, *MRS Online Proceedings Library* **1446**, (2012).
37. Jeremiasse, A. W. et al. Performance of metal alloys as hydrogen evolution reaction catalysts in a microbial electrolysis cell, *Int. J. Hydrogen Energy* **36**, 10482-10489 (2011).
38. Linic, S., Christopher, P., & Ingram, D. B. Plasmonic-metal nanostructures for efficient conversion of solar to chemical energy, *Nature Mater.* **10**, 911-921 (2011).
39. Warren, S. C. & Thimsen, E. Plasmonic solar water splitting, *Energy Environ. Sci.* **5**, 5133-5146 (2012).

## 6 Design Rules for Hybrid Photoelectrodes for Solar Water Splitting

Considering the limitations of existing materials for solar water splitting, a tandem configuration is most likely required for a highly efficient device. Here, we propose that a ‘hybrid photoelectrode’—where a photoanode and a photovoltaic (PV) cell are combined—is the best configuration to achieve high efficiency. Currently, ~5% stable solar-to-hydrogen (STH) efficiency has been demonstrated based on this configuration, with a combination of a bismuth vanadate ( $\text{BiVO}_4$ ) photoanode and a double-junction amorphous silicon PV cell. To further improve the efficiency, we identify important factors in the optimization steps, from the standpoint of the photoanode, the PV cell, and the combined device. From the photoelectrode perspective, a low onset potential and a high slope of the J-V curve are essential. A semiconductor with a high-energy conduction band edge is preferred in order to have a low onset potential, while the slope can be greatly enhanced by improving the catalytic and carrier separation efficiencies. We show experimental examples of these improvements in the case of  $\text{BiVO}_4$  photoanodes. Additionally, the PV cell in the hybrid photoelectrode configuration should be optimized for illumination with light transmitted through the photoanode, instead of the AM1.5 spectrum. Due to this optical inter-relation between the photoanode and the PV cell, general absorption improvement techniques commonly used for photoelectrodes (nanostructuring, substrate texturing, etc.) may not be suitable. We instead propose several light management techniques which take this inter-relation into consideration. This chapter should thus aim to provide some general design guidelines towards achieving a highly-efficient low-cost solar water splitting device.

## 6.1 Introduction

In the search for a low-cost renewable energy source to replace fossil fuels, there are three hard facts that need to be considered. First, sunlight is by far the most abundant and sustainable energy source available to mankind, with 36,000 TW reaching the land on the Earth's surface.<sup>1</sup> Second, considering the intermittency of this energy source and the world's current energy demand,<sup>2</sup> we need to store this solar energy on a TW-scale. Finally, the energy- and power-densities of chemical fuels are significantly greater than other storage solutions, and are thus hard to beat. For example, the specific energy-density of batteries is less than 1,000 Wh/kg, while it is close to 10,000 Wh/kg for gasoline.<sup>3</sup> Combining all these facts, using solar energy to produce chemical fuels (solar fuels) seems to be one of the most viable options to provide the world's future large scale energy needs. In addition, more than 80% of the total world's energy is consumed in the form of fuels, while only less than 20% is directly used in the form of electricity.<sup>4</sup> This means that there is already a huge infrastructure available for fuels, which will ease the transition from fossil fuels to solar fuels.

A very attractive route for the production of solar fuels is photoelectrochemical (PEC) water splitting, where photons from sunlight are utilized to oxidize and reduce water to form oxygen and hydrogen, respectively. Hydrogen can then be used directly as a fuel, either stored in pressurized tanks or in other forms (e.g. metal hydrides, liquefied hydrogen). Alternatively, it can be used as an intermediate in the production of more complex hydrocarbon fuels. For example, hydrogen can be fed to a Fischer-Tropsch reactor, together with carbon monoxide, to form several hydrocarbons such as methane or methanol.<sup>5</sup>

Despite the promising features of PEC water splitting, its implementation is currently hindered by the high cost and low efficiency of such a process. It has been estimated that the current technology of PEC water splitting through coupled photovoltaic (PV)-electrolyzer produces hydrogen at the cost of >US\$ 8 per kg or gge (gallons gasoline equivalent, 1 kg of H<sub>2</sub>  $\cong$  1 gge). This is much higher than the US\$ 2-4/kg target that is set by the United States Department of Energy for future hydrogen production pathways. Several techno-economic studies on direct PEC water splitting have been performed,<sup>6,7</sup> which identify the solar-to-hydrogen (STH) efficiency as the factor that most strongly affects the ultimate price per kg of hydrogen. If 10% STH efficiency could be achieved, combined with US\$ 160 per m<sup>2</sup> production cost and 15 years of lifetime, the cost of hydrogen in the range of US\$ 3-5/kg would be feasible.

The biggest challenge in reaching the 10% STH target efficiency lies in finding the optimal semiconductor material to be used as the photoelectrode. This ideal material

needs to fulfill many requirements,<sup>8-12</sup> and four decades of research efforts suggest that this is unlikely to be achieved by one single material. To circumvent this, more than one material can be combined to achieve highly efficient PEC water splitting. In fact, reports in the literature show that all systems with efficiency larger than 1% were achieved only in tandem configurations.<sup>13-22</sup> In these tandem arrangements, three or more components with different functionalities (light absorption, oxygen evolution, and hydrogen evolution) are combined to perform the overall PEC water splitting. Various architectures and materials have been proposed for the tandem configurations,<sup>13-18</sup> but the optimal device design is still not obvious.

In this chapter, we aim to elucidate the fundamental requirements that are necessary for an optimal tandem configuration for a PEC water splitting device. We propose that a hybrid photoelectrode concept—a system where a photoanode is integrated with a photovoltaic (PV) cell—is the best possible option to achieve highly efficient PEC water splitting. This is mainly driven by the better materials, cost, and optoelectronic perspectives that this configuration has to offer, as compared to other architectures. Additionally, rules and guidelines for the design of photoanode and PV cells for this hybrid photoelectrode concept are discussed. Here, we limit our scope to the application of thin film silicon PV cells, although we do not fully omit the possibility of using other types of cheap and efficient PV cells. This is mainly due to the relatively low-cost, high abundance, and vast knowledge on silicon-based solar cells, as well as the high degree of flexibility of the thin film silicon PV cells in terms of the optical and electrical characteristics. Finally, several issues from the point of view of the integrated device are outlined and addressed, revealing the optimized tandem configuration design.

## 6.2 Hybrid photoelectrode configurations

Several tandem designs for highly efficient PEC water splitting have been proposed in the past two decades,<sup>13-18</sup> and three particular configurations have emerged as viable options to reach high solar to hydrogen conversion efficiencies; (i) PV-electrocatalyst tandem, (ii) PV-photoelectrode tandems, and (iii) photoanode-photocathode tandems (shown in Figure 1). However, some of these devices are less promising compared to others due to issues of cost and scalability. For example, Licht et al. showed a solar water splitting device based on AlGaAs/Si and RuO<sub>2</sub>/Pt<sub>black</sub>.<sup>13</sup> While the STH efficiency for this PV-electrocatalyst system is very high (18.3%), the complexity of such architectures and the costs of the materials prohibit large-scale practical applications. The pros and cons of each device configuration will be discussed below in order to determine the performance limiting factors for each tandem system.



Emphasis will be placed on the application of low-cost, abundant materials as the building blocks of these tandem devices.

### Photovoltaic-Electrocatalyst (PV-EC)

Figure 6.1a shows the schematic structure and band diagram for the PV-electrocatalyst tandem device. In this configuration, a triple-junction amorphous silicon (a-Si) solar cell is used as the photovoltaic element in the system. This method has been demonstrated almost thirty years ago by Delahoy et al.<sup>14</sup> The combination of a 3-jn a-Si solar cell, RuO<sub>2</sub> as the oxygen evolution catalyst, and Pt as the hydrogen evolution catalyst, resulted in an STH efficiency of 1.8% for this device. One decade after this initial effort, Rocheleau et al. demonstrated a 7.8% efficient wired device using a 3-jn a-Si solar cell combined with Co-Mo hydrogen evolution catalyst as the cathode, and Ni-Fe-O as the anode.<sup>20</sup> Yamada et al. later showed an integrated (wireless) device based on similar materials, having a much lower efficiency of 2.5%.<sup>21</sup> These early efforts however were performed in highly acidic or alkaline conditions, which is rather undesired for large scale applications. Using the same concept, along with the discovery of cobalt-based water oxidation catalysts that work in near-neutral pH conditions,<sup>23</sup> Reece et al. recently demonstrated an STH efficiency of 4.7% and 2.5% in wired and wireless configurations, respectively.<sup>15</sup>

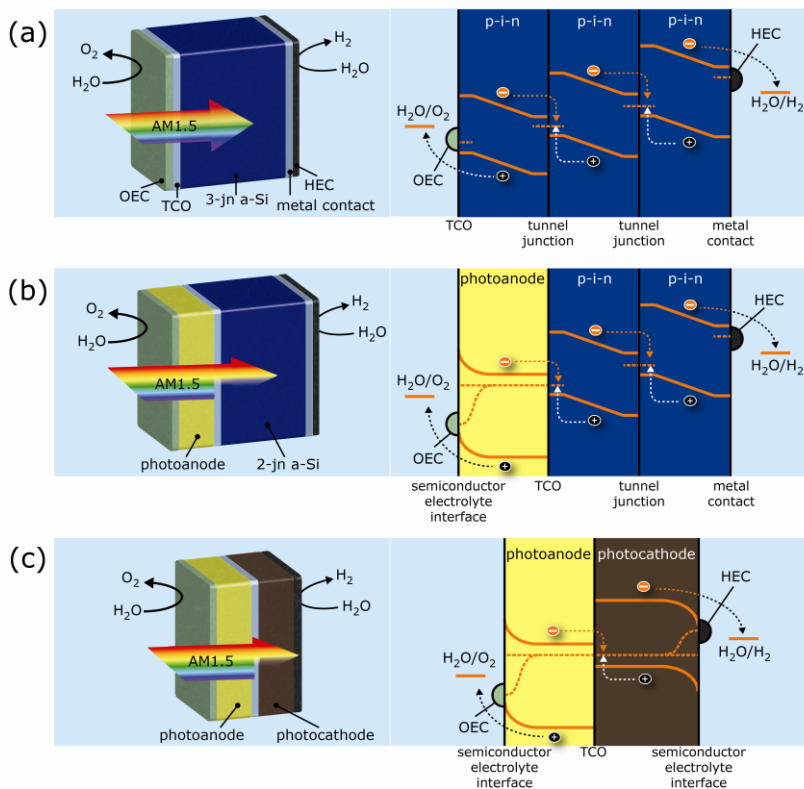


**Figure 6.1.** Schematic structure and band diagram of (a) PV-electrocatalyst tandem, (b) PV-photoelectrode tandem, and (c) photoanode-photocathode tandem configurations.

Although the progress in improving the efficiency of these PV-electrocatalyst tandem devices seems promising, the feasibility of significant further improvements in performance is doubtful. To illustrate this, Figure 6.2 shows the J-V curves of a cobalt-based oxygen evolution catalyst (Co-OEC, solid black curve) and a 3-jn a-Si solar cell (solid red curve). The intersection of these two curves represents the operating point of an electrocatalyst-PV tandem device, similar to what is shown recently by Nocera and coworkers.<sup>15</sup> Based on the onset potential of the Co-OEC J-V curve, which is determined from the thermodynamic overpotential required for water splitting,<sup>24</sup> a solar cell with an open circuit potential of at least 1.6 V is needed. The application of a 3-jn a-Si solar cell in this device is therefore an essential requirement. This is confirmed by a recent modeling study by Winkler et al.,<sup>25</sup> where they indicated that three or four amorphous silicon solar cells are needed in series for an

electrocatalyst-PV tandem configuration. If a simpler solar cell such as a double-junction a-Si (2-jn a-Si, Fig. 6.2 dashed red curve) were used, the STH efficiency of the resulting device would be greatly diminished (~1.5% STH maximum). It is therefore clear that the solar cell's performance is the limiting factor in this configuration and that any major improvements would require PV devices with higher operating voltages and currents. Considering that the 3-jn a-Si solar cells are already highly optimized and quite complex, it is unlikely that an electrocatalyst-PV tandem device with better performance and good economic viability can be developed.

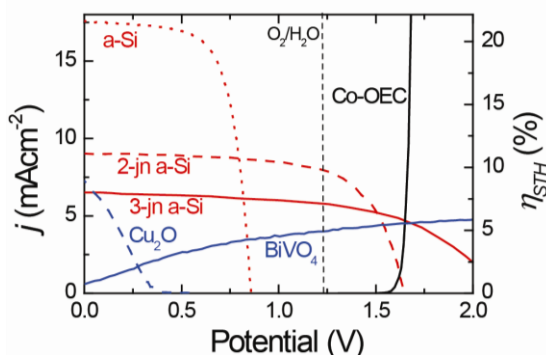


**Figure 6.2.** Current-voltage characteristics of cobalt-based oxygen evolution catalyst (solid black),<sup>26</sup> state-of-the-art BiVO<sub>4</sub> photoanode (solid blue),<sup>22</sup> state-of-the-art Cu<sub>2</sub>O photocathode (dashed blue),<sup>27</sup> and triple-junction (solid red), double-junction (dashed red), and single-junction (dotted red) amorphous silicon solar cells. The J-V curves of the amorphous silicon solar cells are measured at the Photovoltaic Materials and Devices (PVMD) laboratory, TU Delft. The vertical dashed line indicates the thermodynamic potential for water oxidation.

#### Photovoltaic-Photoelectrode (PV-PEC)

In the second tandem configuration (Fig. 6.1b), a PV device is combined with a semiconductor photoelectrode to perform the water splitting reactions. Either a water oxidation (photoanode) or a water reduction (photocathode) photoelectrode can be applied in this configuration with hydrogen evolution catalysts (e.g. Pt, RuO<sub>2</sub>, MoS<sub>2</sub>) serving as the counter electrodes in either case. Upon illumination, the photoelectrode absorbs the short wavelength part of the solar spectrum due to the relatively large bandgap of these materials. The transmitted light not absorbed by the photoelectrode is then used by the PV device to provide the photoelectrode with the needed additional potential for water splitting. This configuration is also called a “hybrid

photoelectrode”, a term first coined by Miller et al.<sup>28</sup> To illustrate the potential of this method, Khaselev and Turner demonstrated a monolithic PV-PEC device which has 12.4% STH efficiency as early as 15 years ago.<sup>16</sup> However, the device consisted of high-quality GaAs and GaInP<sub>2</sub> materials, which are expensive and unstable in aqueous electrolytes. Although efforts are ongoing in reducing the cost and improving the stability of this device, these particular materials are not going to be considered in this paper.

To address the stability issue, Miller et al. proposed a hybrid photoelectrode concept based on a cheap semiconducting metal oxide photoelectrode and an amorphous silicon solar cell.<sup>18, 28, 29</sup> A tandem device consisting of a 2-jn a-Si solar cell and a tungsten trioxide (WO<sub>3</sub>) photoanode with a projected 2.2% STH efficiency and 0.6% demonstrated efficiency was reported.<sup>18</sup> This configuration has recently been improved using a combination of molybdenum-doped and undoped WO<sub>3</sub>, and an STH efficiency of 3% has been achieved.<sup>19</sup>

Based on the same concept, we also recently reported a tandem device consisting of a 2-jn a-Si solar cell and a bismuth vanadate (BiVO<sub>4</sub>) photoanode with 4.9% STH efficiency,<sup>22</sup> see also Chapter 5. The BiVO<sub>4</sub> can give higher efficiencies than the WO<sub>3</sub> due to the smaller bandgap. The key to achieve high photocurrents for BiVO<sub>4</sub> was to enhance the carrier separation as well as its catalytic efficiency.

While the reported efficiency for this device configuration is still lower than the 10% STH efficiency target,<sup>7</sup> the hybrid photoelectrode concept based on a cheap semiconducting metal oxide photocatalyst and a 2-jn a-Si solar cell has several distinct advantages. As compared to the 4.7% efficient electrocatalyst-PV tandem,<sup>15</sup> the hybrid photoelectrode achieved slightly higher efficiency (4.9%), while replacing four layers (the p-i-n layers of the a-Si and the tunnel barrier) with a single cheap metal oxide photoelectrode. The performance of the hybrid photoelectrode is generally limited by the metal oxide photoelectrode, as opposed to the PV materials in the PV-EC configuration. Figure 6.2 shows the J-V curve of the BiVO<sub>4</sub> photoanode (solid blue) and 2-jn a-Si solar cell (dashed red), and once again the intersection of these curves is the operating point for the tandem device. Based on these two curves, significant improvement is not expected by replacing the solar cell with a more complex one (e.g. 3-jn a-Si). Instead, to increase the operating current of the device, it is obvious that one would need to improve the performance of the BiVO<sub>4</sub> photoanode. The maximum photocurrent one could theoretically obtain from BiVO<sub>4</sub> is ~7.5 mA/cm<sup>2</sup> (~9.2% STH efficiency), so there is still room for significant improvement. This means that the 2-jn a-Si/BiVO<sub>4</sub> device can be improved by at least another 50% without increasing the complexity of the device. In fact, further improvements of the BiVO<sub>4</sub> may lead to an even simpler PV device based on a single a-Si junction. We recently obtained an STH efficiency of 3.6% by combining the state-of-the-art BiVO<sub>4</sub> photoanode and a 1-jn a-Si solar cell.<sup>22</sup> Brilliet et al. also recently reported a 3.1% efficient tandem device based on a WO<sub>3</sub> photoanode and a dye-sensitized solar cell (DSSC).<sup>17</sup> Clearly, these much

simpler PV devices cannot be used for the PV-electrocatalyst their open circuit voltages are too low ( $<1.0$  V).

Utilizing the hybrid photoelectrode configuration therefore offers better perspectives for improved PEC water splitting as compared to the PV-electrocatalyst tandem configuration. Based on the J-V curve of a 1-jn a-Si solar cell (Fig. 6.2, dotted red curve), a photocurrent of  $\sim 17$  mA/cm<sup>2</sup> is available at potentials of  $\sim 0.6$  V. Further improvement of the STH efficiency of the hybrid photoelectrode device can be achieved by the application of a metal oxide photocatalyst with a smaller bandgap. Assuming that a metal oxide with a 1.9 eV bandgap can be found with a quantum efficiency above 50% and a sufficiently low onset potential, an STH efficiency of 10-15% is within reach.

### Photoanode-Photocathode (PEC-PEC)

Finally, one could combine two photoelectrodes to make a tandem device: an n-type semiconductor photoanode and a p-type photocathode. This configuration simply replaces the solar cell in the hybrid photoelectrode with a second photocatalyst. The schematic and band structure diagram for such a device are depicted in Fig. 6.1c. In this device, the shorter wavelength light will be absorbed by the first photocatalyst and the transmitted light by the second. While this method arguably offers the simplest architecture among the three discussed here, the performance of such devices is still very low.<sup>30-33</sup> This is mainly caused by the relatively low open circuit voltage of the photocathode ( $< 0.5$  V) as well as the poor fill factor (the ratio of the maximum obtainable power to the product of the open circuit voltage and the short circuit current). The highest efficiency reported for a PEC-PEC tandem device is only 0.22%, achieved by combining a WO<sub>3</sub> photoanode and a Cu<sub>2</sub>O/NiO<sub>x</sub> composite photocathode.<sup>31</sup> Moreover, most highly efficient photocathodes suffer from having poor stability (GaInP<sub>2</sub>, Cu<sub>2</sub>O, CuGaSe<sub>2</sub>, etc.). Recent efforts are ongoing in stabilizing these materials using protective overlayers. However, these overlayers are usually deposited with a technique which is more difficult for large scale operation (e.g. atomic layer deposition), increasing the device complexity and cost. Figure 6.2 shows the J-V curve of the state-of-the-art Cu<sub>2</sub>O photocathode (dashed blue), as reported by Paracchino et al.<sup>27</sup> Considering that the current density in this photocathode is much lower than that of the PV devices—as a result of the generally lower photovoltage than for a Si based p-n junction—and is considerably more complex than a simple PV device, it is therefore currently more sensible to simply use a PV device in a hybrid photoelectrode concept, which has proven to already give much higher efficiency.

We can now summarize our analysis as follows. A PV-electrocatalyst tandem offers relatively high efficiency, however its progress is hindered by the need for more complex solar cells. A PV-photoelectrode tandem (hybrid photoelectrode) is currently capable of delivering the same level of efficiency with a simpler and relatively cheaper

architecture, and there is a potential of much higher efficiency if the photoelectrode performance can be improved. This also relaxes the requirement for the type of solar cell needed. A photoanode-photocathode tandem is the simplest architecture; however the efficiency is much lower than for the other two configurations due to the low photovoltages, while the performance is further limited by the poor stability of the photocathode. It is therefore concluded that the hybrid photoelectrode is the optimal design to achieve low-cost, highly-efficient photoelectrochemical water splitting. The challenge then lies in the optimization of the photoelectrodes, solar cells, and other device components which is addressed in the following sections.

### **6.3 Optimum photoelectrode for hybrid photoelectrode**

As mentioned above, the efficiency of the hybrid photoelectrode is limited by the performance of the metal oxide photoelectrode. The requirements for an ideal semiconductor for PEC water splitting has been outlined and discussed previously, needing to meet the following criteria:<sup>8-12</sup> (i) high solar absorption, (ii) suitable band edge positions for water reduction/oxidation, (iii) high catalytic activity, (iv) efficient charge separation, (v) high stability, and (vi) low cost. While all the requirements should be applicable to the metal oxide photoelectrode for the hybrid photoelectrode configuration, some are more important than others. In this section, we will extensively discuss these important parameters to achieve an optimum photoelectrode that is suitable for integration in a highly efficient hybrid photoelectrode for solar water splitting. For simplicity, we will focus our discussion on the use of photoanodes in combination with PV cells, and not discuss the integration of photocathodes with solar cells in detail.

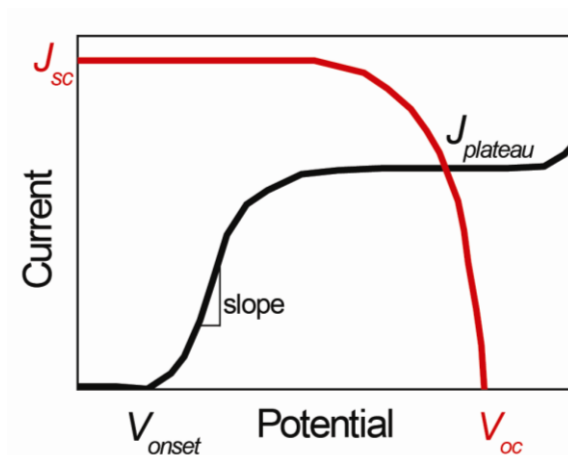


**Figure 6.3.** Typical current-potential (J-V) curves of a photoanode (black) and a PV cell (red), including the important parameters in the hybrid photoelectrode measurement.  $J_{SC}$ : short-circuit current;  $V_{OC}$ : open circuit potential;  $V_{onset}$ : onset potential;  $J_{plateau}$ : plateau photocurrent.

Before we discuss the specific requirements for the metal oxide photoelectrodes, it is important to first identify the performance metrics used to assess the hybrid photoelectrode. Figure 6.3 shows a typical two-electrode current-potential (J-V) curve of a photoanode and a PV cell under illumination. In the hybrid photoelectrode, the intersection of these two curves is the operating point. From the photoanode point of view, there are three important parameters in the J-V curve: (i) the onset potential ( $V_{onset}$ ), (ii) the slope of the J-V curve, and (iii) the photocurrent plateau ( $J_{plateau}$ ). In addition, the important parameters for the solar cell are also shown: open circuit potential ( $V_{OC}$ ) and short-circuit current ( $J_{SC}$ ). A third important parameter is the solar cell's fill factor, which plays a comparable role to the slope of the photoanode's J-V curve. For an optimum operation of the hybrid photoelectrode, the photoanode should have a  $V_{onset}$  that is much lower than  $V_{OC}$ , a high slope, and a  $J_{plateau}$  which is close to the  $J_{SC}$ .

The application of a photoanode material with a low  $V_{onset}$  is essential for a hybrid photoelectrode. The lower the  $V_{onset}$ , the more relaxed the requirements are for the adjoining solar cells. A very important property of the photoanode material that defines the  $V_{onset}$  is the position of the conduction band, as illustrated in Fig. 6.4. Figure 6.4a shows the position of the conduction and valence bands of the three most promising metal oxide photoanodes:  $Fe_2O_3$ ,  $WO_3$ , and  $BiVO_4$ . The valence band levels of these oxides are low enough for oxygen evolution to occur, however their conduction band levels are lower than the hydrogen evolution potential. While this implies that unassisted solar water splitting cannot occur for these materials as a single

photoelectrode, it is possible in the hybrid photoelectrode configuration. This is because the additional potential that is needed to overcome the difference between the conduction band edge and the hydrogen evolution potential can be supplied by the solar cell. The onset potential is determined by this difference in energy level and the needed overpotential for hydrogen evolution ( $\sim 0.1-0.3$  V). An additional 0.4 V is usually needed before appreciable photocurrent is achieved, due to the generally modest slope of the J-V curve. Therefore, to ensure that the application of a simple PV cell is sufficient ( $V_{OC} < 1.0$  V), the conduction band edge should not be located more than 0.5 V below the hydrogen evolution potential. Figure 6.4b shows the J-V curve of a state-of-the-art  $\text{Fe}_2\text{O}_3$ ,<sup>17</sup>  $\text{WO}_3$ ,<sup>17</sup> and  $\text{BiVO}_4$ <sup>22</sup> photoanode. The onset potential is decreasing in the order of  $\text{Fe}_2\text{O}_3 \rightarrow \text{WO}_3 \rightarrow \text{BiVO}_4$ . This trend is consistent with the trend in the difference between hydrogen evolution potential and the conduction band edge (Fig. 6.4a). When combined with a simple single-junction a-Si solar cell, a  $\text{BiVO}_4$ -based hybrid photoelectrode therefore has the highest efficiency, despite all of them having similar  $J_{\text{plateau}}$  (Fig. 6.4b). The application of a photoanode which has a conduction band edge close to the hydrogen evolution potential is therefore very important for realizing a high efficiency tandem water splitting device.

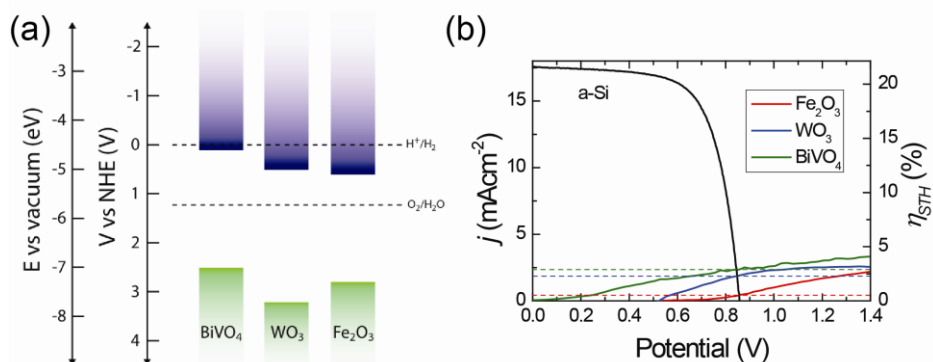


**Figure 6.4.** (a) Position of conduction (blue) and valence (green) band of  $\text{Fe}_2\text{O}_3$ ,  $\text{WO}_3$ , and  $\text{BiVO}_4$  at pH 0. (b) J-V curve of a single-junction a-Si solar cell (black), a  $\text{Fe}_2\text{O}_3$  (red), a  $\text{WO}_3$  (blue), and a  $\text{BiVO}_4$  (green) photoanode. The horizontal dashed lines represent the operating points, and thus the respective efficiencies of the combined devices.

The second important parameter in the J-V curve of the photoanode is its slope, as indicated in Fig. 6.3. An ideal photoanode will have a slope of  $\infty$  (infinity), which means that the photocurrent goes instantaneously to  $J_{\text{plateau}}$ , as soon as the potential goes above  $V_{\text{onset}}$ . While this is not possible in practice, we would like to have the



slope of the photocurrent as steep as possible. Reichman derived the expression for the current-potential characteristics of semiconductor-electrolyte junction as the following.<sup>34</sup>

$$J = \frac{J_0 + q\Phi \left( \frac{1 - \exp(-\alpha W)}{1 + \alpha L} \right) - J_0 \exp(qV / kT)}{1 + \frac{J_0 \exp(qV / kT)}{I^0}} \quad (6.1)$$

where  $J$  is the photocurrent density,  $J_0$  is the saturation current density,  $\Phi$  is the incident photon flux,  $\alpha$  is the absorption coefficient,  $q$  is the elementary charge,  $V$  is the potential,  $k$  is Boltzmann constant,  $T$  is temperature,  $L$  is the carrier diffusion length,  $I^0$  is the carrier exchange current parameter across the semiconductor-electrolyte interface, and  $W$  is the width of the depletion layer, which is given by the following relationship:

$$W = \sqrt{\frac{2\varepsilon_r \varepsilon_0 (\phi_b - V)}{qN}} \quad (6.2)$$

where  $\varepsilon_r$  is the dielectric constant,  $\varepsilon_0$  is vacuum permittivity,  $\phi_b$  is the equilibrium band bending voltage, and  $N$  is the carrier density.

Although equation (6.1) seems quite complicated, it can be broken down into three simple components: carrier generation (photon absorption), carrier injection from the semiconductor to the electrolyte (catalysis) and carrier separation in the semiconductor. A simplified equation can therefore be written:

$$J = J_{abs} \times \eta_{cat}(V) \times \eta_{sep}(V) \quad (6.3)$$

where  $J_{abs}$  is the absorbed photons expressed as current density,  $\eta_{cat}(V)$  is the catalytic efficiency as a function of potential, and  $\eta_{sep}(V)$  is the carrier separation efficiency as a function of potential. Since  $J_{abs}$  is not affected by potential, to improve the slope of the J-V curve, it is important to improve the catalytic efficiency and charge separation of the photoanode material.

To illustrate this, we show the examples of the slope improvement in BiVO<sub>4</sub> photoanodes. Poor surface catalysis has been identified as the performance limiting factor in BiVO<sub>4</sub> photoanodes,<sup>35-38</sup> reflected by a small slope in the J-V curve of BiVO<sub>4</sub> (Fig. 6.5, black). To improve this, a cobalt phosphate (Co-Pi) catalyst was electrodeposited onto the surface of BiVO<sub>4</sub>. Co-Pi is known to be an effective water oxidation catalyst on BiVO<sub>4</sub>, and other semiconductor photoanodes (Fe<sub>2</sub>O<sub>3</sub>, etc.).<sup>35,36</sup>

As a result, the slope of the J-V curve is improved significantly (Fig. 6.5, red). In addition, poor carrier separation caused by the slow electron transport is also known to limit the performance of  $\text{BiVO}_4$  photoanode.<sup>36, 37</sup> We recently reported that gradient-doping of tungsten—which replaces the vanadium—in  $\text{BiVO}_4$  can improve the carrier separation significantly.<sup>22</sup> This improvement results in a steeper rise of the J-V curve, as shown in Fig. 6.5 (blue). For a hybrid photoelectrode, this means that although the onset potential is relatively constant, the operating photocurrent is much higher when a high slope of the photoanode’s J-V curve is achieved. To the best of our knowledge, this is the first time that the slope of the J-V curve is explicitly defined and demonstrated to be a function of the catalytic and the carrier separation efficiency.

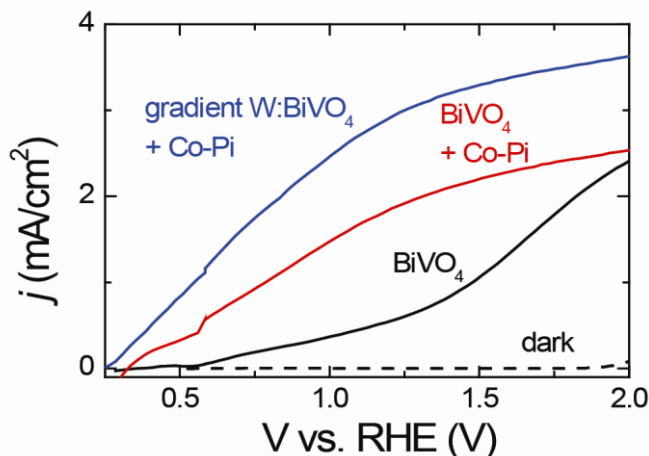


**Figure 6.5.** AM1.5 photocurrent vs voltage of  $\text{BiVO}_4$  (black), Co-Pi-catalyzed  $\text{BiVO}_4$  (red) and gradient-doped Co-Pi-catalyzed  $\text{W:BiVO}_4$  (blue) photoanode in 0.1 M potassium phosphate buffer electrolyte (pH  $\sim$ 7.3). The dark current is shown as dashed black curve.

Finally, if the onset potential and the slope of the J-V curve would have been optimized, increasing  $J_{\text{plateau}}$  will improve the performance of the hybrid photoelectrode even further. This, too, can be partially achieved by improving the carrier separation, as illustrated in Fig. 6.5 (red vs blue curve); however, a more significant factor to increase  $J_{\text{plateau}}$  is to increase the light absorption. Nanostructuring, bandgap engineering, and other light management techniques can therefore be applied. One, however, needs to be careful in the efforts of improving light absorption of the photoanode in the hybrid photoelectrode, since more light absorbed in the photoanode may result in less photons being available for the PV cell. This delicate trade-off

between light absorption in the photoanode and the PV cell will be discussed in a later section of this chapter.

#### 6.4 Optimum PV cell for hybrid photoelectrode

In order to achieve a highly-efficient hybrid photoelectrode, the PV cell used in conjunction with the photoanode should be designed carefully. Although we do not completely ignore the possibility of other cheap and efficient solar cells, the discussion in this paper is limited to thin film silicon solar cells. Silicon is earth-abundant, non-toxic, relatively low-cost and widely investigated both in academic research and industry. Additionally, the parameters in thin film silicon solar cells ( $V_{OC}$ ,  $J_{SC}$ , fill factor) can be highly tuned by employing various multi-junctions of silicon (e.g. amorphous-amorphous, micromorphous tandem structures) or different silicon alloys (e.g. silicon-germanium, silicon oxide, silicon carbide). This high degree of flexibility allows the application of a more optimized solar cell with respect to the performance of the metal oxide photoelectrode.

The first consideration for the PV cell is related to its optical properties. In a hybrid photoelectrode, the PV cell is positioned behind the photoanode (Fig. 6.1b). Since the photoanode absorbs most of the light with energy higher than its bandgap, the light-absorption layer in the PV cell should have a lower bandgap than that of the photoanode. This way, we ensure that the PV cell will have access to enough photons from the transmitted light spectrum. Figure 6.6 shows the AM1.5 spectrum as well as the transmitted spectrum of the  $\text{BiVO}_4$  photoanode as a function of wavelength. Only photons with wavelength smaller than 520 nm are absorbed by  $\text{BiVO}_4$  ( $E_g$  of  $\text{BiVO}_4$  is  $\sim 2.4$  eV). Any PV cell used in conjunction with  $\text{BiVO}_4$  should therefore be able to use the transmitted part of the solar spectrum (Fig. 6.6) to provide enough  $J_{SC}$  and  $V_{OC}$ .

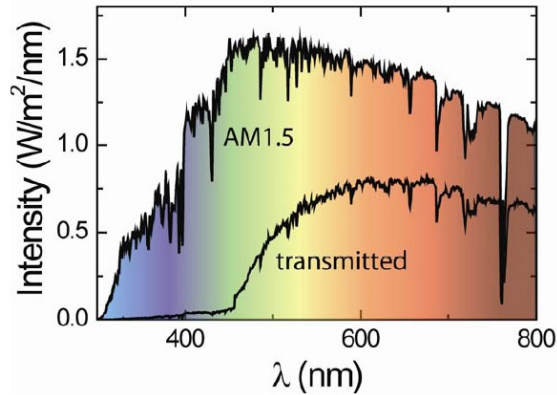


**Figure 6.6.** AM1.5 spectrum and the measured fraction of the light that reaches the PV cell via transmission through a 200 nm-thick  $\text{BiVO}_4$  photoanode in the hybrid photoelectrode configuration.

Stand-alone PV devices are generally optimized according to the standard AM1.5 ( $100 \text{ mW/cm}^2$ ) solar spectrum. This is, however, not optimal for the case when PV devices are used in the hybrid photoelectrode configuration. Instead, they should be optimized according to the spectrum transmitted through the photoelectrode, which is markedly different from the AM1.5 spectrum. To illustrate this, we compare three different 2-jn a-Si solar cells with varying thickness of the top intrinsic layer (i-layer), as shown in Table 6.1. In amorphous silicon solar cells, the i-layer is where photons are absorbed and carriers are therefore generated. PV A, B, and C have the same bottom i-layer thicknesses, but the top i-layer thicknesses are 50, 75 and 100 nm, respectively. Under AM1.5 illumination, the PV cell with the thinnest top i-layer (PV A) has the highest  $J_{SC}$  of  $8.11 \text{ mA/cm}^2$  as well as the highest efficiency ( $\eta$ ) of 9.62%. However, when PV A is subjected to the transmitted spectrum of  $\text{BiVO}_4$  photoanode, it results in the lowest  $J_{SC}$  of  $2.87 \text{ mA/cm}^2$  and  $\eta$  of 3.36%. Instead, the PV cell with the thickest top i-layer (PV C) has the highest  $J_{SC}$  of  $3.56 \text{ mA/cm}^2$  and  $\eta$  of 4.17% under the transmitted spectrum. Therefore, while PV A has the highest efficiency with  $\text{BiVO}_4$  photoanode.

**Table 6.1.** Performance metrics (simulated) for three double junction amorphous silicon solar cells of varying top i-layer thickness under AM1.5 and transmitted spectrum, as shown in Fig. 6.6.

PV cell	Top i-layer thickness (nm)	Bottom i-layer thickness (nm)	AM1.5			BiVO <sub>4</sub> -filtered		
			$J_{SC}$ (mA/cm <sup>2</sup> )	$V_{OC}$ (V)	$\eta$ (%)	$J_{SC}$ (mA/cm <sup>2</sup> )	$V_{OC}$ (V)	$\eta$ (%)
A	50	350	8.11	1.72	9.62	2.87	1.67	3.36
B	75	350	7.32	1.72	8.59	3.42	1.68	3.92
C	100	350	6.19	1.68	7.24	3.56	1.63	4.17

The J-V characteristics of a PV cell also define the suitability of its combination with a certain photoanode. Although a certain PV cell is ideal for one particular photoanode, it does not necessarily mean that it will be the optimum for every photoanode. Figure 6.7 shows the J-V curves of three different type of amorphous silicon solar cells: (i) single-junction amorphous silicon (a-Si, solid blue curve), (ii) double-junction amorphous/nano-crystalline silicon (a-Si/nc-Si, solid red curve), and (iii) double-junction amorphous silicon (a-Si/a-Si, solid black curve). The J-V curves of three hypothetical photoanodes with varying onset potential—but with the same plateau photocurrent and slope—are also shown. Depending on the onset potential of the photoanode, different types of solar cells have to be chosen. In the case of the high  $V_{onset}$  photoanode (Fig. 6.7, dashed black curve), an a-Si solar cell does not have enough potential to produce a significant efficiency. Either an a-Si/nc-Si or an a-Si/a-Si solar cell has to be used. The combination with a-Si/a-Si solar cell results in the highest efficiency, i.e., 4.5% (vs. 2.5% for a-Si/nc-Si). Similarly, by comparing the intersection between the photoanode's and the solar cell's J-V curve, the medium  $V_{onset}$  photoanode (Fig. 6.7, dashed red curve) should be combined with the a-Si/nc-Si solar cell to give an efficiency of 6%, and the low  $V_{onset}$  photoanode (Fig. 6.7, dashed blue curve) with the a-Si solar cell results in more than 8% efficiency.

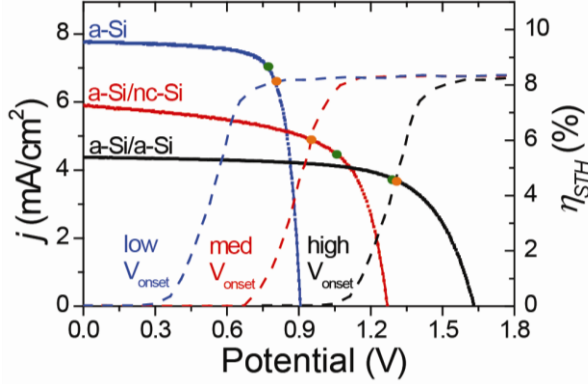


**Figure 6.7.** Current-potential (J-V) curves of a double-junction amorphous silicon solar cell (a-Si/a-Si, solid black), a double-junction amorphous/nano-crystalline solar cell (a-Si/nc-Si, solid red), and a single-junction amorphous solar cell (a-Si, solid blue). J-V curves of three hypothetical photoanodes with low (dashed blue), medium (dashed red), and high (dashed black) onset potential are also shown. The J-V curves of the solar cells were measured in the PVMD laboratory, TU Delft, under the transmitted spectrum as shown in Fig. 6.6. The orange circles are the operating point of the respective hybrid photoelectrodes, while the green circles are the maximum power point (MPP) of each solar cells.

Finally, it is important to note that the efficiency of the solar cell is defined differently than the efficiency of the hybrid photoelectrode. The efficiency of a solar cell is the ratio of the maximum power generated by the solar cell to the illumination intensity, which can be written to the following equation:

$$\eta = \frac{V_{MPP} \text{ (V)} \times J_{MPP} \text{ (mA/cm}_2\text{)}}{P_{in} \text{ (mW/cm}^2\text{)}} \quad (6.4)$$

where  $V_{MPP}$  is the voltage at the maximum power point,  $J_{MPP}$  is the current density at the maximum power point, and  $P_{in}$  is the intensity of the incident spectrum ( $100 \text{ mW/cm}^2$  for AM1.5). In a hybrid photoelectrode, the operating point (the intersection between the J-V curves of the photoanode and the solar cell) is not always the same as the maximum power point of the solar cell (see Fig. 6.7). The efficiency of the hybrid photoelectrode (STH efficiency) is therefore only subjected to the photocurrent density at the operating point, as shown in the following equation:

$$\eta_{STH} = \frac{1.23 \text{ (V)} \times J_{OP} \text{ (mA/cm}^2\text{)} \times \eta_{Faradaic}}{P_m \text{ (mW/cm}^2\text{)}} \quad (6.5)$$

where  $J_{OP}$  is the current density at the operating point of the hybrid photoelectrode and  $\eta_{Faradaic}$  is the Faradaic efficiency of the hydrogen and oxygen evolution reaction. Any direct relationship between the efficiency of the hybrid photoelectrode ( $\eta_{STH}$ ) and the solar cell ( $\eta$ ) is therefore non-existent and should not be used to determine the efficiency of a particular redox reaction.

## 6.5 Device optimization

When the photoanode and the solar cell have been optimized, several issues from the point of view of the whole device configuration need to be addressed for further improvement of the resulting hybrid photoelectrode. As discussed previously, one of the most crucial factors is related to the light management for both the photoanode and the PV cell. Currently, the performance of the photoanode is the limiting factor in the hybrid photoelectrode. One way to increase its photocurrent is by increasing the absorption. However, more absorption in the photoanode means less photons are being transmitted to the solar cell, which can have a negative impact on the total device performance.

One way to enhance the absorption is by texturing the transparent conductive oxide (TCO) film, which scatters the light and increases the path-length that the photons travel through the material. This is an example of a light trapping approach which has been widely investigated for thin film PV cells in the recent decades.<sup>39, 40</sup> Figure 6.8 shows the J-V curves of a gradient-doped W:BiVO<sub>4</sub> photoanode on a flat TCO substrate (solid black) and a textured TCO substrate (solid red). As a result of the increased absorption, the photocurrent of the BiVO<sub>4</sub> photoanode on a textured TCO substrate is higher. At the same time, however, this results in lower  $J_{SC}$  and  $V_{OC}$  of the 2-jn a-Si solar cell (Fig. 6.8, dashed red vs. dashed black). While in this case the resulting efficiency is still improved by the introduction of textures, further absorption increases through relatively general methods (e.g. thickness optimization, nanostructuring) may present a detrimental effect to the overall efficiency.

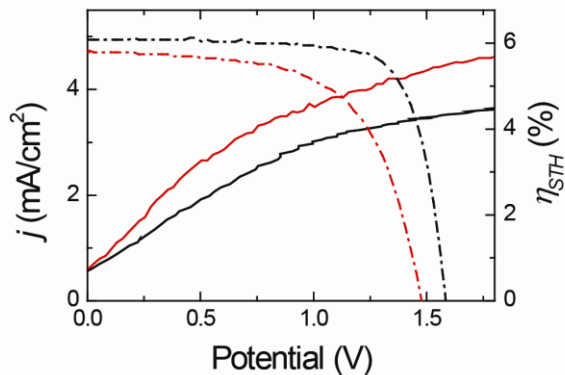


**Figure 6.8.** J-V curves of the state-of-the-art BiVO<sub>4</sub> photoanode on flat (solid black) and textured (solid red) TCO substrates. The J-V curves of the 2-jn a-Si solar cell behind each type of BiVO<sub>4</sub> photoanodes are shown in dashed with the respective color.

The selective absorption improvement of a particular wavelength range is much more advantageous in the hybrid photoelectrode configuration. In this case, light can be directed to be absorbed more efficiently in either the photoanode or the solar cell. An example of this is the implementation of plasmonic nanoparticles on the surface or at the back interface of the photoanode to selectively increase the absorption of a certain wavelength region (Fig. 6.9a). A recent study on implementing silica covered gold (Au/SiO<sub>2</sub>) nanoparticles on the surface of hematite ( $\alpha$ -Fe<sub>2</sub>O<sub>3</sub>) results in a ~20-fold photocurrent improvement at wavelength of 590 nm and a total AM1.5 photocurrent enhancement of 7%.<sup>41</sup>



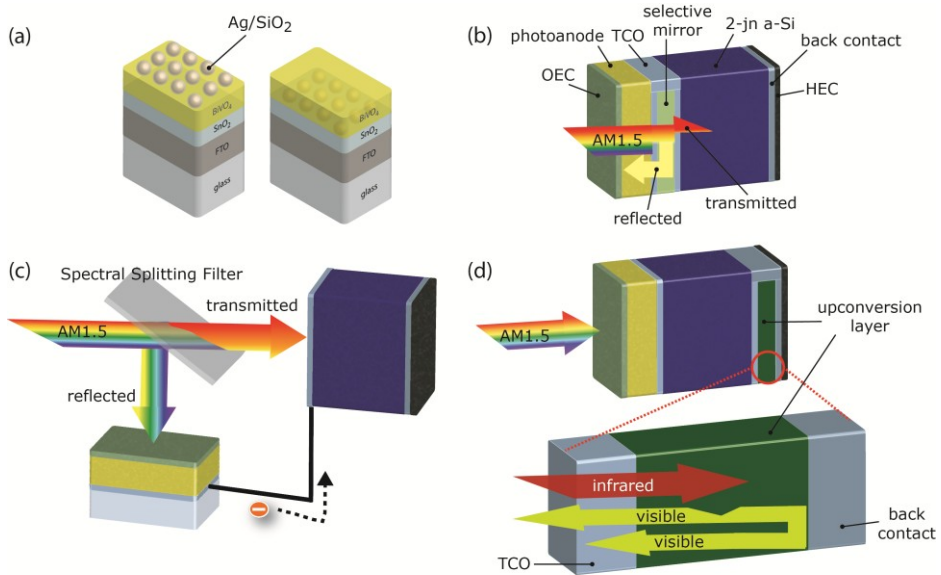


**Figure 6.9.** Applicable light management techniques for hybrid photoelectrode: **(a)** plasmonic enhancement, **(b)** ‘selective mirror’, **(c)** spectral splitting filter, and **(d)** up-conversion.

Alternatively, a ‘selective mirror’ can be inserted between the photoanode and the PV cell, as shown in Fig. 6.9b. This “selective mirror” is a single- or multi-layer thin film designed to selectively reflect shorter wavelength lights back to the photoanode and transmit the longer wavelength to the PV cell. We have performed an absorption simulation study on the hybrid photoelectrode, consisting of a  $\text{BiVO}_4$  photoanode and a 2-jn a-Si solar cell, using the Advanced Semiconductor Analysis (ASA) simulation package.<sup>42</sup> Two single-layer thin films are considered: aluminum-doped zinc oxide (AZO) and tin-doped indium oxide (ITO), both are optimized to be 150 nm-thick. As shown in Fig. 6.10, the insertion of either films successfully improve the absorption of shorter wavelength lights in  $\text{BiVO}_4$  photoanode, without any reduction of the transmission of longer wavelength lights towards the 2-jn a-Si solar cell. While the total absorption increase in this case is relatively modest (4.3-6.4%), further enhancement can be expected with the application of a multi-layer thin film with alternating refractive indices (distributed Bragg reflector—DBR<sup>43</sup>) as the ‘selective mirror’.

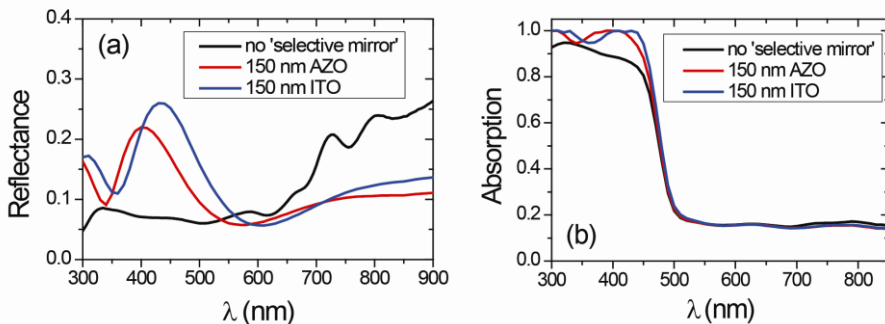


**Figure 6.10.** (a) Reflectance of the 2-jn a-Si solar cell and (b) absorption of BiVO<sub>4</sub> photoanode in the hybrid configuration without ‘selective mirror’ (black) and with either 150 nm-thick aluminum-doped zinc oxide (red) or 150 nm-thick tin-doped indium oxide (blue).

Similar to the “selective mirror” technique, a spectral-splitting filter (SSF), which has been investigated extensively in concentrated PV systems,<sup>44</sup> can be applied to a re-designed hybrid photoelectrode (see Fig. 6.9c). Since the SSF has high reflection for light with short wavelengths and high transmission for long wavelength light, the solar spectrum can be effectively separated and utilized more efficiently. Additionally, novel concepts on light management and/or improvement that are currently being developed in the field of photovoltaic and photoelectrolysis (e.g. multiple exciton generation,<sup>45,46</sup> space-separated quantum cutting,<sup>47</sup> down- and up-conversion<sup>48-50</sup>) may have a potential of application in the hybrid photoelectrode. Special attention should be placed on up-conversion techniques, although the reported efficiencies of such processes are currently very low.<sup>51</sup> Should any efficiency breakthrough be achieved, an up-conversion layer can be inserted at the bottom of the PV cell to convert the unabsorbed longer wavelength into shorter wavelength photons (Fig. 6.9d). Finally, it should be noted that any efficiency increase through the introduction of additional materials or components for better light management should outweigh the disadvantages of increasing complexity and cost in the resulting hybrid photoelectrode.

Moreover, chemical engineering challenges remain to be solved for the application of the hybrid photoelectrodes as practical solar water splitting modules. The architecture shown in Fig. 6.1b (also called the ‘artificial leaf’ configuration) presents an ideal case where H<sub>2</sub> and O<sub>2</sub> are evolved from opposite sides, enabling relatively straightforward gas separation. This configuration is, however, proven to give a detrimental effect to the overall device efficiency due to proton transport limitations in the electrolyte. Reece et al. showed that their STH efficiency decreased from 4.7% to 2.5% when changing the cell configuration from two electrodes facing each other

(wired) to an ‘artificial leaf’ configuration (wireless).<sup>15</sup> Recently, Newman performed a quantitative modeling study based on Ohm’s law, comparing these two configurations.<sup>52</sup> He concluded that, within the same geometry, the potential drop in the wireless configuration is 6 orders of magnitude higher than the wired configuration. This is mainly caused by the much lower ionic conductivity of the electrolyte as compared to the electronic conductivity of electrical wires. To solve this problem, more advanced architectures such as a ‘nanostructured artificial leaf’ with the introduction of proton conducting membrane at the hybrid photoelectrode’s interface have been proposed by Lewis et al. among others.<sup>53, 54</sup> However, it is still not clear whether the added complexity is needed and can be justified with enhancement in efficiency, since the fabrication of such architecture is very challenging and currently very expensive making it impractical for large scale integration.

## 6.6 Conclusions

In summary, we have proposed that among the several tandem device architectures used for solar water splitting, the hybrid photoelectrode configuration—a combination of photoelectrode and PV—is the most viable option towards achieving highly-efficient unassisted solar water splitting. Currently, ~5% STH efficiency, which is half of the 10% efficiency target, has been achieved using this configuration with stable, cheap, and earth abundant materials. A design rule for the hybrid photoelectrode towards achieving this efficiency target has been discussed from the photoelectrode, PV cell, and device point of view. A lower onset potential and higher slope of the J-V curve are expected for the optimum photoanode. The first requirement can be achieved by exploiting materials with conduction band energy level as high as possible. We show that the position of the conduction band directly determines the choice for the PV cell configuration, i.e., the number and type of junctions required. A higher slope of the J-V curve of the photoanode can be obtained by improving the catalytic and carrier separation efficiencies. We show, in the case of BiVO<sub>4</sub> photoanodes, that the deposition of a Co-Pi catalyst on its surface and the introduction of gradient tungsten dopant concentration successfully improve the catalytic and carrier separation efficiency, respectively. As a result, the slope of the J-V curve is increased. From the PV cell perspective, we show that a general optimization using the AM1.5 spectrum does not necessarily yield an optimum PV cell for hybrid photoelectrode configuration. Instead, the transmitted spectrum of the photoanode should be used for the optimization procedure. This optical inter-relation between the photoanode and the PV cell therefore requires light management to be viewed from the whole device standpoint, not just for each individual layer. Several light management techniques have been proposed to utilize the solar spectrum more efficiently, and therefore

improve the overall device efficiency. Finally, remaining challenges in term of the device architecture and chemical engineering issues have to be addressed before a practical device based on a hybrid photoelectrode can be implemented. Collaborative efforts from various disciplines—including but not limited to photoelectrochemistry, solar cells, physics and chemical engineering—are therefore essential to achieve low-cost, highly-efficient solar water splitting devices.

## 6.7 References

1. R. van de Krol, M. Grätzel, *Photoelectrochemical Hydrogen Production*, Springer **2012**.
2. International Energy Agency Report: World Energy Outlook 2012.
3. NREL website (<http://nrel.gov>).
4. Styring, S. Artificial photosynthesis for solar fuels, *Faraday Discuss.* **155**, 357-376 (2012).
5. Haije, W. & Geerlings, H. Efficient Production of Solar Fuel Using Existing Large Scale Production Technologies, *Environ. Sci. Technol.* **45**, 8609-8610 (2011).
6. James, B. D. et al. Technoeconomic Analysis of Photoelectrochemical (PEC) Hydrogen Production, *DOE Report* (2009).
7. Keable, J. & Holcroft, B. Economic and Business Perspectives, *Photoelectrochemical Hydrogen Production*, 277-292 (2012).
8. C. A. Grimes, O. K. Varghese, S. Ranjan, *Light, Water, Hydrogen - The Solar Generation of Hydrogen by Water Photoelectrolysis*, Springer **2008**.
9. van de Krol, R., Liang, Y. Q., & Schoonman, J. Solar hydrogen production with nanostructured metal oxides, *J. Mater. Chem.* **18**, 2311-2320 (2008).
10. Chen, X. B., Shen, S. H., Guo, L. J., & Mao, S. S. Semiconductor-based Photocatalytic Hydrogen Generation, *Chem. Rev.* **110**, 6503-6570 (2010).
11. Chen, H. M. et al. Nano-architecture and material designs for water splitting photoelectrodes, *Chem. Soc. Rev.* **41**, 5654-5671 (2012).
12. Li, Z. et al. Photoelectrochemical cells for solar hydrogen production: current state of promising photoelectrodes, methods to improve their properties, and outlook, *Energy Environ. Sci.* **6**, 347-370 (2013).
13. Licht, S. Multiple band gap semiconductor/electrolyte solar energy conversion, *J. Phys. Chem. B* **105**, 6281-6294 (2001).
14. Delahoy, A. E. et al. A one-unit photovoltaic electrolysis system based on a triple stack of amorphous silicon (pin) cells, *Int. J. Hydrogen Energy* **10**, 113-116 (1985).
15. Reece, S. Y. et al. Wireless Solar Water Splitting Using Silicon-Based Semiconductors and Earth-Abundant Catalysts, *Science* **334**, 645-648 (2011).

16. Khaselev, O. & Turner, J. A. A monolithic photovoltaic-photoelectrochemical device for hydrogen production via water splitting, *Science* **280**, 425-427 (1998).
17. Brillet, J. et al. Highly efficient water splitting by a dual-absorber tandem cell, *Nat Photon* **6**, 824-828 (2012).
18. Miller, E. L., Marsen, B., Paluselli, D., & Rocheleau, R. Optimization of hybrid photoelectrodes for solar water-splitting, *Electrochem. Solid State Lett.* **8**, A247-A249 (2005).
19. N. Gaillard, Y. Chang, J. Kaneshiro, A. Deangelis, E. L. Miller, Status of Research on Tungsten Oxide-based Photoelectrochemical Devices at the University of Hawai'i, *Proc. SPIE* **7770**, 7770V1-14 (2010).
20. Rocheleau, R. E., Miller, E. L., & Misra, A. High-efficiency photoelectrochemical hydrogen production using multijunction amorphous silicon photoelectrodes, *Energy & Fuels* **12**, 3-10 (1998).
21. Yamada, Y. et al. One chip photovoltaic water electrolysis device, *Int. J. Hydrogen Energy* **28**, 1167-1169 (2003).
22. Abdi, F. F. et al. Efficient solar water splitting by enhanced charge separation in a bismuth vanadate-silicon tandem photoelectrode, *Nat. Commun.* **4**, 2195 (2013).
23. Kanan, M. W. & Nocera, D. G. In situ formation of an oxygen-evolving catalyst in neutral water containing phosphate and  $\text{Co}^{2+}$ , *Science* **321**, 1072-1075 (2008).
24. Koper, M. T. Thermodynamic theory of multi-electron transfer reactions: Implications for electrocatalysis, *J. Electroanal. Chem.* **660**, 254-260 (2011).
25. Winkler, M. T., Cox, C. R., Nocera, D. G., & Buonassisi, T. Modeling integrated photovoltaic—electrochemical devices using steady-state equivalent circuits, *Proceedings of the National Academy of Sciences* (2013).
26. Surendranath, Y., Kanan, M. W., & Nocera, D. G. Mechanistic Studies of the Oxygen Evolution Reaction by a Cobalt-Phosphate Catalyst at Neutral pH, *J. Am. Chem. Soc.* **132**, 16501-16509 (2010).
27. Paracchino, A. et al. Highly active oxide photocathode for photoelectrochemical water reduction, *Nature Mater.* **10**, 456-461 (2011).
28. Miller, E. L., Rocheleau, R. E., & Deng, X. M. Design considerations for a hybrid amorphous silicon/photoelectrochemical multijunction cell for hydrogen production, *Int. J. Hydrogen Energy* **28**, 615-623 (2003).
29. Miller, E. L., Rocheleau, R. E., & Khan, S. A hybrid multijunction photoelectrode for hydrogen production fabricated with amorphous silicon/germanium and iron oxide thin films, *Int. J. Hydrogen Energy* **29**, 907-914 (2004).
30. Tong, L. et al. Sustained solar hydrogen generation using a dye-sensitised NiO photocathode/ $\text{BiVO}_4$  tandem photo-electrochemical device, *Energy Environ. Sci.* **5**, 9472-9475 (2012).
31. Lin, C. Y., Lai, Y. H., Mersch, D., & Reisner, E.  $\text{Cu}_2\text{O}/\text{NiO}_x$  nanocomposite as an inexpensive photocathode in photoelectrochemical water splitting, *Chem. Sci.* **3**, 3482-3487 (2012).

32. Miyauchi, M., Hanayama, T., Atarashi, D., & Sakai, E. Photoenergy Conversion in p-Type  $\text{Cu}_2\text{ZnSnS}_4$  Nanorods and n-Type Metal Oxide Composites, *J. Phys. Chem. C* **116**, 23945-23950 (2012).
33. Jia, Q., Iwashina, K., & Kudo, A. Facile fabrication of an efficient  $\text{BiVO}_4$  thin film electrode for water splitting under visible light irradiation, *Proceedings of the National Academy of Sciences* **109**, 11564-11569 (2012).
34. Reichman, J. The Current-Voltage Characteristics of Semiconductor-Electrolyte Junction Photo-Voltaic Cells, *Appl. Phys. Lett.* **36**, 574-577 (1980).
35. Zhong, D. K., Choi, S., & Gamelin, D. R. Near-Complete Suppression of Surface Recombination in Solar Photoelectrolysis by "Co-Pi" Catalyst-Modified W: $\text{BiVO}_4$ , *J. Am. Chem. Soc.* **133**, 18370-18377 (2011).
36. Abdi, F. F. & van de Krol, R. Nature and Light Dependence of Bulk Recombination in Co-Pi-Catalyzed  $\text{BiVO}_4$  Photoanodes, *J. Phys. Chem. C* **116**, 9398-9404 (2012).
37. Abdi, F. F., Firet, N., & van de Krol, R. Efficient  $\text{BiVO}_4$  Thin Film Photoanodes Modified with Cobalt Phosphate Catalyst and W-doping, *ChemCatChem* **5**, 490-496 (2013).
38. Seabold, J. A. & Choi, K. S. Efficient and stable photo-oxidation of water by a bismuth vanadate photoanode coupled with an iron oxyhydroxide oxygen evolution catalyst, *J. Am. Chem. Soc.* **134**, 2186-2192 (2012).
39. K. Jager, O. Isabella, L. Zhao, M. Zeman, *Light scattering properties of surface-textured substrates*, WILEY-VCH VERLAG GMBH, WEINHEIM **2010**.
40. Battaglia, C. et al. Light Trapping in Solar Cells: Can Periodic Beat Random?, *Acs Nano* **6**, 2790-2797 (2012).
41. Thomann, I. et al. Plasmon Enhanced Solar-to-Fuel Energy Conversion, *Nano Lett.* **11**, 3440-3446 (2011).
42. Isabella, O., Solntsev, S., Caratelli, D., & Zeman, M. 3-D optical modeling of thin-film silicon solar cells on diffraction gratings, *Prog. Photovoltaics* **21**, 94-108 (2013).
43. MacDougall, M. H. et al. Wide-bandwidth distributed Bragg reflectors using oxide/GaAs multilayers, *Electron. Lett.* **30**, 1147-1149 (1994).
44. Green, M. A. & Ho-Baillie, A. Forty three per cent composite split-spectrum concentrator solar cell efficiency, *Prog. Photovoltaics* **18**, 42-47 (2010).
45. Schaller, R. D., Agranovich, V. M., & Klimov, V. I. High-efficiency carrier multiplication through direct photogeneration of multi-excitons via virtual single-exciton states, *Nature Physics* **1**, 189-194 (2005).
46. Trinh, M. T. et al. Direct generation of multiple excitons in adjacent silicon nanocrystals revealed by induced absorption, *Nature Photonics* **6**, 316-321 (2012).
47. Timmerman, D. et al. Space-separated quantum cutting with silicon nanocrystals for photovoltaic applications, *Nature Photonics* **2**, 105-109 (2008).
48. Trupke, T., Green, M. A., & Würfel, P. Improving solar cell efficiencies by up-conversion of sub-band-gap light, *J. Appl. Phys.* **92**, 4117-4122 (2002).

49. Trupke, T., Green, M. A., & Würfel, P. Improving solar cell efficiencies by down-conversion of high-energy photons, *J. Appl. Phys.* **92**, 1668-1674 (2002).
50. Badescu, V. & Badescu, A. M. Improved model for solar cells with up-conversion of low-energy photons, *Renewable Energy* **34**, 1538-1544 (2009).
51. Zhang, M. et al. Improving Hematite's Solar Water Splitting Efficiency by Incorporating Rare-Earth Upconversion Nanomaterials, *J. Phys. Chem. Lett.* **3**, 3188-3192 (2012).
52. Newman, J. Scaling with Ohm's Law; Wired vs. Wireless Photoelectrochemical Cells, *J. Electrochem. Soc.* **160**, F309-F311 (2013).
53. Dahl, S. & Chorkendorff, I. SOLAR-FUEL GENERATION Towards practical implementation, *Nature Mater.* **11**, 100-101 (2012).
54. Warren, E. L. et al. Hydrogen-evolution characteristics of Ni-Mo-coated, radial junction, n<sup>+</sup>p-silicon microwire array photocathodes, *Energy Environ. Sci.* **5**, 9653-9661 (2012).

## Appendix A

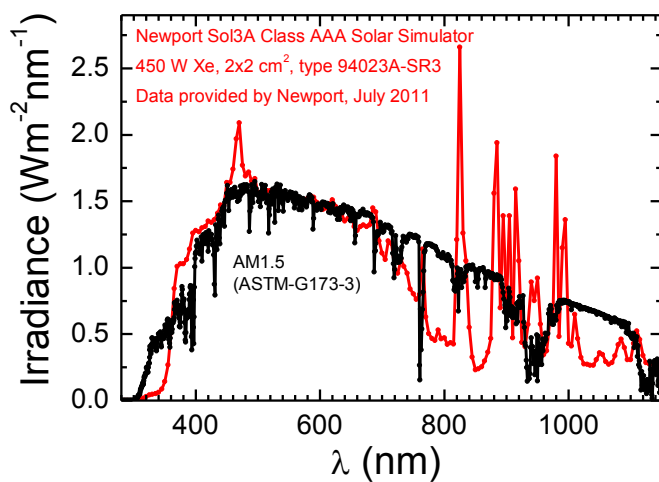


**Figure A1.** Spectral irradiance of the solar simulator used as a function of wavelength, as compared to the standard AM1.5 irradiance.



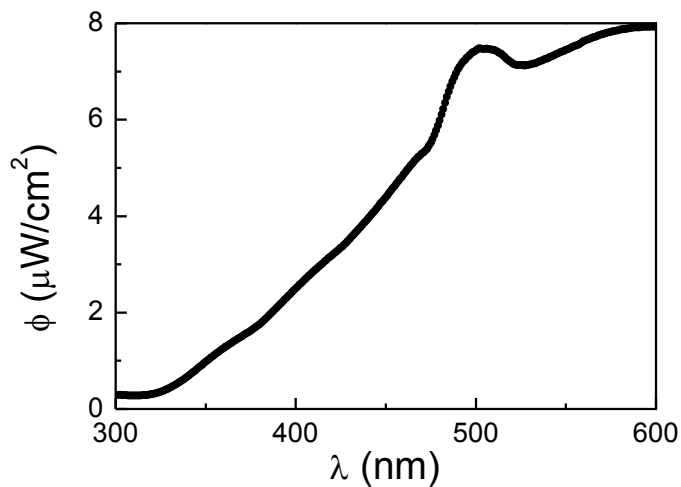


**Figure A2.** Light intensity for the IPCE measurements measured with a calibrated photodiode.

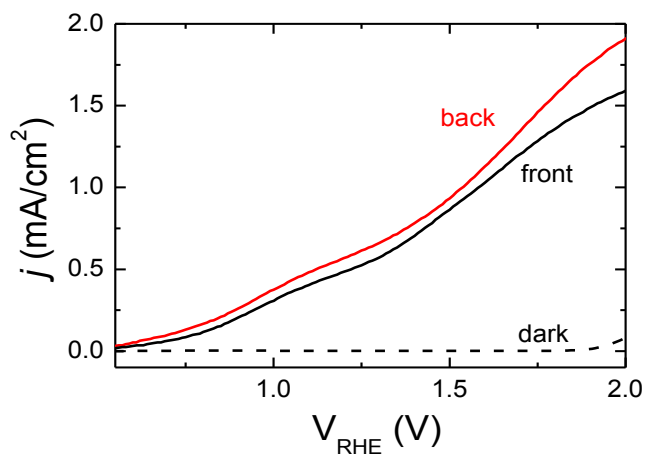


**Figure A3.** AM1.5 photocurrent density vs. voltage for 100 nm uncatalyzed  $\text{BiVO}_4$  photoelectrode under back and front illumination. The dashed line indicates the dark spectrum of the same sample.

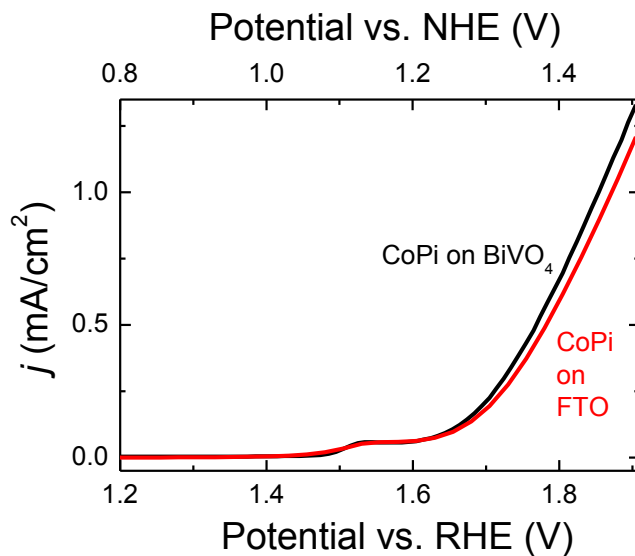


**Figure A4.** Current voltage characteristic of BiVO<sub>4</sub> (black) and FTO (red) in a 0.5 mM Co(NO<sub>3</sub>)<sub>2</sub> + 0.1 M KPi electrolyte. The hump starting at ~1.5 V<sub>RHE</sub> (~1.1 V<sub>NHE</sub>) indicates Co-Pi electrodeposition.

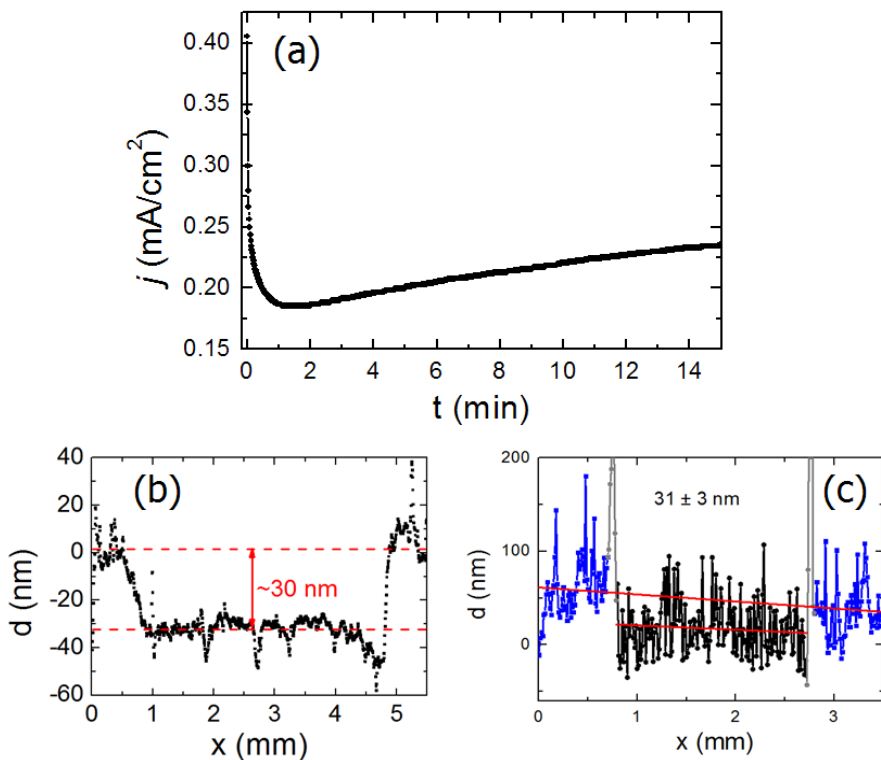


**Figure A5.** (a) Current vs. time plot of Co-Pi electrodeposition on BiVO<sub>4</sub> photoelectrode at 1.3 V<sub>NHE</sub> (=1.7 V<sub>RHE</sub>). The bottom graphs show step profile measurements of a Co-Pi film on FTO (b) and on BiVO<sub>4</sub> (c), both deposited at 1.3 V<sub>NHE</sub> for 15 min. The red lines for the BiVO<sub>4</sub> data represent linear fits of the black and blue datapoints.

## Appendix B

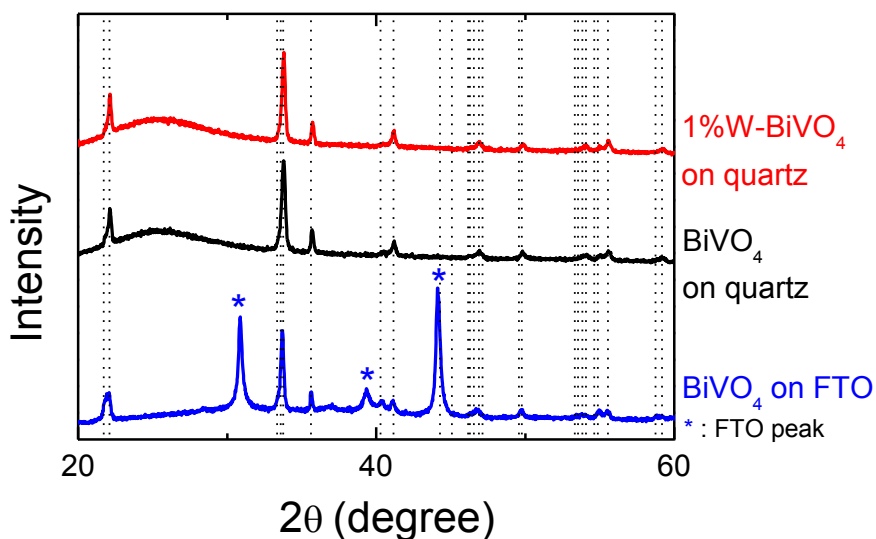


**Figure B1.** X-ray diffraction spectra for undoped BiVO<sub>4</sub> thin films on fluorine-doped tin oxide (FTO), undoped and 1% W-doped BiVO<sub>4</sub> on quartz. The dashed vertical lines represent the location of monoclinic BiVO<sub>4</sub> peaks, and the FTO peaks are indicated with star (\*).

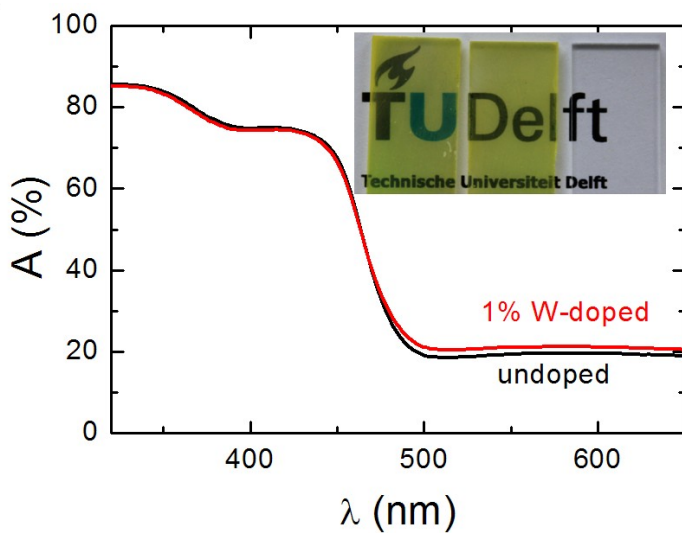


**Figure B2.** Optical absorption of undoped and 1% W-doped  $\text{BiVO}_4$  on quartz. Inset shows the photographs of (left to right) undoped  $\text{BiVO}_4$  on quartz, 1% W-doped  $\text{BiVO}_4$  on quartz, and blank quartz substrate.

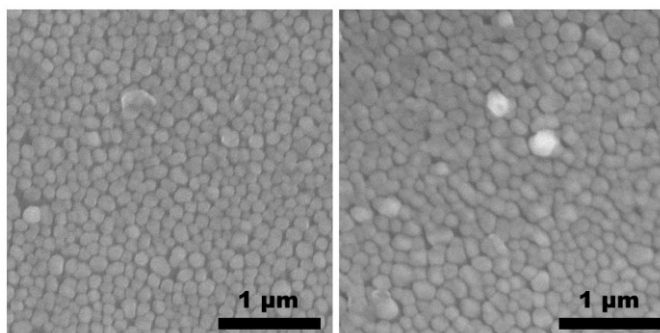


**Figure B3.** Scanning electron micrographs of undoped and 1% W-doped  $\text{BiVO}_4$  on quartz.

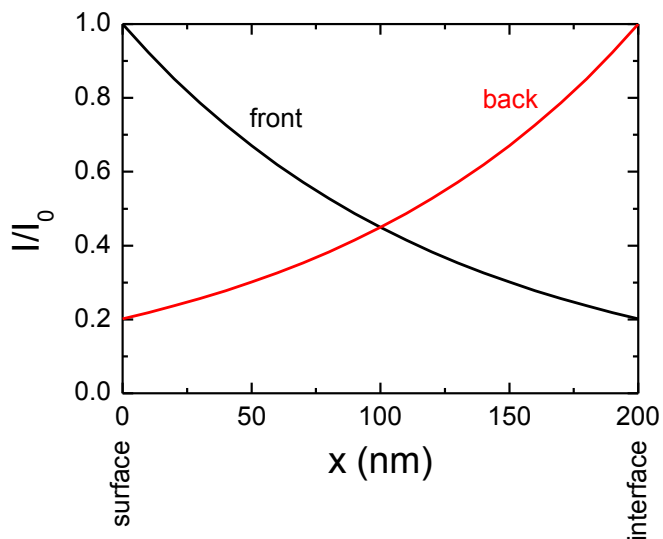


**Figure B4.** Absorption profile ( $\lambda = 300$  nm) in  $\text{BiVO}_4$  as a function of location within the film under front- and back-side illumination, calculated based on the reported absorption coefficient of  $\text{BiVO}_4$  (Zhao, Z. Y. et al., *Phys. Chem. Chem. Phys.* 13 **2011** 4746).

## Appendix C

### Definition of efficiency terms: IPCE, APCE and $\eta_{sep}$

The incident photon-to-current efficiency (*IPCE*, also called external quantum efficiency, or *EQE*) describes the amount of photocurrent collected per incident photon flux.

$$IPCE = EQE = \frac{\text{electrons} / \text{cm}^2 / \text{s}}{\text{photons} / \text{cm}^2 / \text{s}} \quad (\text{C1})$$

The absorbed photon-to-current efficiency (*APCE*, also called the internal quantum efficiency, or *IQE*) is defined as the *IPCE* which is normalized to the amount of absorbed photons within the material.

$$APCE = \frac{IPCE}{\eta_{abs}} \quad (\text{C2})$$

where  $\eta_{abs}$  is the number of electron-hole pairs generated per incident photon (absorptance). The *APCE* can also be defined as the product of the charge separation efficiency,  $\eta_{sep}$ , and the catalytic efficiency,  $\eta_{cat}$ :

$$APCE = \eta_{sep} \times \eta_{cat} \quad (\text{C3})$$

Here, the catalytic efficiency of the material is defined as the fraction of the photo-generated holes which, after arriving at the surface, successfully participate in the water oxidation reaction.

### **Band bending in the homojunction**

The amount of band bending at the interface of the homojunction is given by the following equation,

$$\Delta E = E_{f,W:BiVO_4} - E_{f,BiVO_4} = kT \ln \left( \frac{N_{D,W:BiVO_4}}{N_{D,BiVO_4}} \right) \quad (C4)$$

where  $E_{f,W:BiVO_4}$  and  $E_{f,BiVO_4}$  are the Fermi energy levels of W-doped and undoped  $BiVO_4$ , respectively,  $k$  is Boltzmann's constant,  $T$  is the temperature, and  $N_{D,W:BiVO_4}$  and  $N_{D,BiVO_4}$  are the donor densities of W-doped and undoped  $BiVO_4$ , respectively.

Based on previously reported donor densities for undoped and W-doped  $BiVO_4$ ,<sup>1-3</sup> we estimate that the donor density in W-doped  $BiVO_4$  is 10-100 times higher than that in undoped  $BiVO_4$ . From equation C4, this leads to a potential drop at the interface of the homojunction of ~60-120 mV, which is consistent with the observed change in open circuit potential upon illumination ( $\Delta OCP$ ) as shown in Fig. C2. The average thermal energy of the electrons ( $\sim kT$ ) is sufficient to overcome a barrier of 60-70 mV, which explains the somewhat modest decrease of the carrier separation for the reverse homojunction in Fig. 5.3.



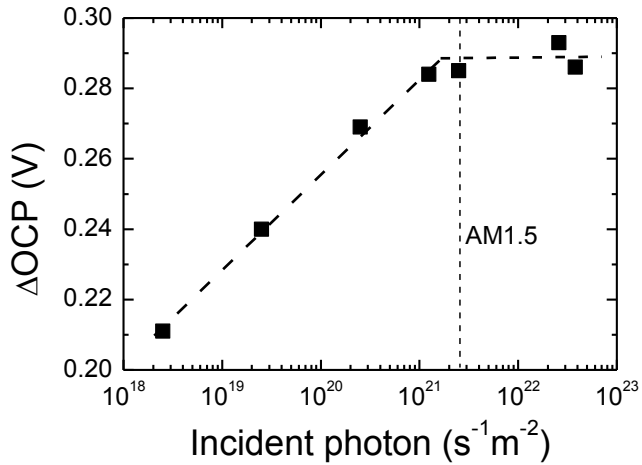


**Figure C1.** Change in open circuit potential ( $\Delta\text{OCP}$ ) of 1% W-doped  $\text{BiVO}_4$  photoanode upon illumination with different light intensities. Above an incident photon flux of  $\sim 10^{21} \text{ s}^{-1}\text{m}^{-2}$ ,  $\Delta\text{OCP}$  remains constant, indicating that the energy bands of  $\text{BiVO}_4$  completely flatten. The vertical dashed line indicates the intensity corresponding to AM1.5 sunlight. The thickness of the  $\text{BiVO}_4$  film is  $\sim 200 \text{ nm}$ .

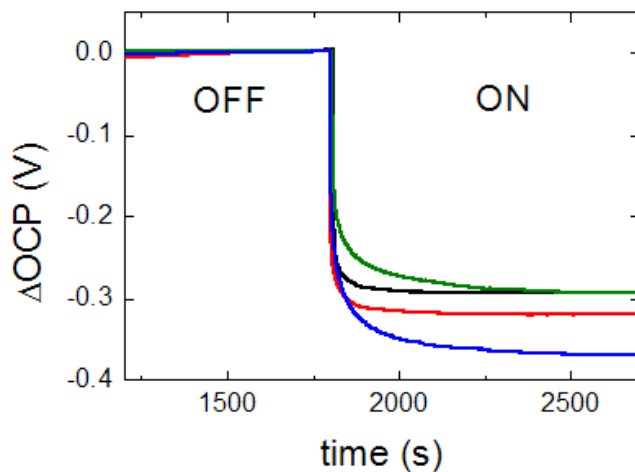


**Figure C2.** Change in open circuit potential under dark (OFF) and AM1.5 illumination (ON) of 1% W-doped BiVO<sub>4</sub> (black), W:BiVO<sub>4</sub> homojunction (red), W:BiVO<sub>4</sub> reverse homojunction (green), and gradient-doped W:BiVO<sub>4</sub> (blue).

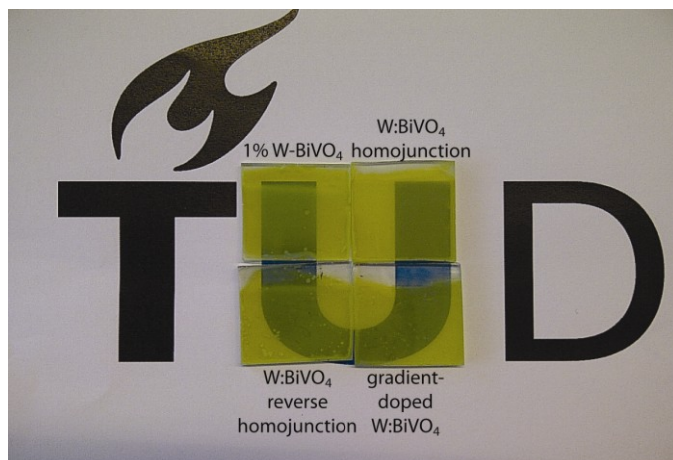


**Figure C3.** Photographs of the 200 nm-thick BiVO<sub>4</sub> photoanode samples.

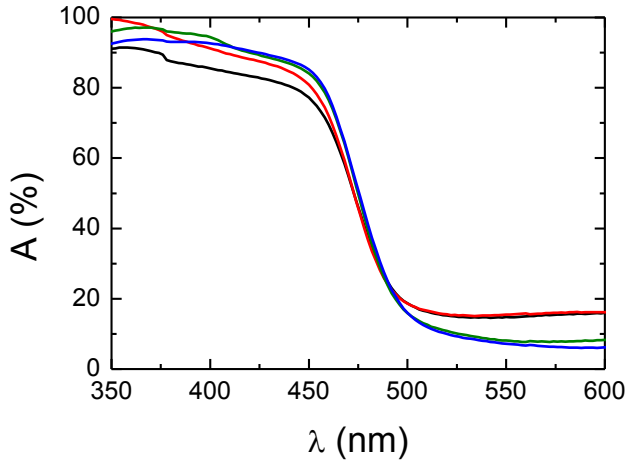


**Figure C4.** Optical absorption of 200 nm-thick 1% W-doped BiVO<sub>4</sub> (black), W:BiVO<sub>4</sub> homojunction (red), W:BiVO<sub>4</sub> reverse homojunction (green), and gradient-doped W:BiVO<sub>4</sub> (blue).

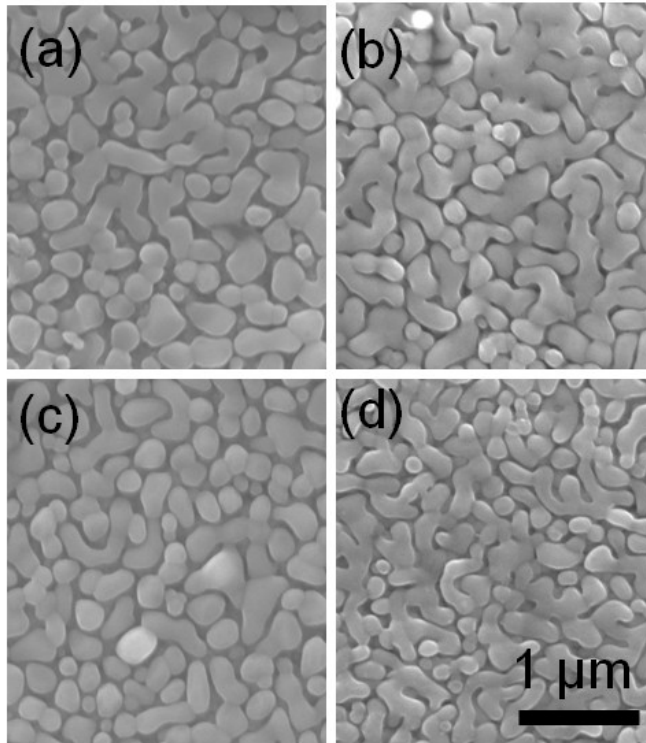


**Figure C5.** Scanning electron micrographs of 1% W-doped  $\text{BiVO}_4$  (a),  $\text{W:BiVO}_4$  homojunction (b),  $\text{W:BiVO}_4$  reverse homojunction (c), and gradient-doped  $\text{W:BiVO}_4$  (d).

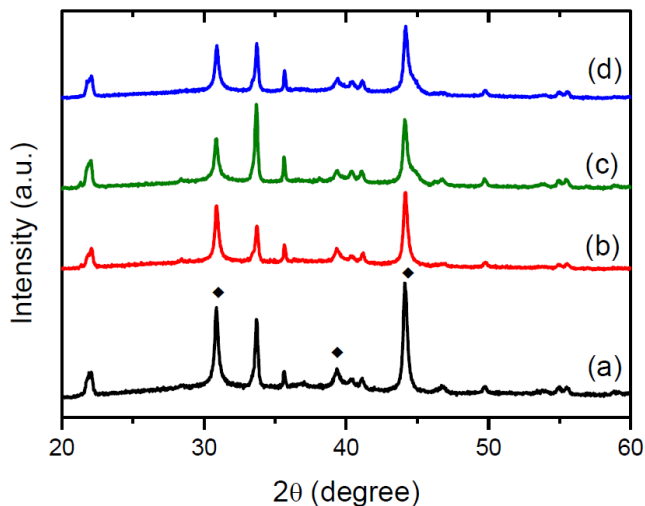


**Figure C6.** X-ray diffractogram (Bragg-Brentano geometry, Co  $K\alpha$  source) of 1% W-doped  $\text{BiVO}_4$  (a),  $\text{W}:\text{BiVO}_4$  homojunction (b),  $\text{W}:\text{BiVO}_4$  reverse homojunction (c), and gradient-doped  $\text{W}:\text{BiVO}_4$  (d). FTO substrate peaks are indicated by  $\blacklozenge$ .

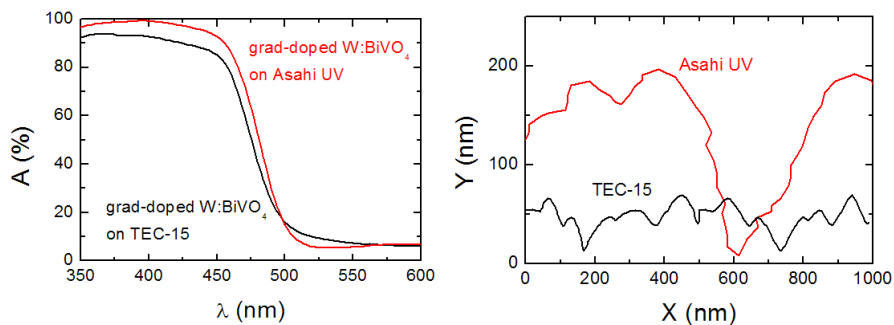


**Figure C7.** (a) Optical absorption of 200 nm-thick gradient-doped  $\text{W}:\text{BiVO}_4$  on TEC-15 (black) and the more highly textured Asahi UV conducting glass (red). (b) Surface profile of TEC-15 (black) and Asahi UV substrate (red).

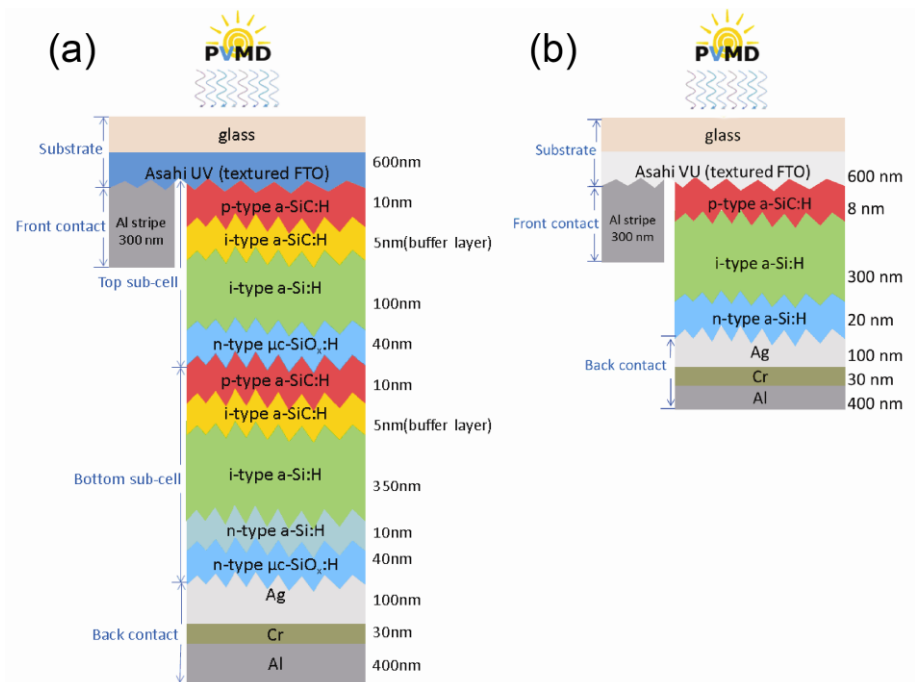


**Figure C8.** The structure of (a) the 2-jn a-Si and (b) the 1-jn a-Si solar cell used in Chapter 5. The thickness of each layer is indicated (drawing is not to scale).

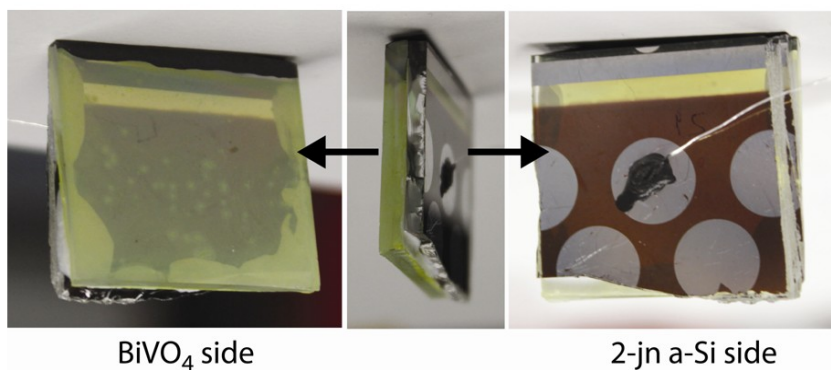


**Figure C9.** The photograph of the hybrid photoelectrode device consisting of gradient-doped W:BiVO<sub>4</sub> photoanode and 2-jn a-Si solar cell.

### **Two-electrode and three-electrode J-V curves comparison**

The J-V curves of the  $\text{BiVO}_4$  photoanode in the three-electrode measurement of Fig. 5.4 and the two-electrode measurement of Fig. 5.6a are different; Fig. 5.4 shows a more positive onset potential and lower photocurrents at potentials below  $\sim 0.7$  V vs RHE. These differences arise from the different nature of the measurement. In a three-electrode measurement, the potential of the working electrode (WE) is measured with respect to that of a reference electrode (RE), which has a fixed potential. This is, however, not the case in a two-electrode measurement. In this case, the WE potential is measured against the potential of a platinum counter electrode (CE). The CE potential is not constant, but a function of the current density (overpotential) and the local pH and concentration of dissolved  $\text{H}_2$  gas (Nernst potential). At low current densities, the equilibrium partial pressure of dissolved  $\text{H}_2$  gas will (initially) be rather low, which causes the Nernst potential of the CE to be more positive than 0 V vs. RHE. Hence,  $(V_{\text{WE}}-V_{\text{CE}})$  is more negative than  $(V_{\text{WE}}-V_{\text{RE}})$  under otherwise identical conditions. This is illustrated in Fig. C10a for an uncatalyzed  $\text{BiVO}_4$  photoanode. Since the potential difference between both curves is much larger than the typical overpotential observed for  $\text{H}_2$  evolution on Pt ( $<0.1$  V), most of it is attributed to a shift in the Nernst potential. To confirm this, a constant photocurrent density of  $\sim 0.35$   $\text{mA}/\text{cm}^2$  was passed through the sample while measuring the two-electrode and three-electrode potentials. As shown in Fig. C10b, the two-electrode potential slowly shifts towards the three-electrode potential level. After  $\sim 18$  minutes (without stirring) the difference between the curves no longer changes, indicating that the concentration of dissolved  $\text{H}_2$  no longer increases. The remaining  $\sim 50$  mV difference is due to the overpotential for  $\text{H}_2$  evolution at the platinum CE.

This overpotential is also the main reason for the slightly higher photocurrents in Fig. 5.6 (two-electrode) compared to those in Fig. 5.4 (three-electrode) at potentials positive of 1 Volt. At these high current densities, the electrolyte solution quickly saturates with  $\text{H}_2$  gas so that Nernst potential differences can be neglected.

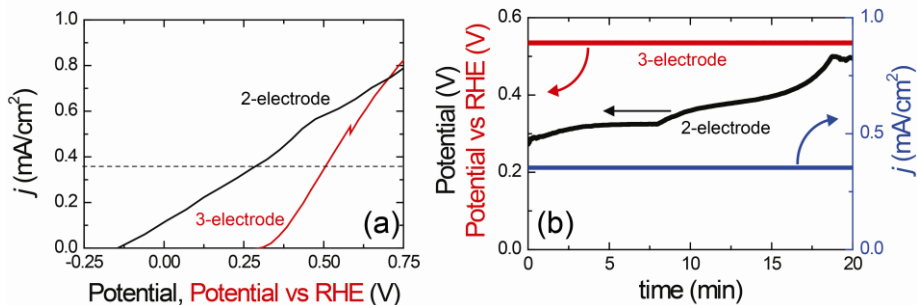


**Figure C10.** (a) AM1.5 photocurrent vs voltage (J-V) curve of an uncatalyzed gradient-doped BiVO<sub>4</sub> photoanode in a two-electrode (black) and three-electrode (red) measurement configuration. Both measurements were recorded simultaneously using a conventional three-electrode configuration, with an auxiliary high-impedance voltmeter ( $> 10 \text{ G}\Omega$ ) connected to the working and counter electrodes to measure the two-electrode J-V curve. The horizontal dashed line indicates the current level used for the galvanostatic measurement shown in (b). This graph shows the difference between the two-electrode (black) and three-electrode (red) potential as a function of time when a constant current density of  $\sim 0.35 \text{ mA/cm}^2$  (blue) is passed through the system. It takes  $\sim 18$  minutes before the two-electrode potential approaches the three-electrode potential, which is the time it takes for the solution to become saturated with dissolved H<sub>2</sub> gas.

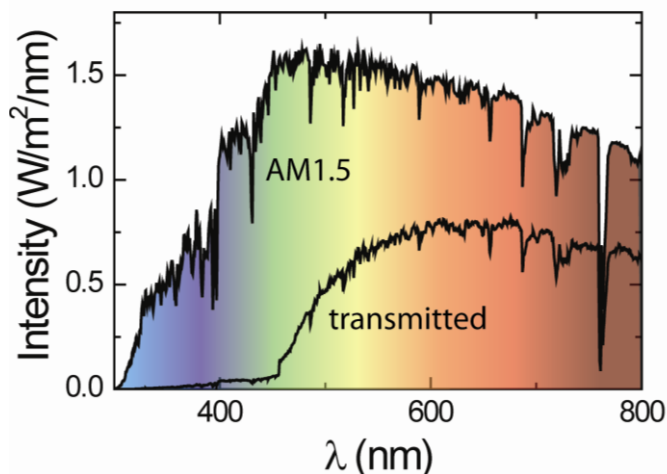


**Figure C11.** AM1.5 spectrum and the measured fraction of the light that reaches the 2-jn a-Si cell *via* transmission through the BiVO<sub>4</sub> photoanode as shown in Fig. 5.5.



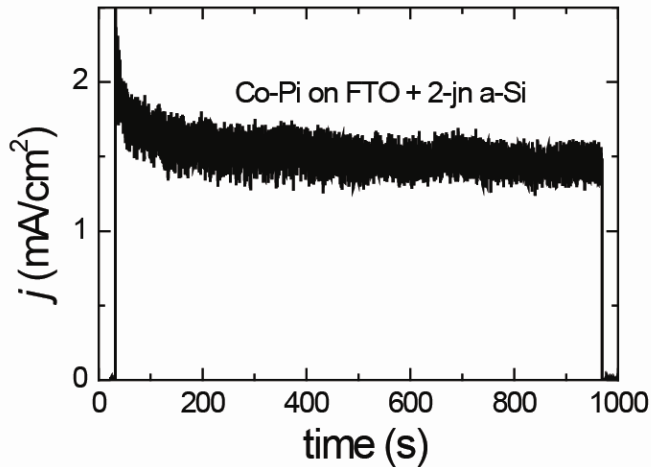


**Figure C12.** Short-circuit current vs time for the Co-Pi-coated FTO/2-jn a-Si device under AM1.5 illumination.

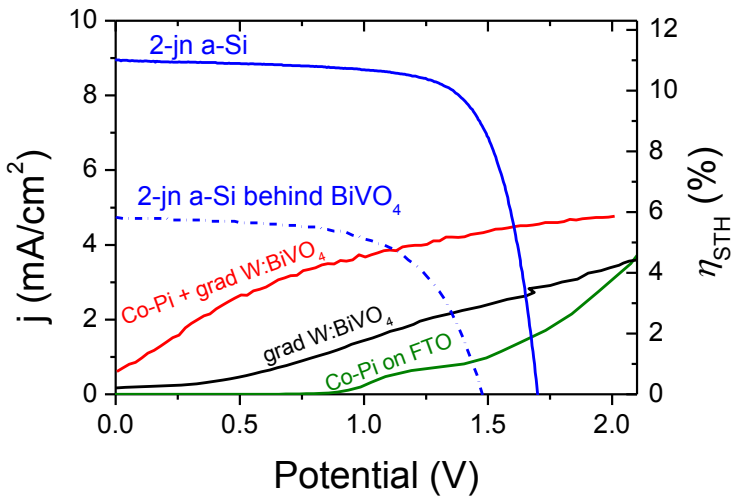


**Figure C13.** Two-electrode AM1.5 J-V curve of uncatalyzed gradient-doped W:BiVO<sub>4</sub> (black), Co-Pi catalyzed gradient-doped W:BiVO<sub>4</sub> (red), and Co-Pi on FTO substrate (green). Also shown are the J-V curves of the double-junction a-Si solar cell (blue, solid) and that of the same solar cell placed behind the BiVO<sub>4</sub> photoanode (blue, dashed).

## Summary

Climate change has been widely recognized as a major environmental problem facing the world today. The extent of the problem is also associated with economic, geopolitical and societal aspects; WHO estimates 150,000 deaths per year are caused by climate change. According to IPCC, this is related to the increase in greenhouse gas concentrations, mainly as a result of the combustion of fossil-fuels. To reconcile this, a transition from fossil-fuels to renewable-based energy sources is therefore imperative and unavoidable.

Solar water splitting has attracted significant attention to convert the abundant solar energy to chemical energy. It uses a semiconductor to convert sunlight into electron-hole pairs, which then split water into hydrogen and oxygen. To achieve a high efficiency, the semiconductor needs to fulfill several requirements, such as high absorption, efficient charge transport, high catalytic activity, good stability in aqueous solution, and low cost. It is difficult to meet all these requirements in a single material; the search for the ideal semiconductor for solar water splitting remains a challenge for many researchers.

At the beginning of the present thesis research, we therefore searched for this ideal semiconductor. We specifically limit ourselves to metal oxides, since they are generally stable in water and cheap. One of the metal oxides is bismuth vanadate ( $\text{BiVO}_4$ ), which is present in our daily life as a yellow pigment in printing ink. We chose this material because its reported photocatalytic activities, although modest, were promising. However, prior to the start of our work, there was only a limited understanding on the factors that affect its photoelectrochemical (PEC) performance.

We prepared thin film  $\text{BiVO}_4$  photoanodes with a simple spray deposition technique. Upon optimization of the deposition parameters, a high-quality thin film  $\text{BiVO}_4$  photoanode was obtained, showing an internal quantum efficiency of close to 100% under low light intensities (few  $\mu\text{W}/\text{cm}^2$ ). This high level of performance, however, could not be extrapolated to the high intensity condition of 1 sun. The photocurrent greatly diminishes as light intensity increases.

To understand this, we performed a thorough analysis to our spray-deposited BiVO<sub>4</sub> photoanode thin films. By the introduction of hydrogen peroxide (H<sub>2</sub>O<sub>2</sub>) as a hole scavenger in the electrolyte, we discovered that the performance of BiVO<sub>4</sub> at high intensities is limited by a poor catalytic activity towards the water oxidation reaction occurring at its surface. To solve this, we electrodeposited a thin layer of cobalt phosphate (Co-Pi) on the surface of BiVO<sub>4</sub>, which improved the photocurrent by a factor of ~3. This improvement is attributed to the increase of the catalytic efficiency to close to ~100%. This means that no further significant increase in performance can be expected from an improvement in the catalytic processes.

As soon as the catalytic limitation is removed, poor electron transport starts becoming the limiting factor in BiVO<sub>4</sub>. This is reflected by the lower photocurrents under front-side illumination as compared to the back-side illumination, as well as the poor charge separation efficiency. Tungsten (W) was then introduced as a donor-type dopant to replace vanadium (V). As a result, the carrier concentration, as well as the conductivity, in the doped BiVO<sub>4</sub> sample was improved. However, the improvement in the charge separation efficiency and the PEC performance remained modest. We investigated the origin of this limitation by time-resolved microwave conductivity (TRMC) measurements. Based on these measurements, we found that a further improvement of efficiency is prevented due to the low intrinsic carrier mobility in BiVO<sub>4</sub>.

To overcome this poor charge separation, we introduced a simple and elegant strategy, taking advantage of the difference between the properties of doped and undoped BiVO<sub>4</sub>. Due to the difference in their Fermi levels, combining doped and undoped BiVO<sub>4</sub> to form a homojunction could extend the internal electric field to the bulk of the photoanode. This electric field is, of course, very beneficial towards charge separation in a semiconductor. Using this concept, an n<sup>+</sup>-n homojunction based on a gradient W concentration profile was shown to improve the charge separation efficiency significantly, up to ~80%. As a result, a record AM1.5 photocurrent of 3.6 mA/cm<sup>2</sup> at 1.23 V vs RHE was demonstrated, which is more than 20-fold improvement of performance as compared to the photocurrent achieved with BiVO<sub>4</sub> before the start of this thesis work. This achievement also firmly establishes BiVO<sub>4</sub> as the new champion photoanode material in the class of metal oxides, ahead of the already more established tungsten trioxide (WO<sub>3</sub>) and hematite (Fe<sub>2</sub>O<sub>3</sub>).

A hybrid photoelectrode based on this record BiVO<sub>4</sub>-based photoanode and an amorphous silicon solar cell was fabricated to avoid the need for an externally applied bias potential. In this configuration, the short wavelength part of the solar spectrum is absorbed by the BiVO<sub>4</sub>, and the long wavelength part of the solar spectrum is transmitted and absorbed by the solar cell. Solar-to-hydrogen (STH) efficiencies of 3.6% and 4.9% were achieved for the device based on single junction and double junction amorphous silicon solar cell, respectively. This efficiency is the highest

efficiency ever achieved for a hybrid photoelectrode based on a metal oxide photoelectrode.

Finally, we provided a perspective on different PEC water splitting device architectures. The hybrid photoelectrode concept is shown to be superior to other designs, in terms of the prospect for highly-efficient, low-cost water splitting device. To achieve this, the development of materials for PEC water splitting must be continued, and this thesis could act as a guideline. Considering that the four-year effort in this thesis has resulted in a 20-fold performance improvement and a STH efficiency of ~5%, we believe that the ideal semiconductor material for PEC water splitting, which is cheap, abundant, stable, and showing the 10% efficiency target, could be developed within the next few years.

## Samenvatting

Klimaatverandering wordt tegenwoordig op grote schaal erkend als een mondiaal milieuprobleem. Het probleem kent economische, geopolitieke en sociale aspecten; de WHO schat dat er jaarlijks 150.000 mensen sterven aan de gevolgen van klimaatverandering. Volgens het IPCC is dit probleem gerelateerd aan een verhoogde concentratie broeikasgassen die vooral wordt veroorzaakt door de verbranding van fossiele brandstoffen. Om het probleem op te lossen is een transitie van fossiele naar hernieuwbare energiebronnen noodzakelijk en onvermijdelijk.

Watersplitsing met behulp van zonlicht is een zeer interessante manier om de overvloedige aanwezige zonne-energie om te zetten naar chemische energie. Een halfgeleider wordt gebruikt om zonlicht om te zetten naar elektron-gat paren, welke vervolgens water splitsen in waterstof en zuurstof. Om een hoge efficiëntie te verkrijgen moet de halfgeleider aan een aantal eisen voldoen, zoals hoge licht absorptie, efficiënt ladingstransport, hoge katalytische activiteit, een goede stabiliteit in waterige oplossing en lage kosten. Het is moeilijk om al deze eisen in éénmateriaal te vinden; de zoektocht naar de ideale halfgeleider voor fotokatalytische watersplitsing blijft een uitdaging voor vele wetenschappers.

Het begin van het onderzoek voor dit proefschrift bestond daarom uit een zoektocht naar deze ideale halfgeleider. We hebben onszelf specifiek beperkt tot metaal oxides, aangezien deze over het algemeen stabiel in water en goedkoop zijn. Een van de metaal oxides is bismuth vanadaat ( $\text{BiVO}_4$ ), een materiaal dat in het dagelijks leven wordt gebruikt als een geel pigment in printer inkt. Wij hebben voor dit materiaal gekozen omdat de gepubliceerde fotokatalytische activiteiten bescheiden doch veelbelovend waren. Niettemin waren de factoren die de fotoelektrochemische (PEC) prestaties van  $\text{BiVO}_4$  beïnvloeden nog grotendeels onbekend voor aanvang van dit onderzoek.

Wij hebben dunne-film fotoanodes van  $\text{BiVO}_4$  geprepareerd door middel van een simpele spray depositie techniek. Door het optimaliseren van de depositieparameters kon een dunne-film fotoanode van hoge kwaliteit worden gemaakt met een interne kwantum efficiëntie van bijna 100% onder lage lichtintensiteiten (enkele  $\mu\text{W}/\text{cm}^2$ ). Dit hoge prestatieniveau kon echter niet worden geëxtrapoleerd naar de hoge

lichtintensiteit van 1 zon. De fotostroom vermindert enorm wanneer de lichtintensiteit wordt vergroot.

Om dit te begrijpen hebben we onze  $\text{BiVO}_4$  fotoanode aan een grondige analyse onderworpen. Door de introductie van waterstofperoxide ( $\text{H}_2\text{O}_2$ ) als gatenvanger in het elektrolyet ontdekten we dat de prestaties van  $\text{BiVO}_4$  bij hoge lichtintensiteit worden gelimiteerd. Dit wordt veroorzaakt door slechte katalytische eigenschappen voor de wateroxidatie reactie aan het oppervlak van  $\text{BiVO}_4$ . Om dit probleem op te lossen hebben we met elektrodepositie een dunne film van kobaltfosfaat (Co-Pi) op het oppervlak van de  $\text{BiVO}_4$  aangebracht. De Co-Pi verbeterde de fotostroom met een factor  $\sim 3$ . Deze verbetering wordt toegeschreven aan de verhoging van de katalytische efficiëntie naar bijna 100%. Dit betekent dat verdere verbetering van deze katalytische processen geen verdere toename van de prestaties van  $\text{BiVO}_4$  zal opleveren.

Zodra de katalytische limitatie is weggenomen, begint slecht elektrontransport een beperking voor  $\text{BiVO}_4$  te vormen. Dit is te zien aan de lagere fotostroom onder belichting van de voorzijde van de fotoanode vergeleken met belichting van de achterzijde, evenals de slechte efficiëntie voor het scheiden van elektronen en gaten. Hierop is wolfram (W) geïntroduceerd als donor-type dotering van vanadium (V) te vervangen. De ladingdrager concentratie en de conductiviteit zijn hierdoor verbeterd. Niettemin bleven de verbeteringen in ladingsscheiding efficiëntie en de fotoelectrochemische prestaties bescheiden. We hebben de oorzaak van deze limitatie onderzocht met behulp van *time-resolved microwave conductivity* (TRMC) metingen. Gebaseerd op deze metingen vonden we dat verdere verbetering van de efficiëntie verhinderd wordt door de lage intrinsieke ladingdrager mobiliteit in  $\text{BiVO}_4$ .

Om deze slechte ladingsscheiding te ondervangen hebben we een simpele en elegante strategie toegepast, waarbij we profiteerden van het verschil in eigenschappen tussen gedoteerd en niet gedoteerd  $\text{BiVO}_4$ . Door hun verschillende Fermi niveaus kan het interne elektrische veld van  $\text{BiVO}_4$  worden doorgevoerd tot in de bulk van de fotoanode door het combineren van gedoteerd en ongedoteerd  $\text{BiVO}_4$  tot een homo-junctie. Dit elektrische veld is natuurlijk zeer bevorderlijk voor ladingsscheiding in een halfgeleider. Een  $n^+n$  homo-junctie gebaseerd op een gradiënt van de W concentratie heeft de ladingsscheiding efficiëntie verbeterd tot  $\sim 80\%$ . Het resultaat hiervan is een record AM1,5 fotostroom van  $3,6 \text{ mA/cm}^2$  bij  $1,23 \text{ V}_{\text{RHE}}$ . Dit is een meer dan 20-voudige verbetering vergeleken met de fotostroom die was bereikt met  $\text{BiVO}_4$  voor de start van dit proefschrift onderzoek. Deze prestatie kroont  $\text{BiVO}_4$  ook tot de allerbeste fotoanode in de klasse van metaal oxides, met betere resultaten dan de al langer onderzochte wolframoxide ( $\text{WO}_3$ ) en hematiet ( $\text{Fe}_2\text{O}_3$ ).

We hebben een hybride fotoelectrode gebaseerd op deze record- $\text{BiVO}_4$  fotoanode en een amorf silicium zonnecel gemaakt om geen extern spanningsbronte hoeven gebruiken. In deze configuratie worden de korte golflengtes van het zonnespectrum geabsorbeerd door het  $\text{BiVO}_4$  en de lange golflengtes worden doorgelaten en vervolgens geabsorbeerd door de zonnecel. Solar-to-hydrogen (STH) efficiënties van

3,6% en 4,9% werden behaald voor dit apparaat gebaseerd op respectievelijk een enkele en een dubbele junctie amorf silicium zonnecel. Deze efficiëntie is tevens de hoogste efficiëntie ooit gehaald met een hybride fotoelectrode gebaseerd op metaal oxides.

Tenslotte hebben we ons beziggehouden met verschillende configuraties van PEC watersplitsende apparaten. De hybride fotoelectrode is superieur aan andere ontwerpen wanneer we kijken naar zeer efficiënte, goedkope watersplitsende apparaten. Om tot de productie van dergelijke apparaten te komen moet de ontwikkeling van materialen voor PEC watersplitsing worden voortgezet, waarbij dit proefschrift als gids kan dienen. Aangezien dit proefschrift over een periode van 4 jaar heeft geleid tot een 20-voudige verbetering en een STH efficiëntie van ~5%, geloven wij dat een materiaal dat goedkoop, overvloedig aanwezig, stabiel en met een efficiëntie van tenminste 10% de komende jaren ontwikkeld moet kunnen worden.

## List of Publications

1. F. F. Abdi and R. van de Krol  
Nature and Light Dependence of Bulk Recombination in Co-Pi-Catalyzed BiVO<sub>4</sub> Photoanodes  
*The Journal of Physical Chemistry C*, **116**, 9398 (2012)
2. F. F. Abdi, N. Firet, A. Dabirian and R. van de Krol  
Spray-deposited Co-Pi Catalyzed BiVO<sub>4</sub>: a low-cost route towards highly efficient photoanodes  
*Materials Research Society Symposium Proceedings*, **1446** (2012)
3. S. Emin, M. Fanetti, F. F. Abdi, D. Lisjak, M. Valant, R. van de Krol and B. Dam  
Photoelectrochemical Properties of Cadmium Chalcogenide-Sensitized Textured Porous Zinc Oxide Plate Electrodes  
*ACS Applied Materials and Interfaces*, **5**, 1113 (2013)
4. F. F. Abdi, N. Firet and R. van de Krol  
Efficient BiVO<sub>4</sub> Thin Film Photoanodes Modified with Cobalt Phosphate Catalyst and W-doping  
*ChemCatChem*, **5**, 490 (2013)
5. F. F. Abdi, L. Han, A. H. M. Smets, M. Zeman, B. Dam and R. van de Krol  
Efficient Solar Water Splitting by Enhanced Charge Separation in a Bismuth Vanadate-Silicon Tandem Photoelectrode  
*Nature Communications*, **4**, 2195 (2013)
6. L. Han, F. F. Abdi, B. Dam, R. van de Krol, A. H. M. Smets, and M. Zeman  
A Hybrid Photoelectrochemical Water Splitting Configuration Based on Bismuth Vanadate Photoanode with Improved Light Trapping Technique and Thin Film Silicon Solar Cells  
*28th European Photovoltaic Solar Energy Conference and Exhibition (EU PVSEC) Proceedings* (2013)



7. F. F. Abdi, T. J. Savenije, M. M. May, B. Dam and R. van de Krol  
The Origin of Slow Carrier Transport in BiVO<sub>4</sub>: a time-resolved microwave conductivity study  
*The Journal of Physical Chemistry Letters*, accepted, DOI: 10.1021/jz4013257
8. L. Han, P. P. Rodriguez, F. F. Abdi, B. Dam, R. van de Krol, A. H. M. Smets and M. Zeman  
Double-Junction Amorphous Silicon Solar Cell Optimization for Photoelectrochemical Water Splitting Device Based on BiVO<sub>4</sub> Homojunction Photoanode  
*In preparation*
9. F. F. Abdi, L. Han, W. A. Smith, A. H. M. Smets, M. Zeman, B. Dam and R. van de Krol  
Design Rules for Hybrid Photoelectrode for Water Splitting  
*In preparation*
10. B. Trzesniewski, F. F. Abdi, B. Dam, and W. A. Smith  
Comparing the Catalytic Mechanisms of Cobalt- and Nickel-Borate Oxygen Evolution Catalysts  
*In preparation*
11. S. Emin, F. F. Abdi, M. Fanetti, W. Peng, W. A. Smith, K. Sivula, and B. Dam  
Photoelectrochemical Studies of Textured Porous CuO Thin Films Prepared from Electrodeposited CuCl and CuBr  
*In preparation*
12. M. de Respinis, F. F. Abdi, W. A. Smith, T. J. Savenije, B. Dam, and R. van de Krol  
Oxynitrogenography: the search for oxynitrides for solar water splitting  
*In preparation*
13. J. Ravensbergen, F. F. Abdi, R. N. Frese, B. Dam, R. van de Krol, and J. T. M. Kennis  
The photophysics of BiVO<sub>4</sub>, a transient absorption study  
*In preparation*
14. L. Han, I. A. Digdaya, F. F. Abdi, A. H. M. Smets, M. Zeman, B. Dam, and W. A. Smith  
Hydrogenated Amorphous Silicon Carbide Based Photoelectrochemical Device for Solar Water Splitting  
*In preparation*

## Acknowledgements

Alhamdulillahirabbil ‘alamin

“While we’re living, the dreams we have as children fade away.”

Noel Gallagher

While many of my childhood dreams—becoming a professional football player or forming a rock band—may have long gone by now, I am grateful that I do live up to one: being a scientist. The completion of this book and (hopefully) the committee’s approval of my thesis defense therefore mark a very important step in my living this dream. All of these, of course, would not be possible without the help and contribution of many people.

A big and heartfelt thank goes to my supervisors, Roel and Bernard, who have been great sources of my learning in these past four years. I will not definitely be who I am today if not for the two of you. To Roel, thanks for introducing me to this exciting field of solar water splitting, and for teaching me all the necessary skills. Thanks for all your patience to my constant annoyance; I hope it was not too much. ☺ Most of all, thanks for believing in me. I hope you enjoyed working with me as much as I did, and I look forward to more fruitful years ahead. To Bernard, thanks for creating a very comfortable and conducive atmosphere in the group. Thanks for teaching me to absorb from my environment, and at the same time spread influences. Thanks for always posing challenges for me, be it to produce high quality scientific work or to stop using the elevator. ☺ I am really thankful for the discussions and extra supports that you gave during this past year. Finally, to both Roel and Bernard, thanks for always pushing me to become better, as a scientist and a person.

Without a doubt, the contribution of all group members of MECS has been very essential in the completion of this thesis. To Joost and Herman, thanks for always patiently catering to my every needs in the lab. To Heleen, thanks for all your great

help with the administrative matters. And of course, I would like to thank all the group members of MECS: Lennard, Arjen, Yevheniy, Qingping, Qiang, Ali, Yen, Moreno, Petra, Ruud, Christiaan, Martin, Bartek, Digda, Divya, Wilson, Wim, Hans, Peter, Tsveta, Maria, Andrea, Valerio, Matteo, Tobias, my students (Christine, Jelissa, Aletta, Dubravko, Maarten, Nienke, Eli, Paula), and everyone who I can't seem to recall right now in this middle of the night. Thanks for all your contributions, either directly in some of the work in this thesis or indirectly by making my time in the lab and in Delft so enjoyable. Thanks also to Nienke, Eli, and Maarten who helped with the Dutch translation in this thesis.

I would also like to thank several people who have contributed in the four years that I worked in Delft. In ChemE: Tom, Murthy, Maria, Ruben, Marcel, Ben, Esteban; and in EWI: Arno, Lihao, Miro. Thanks for the collaboration and/or the help that you provided along the way. This thesis could not be completed without your help.

Thanks to the Indonesian community in the Netherlands, especially in Delft: Kak Nana, Mba Alia, Aki, Baqir, Jusuf, Bian, Mas Firman, Mas Popong, Giga, Mas Dwi, Pak Agung, Cak Zul, Pandu, Saputra & Pita, Rian & Anti, Bhimo, Digda, Mirza, Azzam, Pak Senot & Mba Pungky and many more members of the PPI Delft. When you're far from home, it's always a comforting feeling to know that there are other people that call the same place home; to share the same frustration of living so far away from home, as well as to help each other in getting over that home-sickness.

Special thanks to the talented Ms. Ruth Marbun (<http://iniruthmarbun.blogspot.com>), who has designed the cover artwork and the invitation for this thesis. Big fan!

Words can never be enough to express my sincerest thank to my family. Bunda: thanks for your never-ending support to whatever I chose to do in life. Your constant prayers have always been the best help that I will ever need. Abang and Firda: thanks for all your support, and for always lending your ears to all my stories. Mudah-mudahan wawa bisa membuat Bunda, Abang dan Firda bahagia.

Last, but definitely not least: my warmest thank goes to Nisa and Zahra. Nisa, thanks for being here with me, accompanying me in my every steps. Thanks for always being supportive, for sharing every moments of happiness and sadness, and for keeping up with me. Zahra, thanks for your presence in our life. Thanks for being the best distraction I could ever wish for in this past year. And most of all, to both of you, thanks for your unconditional love!

## Curriculum Vitae



Fatwa Firdaus Abdi was born on 15 October 1983 in Jakarta, Indonesia. In 2005, he graduated from Nanyang Technological University (NTU), Singapore, with a degree of Bachelor of Engineering, majoring in Materials Science and Engineering with a minor in Business. He then received a Singapore-MIT Alliance Fellowship for the completion of a dual master's program in 2006: Master of Engineering in Materials Science and Engineering from Massachusetts Institute of Technology and Master of Science in Advanced Materials for Micro- and Nano-Systems from National University of Singapore. Subsequently, he worked as a research officer in the materials technology division at NTU for a year, and another year as a dry etch process engineer at Intel Micron Flash Technology in Lehi, Utah. Since 2009, he has been a PhD student working in the group of Materials for Energy Conversion and Storage at TU Delft. During this period, he has been working on the development of metal oxide photoelectrodes for solar water splitting. Starting from September 2013, he will be working as a postdoctoral researcher at the Institute for Solar Fuels, Helmholtz-Zentrum Berlin für Materialien und Energie.